



HAL
open science

Development of the fictitious sources method for stratified media and design of resonant cavities antennas

Giacomo Benelli

► **To cite this version:**

Giacomo Benelli. Development of the fictitious sources method for stratified media and design of resonant cavities antennas. Physics [physics]. Université Paul Cézanne - Aix-Marseille III, 2007. English. NNT: . tel-00324206

HAL Id: tel-00324206

<https://theses.hal.science/tel-00324206>

Submitted on 24 Sep 2008

HAL is a multi-disciplinary open access archive for the deposit and dissemination of scientific research documents, whether they are published or not. The documents may come from teaching and research institutions in France or abroad, or from public or private research centers.

L'archive ouverte pluridisciplinaire **HAL**, est destinée au dépôt et à la diffusion de documents scientifiques de niveau recherche, publiés ou non, émanant des établissements d'enseignement et de recherche français ou étrangers, des laboratoires publics ou privés.

UNIVERSITÉ PAUL CÉZANNE AIX-MARSEILLE III
ÉCOLE DOCTORALE PHYSIQUE ET SCIENCES DE LA MATIÈRE

Année:

Thèse N°:

DEVELOPMENT OF THE FICTITIOUS SOURCES
METHOD FOR STRATIFIED MEDIA AND DESIGN OF
RESONANT CAVITIES ANTENNAS.

THÈSE

pour obtenir le grade de

DOCTEUR DE L'UNIVERSITÉ PAUL CÉZANNE
Faculté des Sciences et Techniques

Discipline : Optique, images et signales

présentée et soutenue publiquement par

Giacomo BENELLI

le 19 Janvier 2007

Les Directeurs de thèse Monsieur Gérard Tayeb et Monsieur Filippo
Capolino

JURY:

Monsieur Stefan ENOCH
Monsieur Gerard TAYEB
Monsieur Ronan SAULEAU
Monsieur Filippo CAPOLINO
Monsieur Vincenzo GALDI
Monsieur Vincenzo PIERRO

Contents

1	Introduction	1
2	The method of fictitious sources	3
2.1	Background and some history	3
2.1.1	Finite Element Methods	3
2.1.2	Moment Methods	4
2.1.3	Finite Difference Time Domain Method	4
2.1.4	Method of Fictitious Sources	5
2.2	The basis of the method	6
2.2.1	Perfectly conducting scatterer	10
2.2.2	Case of multiple scatterers	10
2.2.3	Case of excitation inside an object	10
2.3	Stratified medium problems	12
2.3.1	Green's function computation	13
2.4	Implementation	21
2.5	Results	24
2.5.1	Free-space problems	24
2.5.2	Stratified medium problems	39
3	A compact planar antenna	47
3.1	Introduction.	47
3.2	Fundamental antenna parameters	48
3.3	Initial configuration: Fabry-Perot antenna.	53
3.3.1	First conclusions	58
3.4	A 3D finite elements method	61
3.4.1	New kinds of grid	61
3.5	A method to dimension the cavity.	70
3.6	Grids for a better impedance matching	75
3.7	The introduction of perfectly magnetic walls.	80
3.7.1	Grid optimization with metallic walls	83
3.8	Conclusions	87

A	Green’s function magnetic field.	92
A.1	s- polarization	93
A.2	p- polarization	95
B	MFS and geometry representation	98
B.1	Geometry representation and the STL format	98
C	Waveguides and rectangular cavities	101
C.1	Rectangular waveguides	101
C.2	Perfectly metallic cavity	103
C.3	PEC/PMC waveguide and cavity	105

Chapter 1

Introduction

Today, the study of electromagnetic waves behavior in different environments is a topic of fundamental interest. In fact, it constitutes the hearth of modern technologies such as telecommunications, electronic, imaging, optical components, astronomy. In particular, the problem of electromagnetic scattering from a disordered or periodic set of objects, or from a set of defects on given surfaces, is the key to design devices that could improve the performance of processors, or increase the speed of networks.

Computer methods for analyzing problems in electromagnetics generally fall into one of three categories: analytical techniques, numerical techniques, and expert systems. Analytical techniques make simplifying assumptions about the geometry of a problem in order to apply a closed-form (or table look-up) solution. Numerical techniques attempt to solve fundamental field equations directly, subject to the boundary constraints posed by the geometry. Expert systems do not actually calculate the field directly, but instead estimate values for the parameters of interest based on a rules database.

A number of computer programs based on analytical techniques are available to the engineer. Analytical techniques can be a useful tool when the important EM interactions of the configuration can be anticipated. However, most EMC problems of interest are simply too unpredictable to be modeled using this approach.

Expert systems approach a problem in much the same way as a quick-thinking, experienced EM engineer with a calculator would approach it. As system design and board layout procedures become more automated, expert system EM software will certainly play an important role. Nevertheless, expert systems are no better than their rules database and it is unlikely that they will ever be used to model or understand phenomena driven by very complex EM interactions.

Numerical techniques generally require more computation than analytical

techniques or expert systems, but they are very powerful EM analysis tools. Without making a priori assumptions about which field interactions are most significant, numerical techniques analyze the entire geometry provided as input. They calculate the solution to a problem based on a full-wave analysis. A number of different numerical techniques for solving electromagnetic problems are available. Each numerical technique is well-suited for the analysis of a particular type of problem. The numerical technique used by a particular EM analysis program plays a significant role in determining what kinds of problems the program will be able to analyze.

The first part of this thesis illustrates the characteristics of a particular numerical technique called Method of Fictitious Sources (MFS) and how it has been implemented in a software that can solve a large class of three dimensional scattering problems. Pros and cons of MFS when compared with other methods will be illustrated. In the second part of this thesis, we will show how computer-aided design can help design innovative types of antennas.

Chapter 2 will illustrate in detail the basis of the Method of Fictitious Sources in comparison with other numerical methods. The method will be illustrated with examples involving homogeneous and stratified media.

Chapter 2.5 will propose the solution of some significant scattering problems obtained with our implementation of the MFS.

Chapter 2

The method of fictitious sources

2.1 Background and some history

In the past years, several numerical methods for electromagnetic computation have been developed. In fact, there is no such thing as "the universal method": on the opposite, by the need to solve different, very specific problems, several methods were born that slowly widened their field of applications, though each remaining more suited to a given class of problems. Without trying to be exhaustive, we would like to give a brief overview of the most known ones in comparison to the Method of Fictitious Sources.

2.1.1 Finite Element Methods

The first step in finite-element analysis is to divide the configuration into a number of small homogeneous pieces or elements. The elements can be small where geometric details exist and much larger elsewhere. In each finite element, a simple (often linear) variation of the field quantity is assumed.

Generally, finite-element analysis techniques solve for the unknown field quantities by minimizing an energy functional. The energy functional is an expression describing all the energy associated with the configuration being analyzed.

The major advantage that finite element methods have over other EM modeling techniques stems from the fact that the electrical and geometric properties of each element can be defined independently. This permits the problem to be set up with a large number of small elements in regions of complex geometry and fewer, larger elements in relatively open regions. Thus

it is possible to model configurations that have complicated geometries and many arbitrarily shaped dielectric regions in a relatively efficient manner. Commercial finite element codes are available that have graphical user interfaces and can determine the optimum placement of node points for a given geometry automatically.

2.1.2 Moment Methods

The method of moments (or moment method) is a technique for solving complex integral equations by reducing them to a system of simpler linear equations.

The equation solved by moment method techniques is generally a form of the electric field integral equation (EFIE) or the magnetic field integral equation (MFIE). Both of these equations can be derived from Maxwells equations by considering the problem of a field scattered by a perfect conductor (or a lossless dielectric). These are equations where the unknowns (that appear generally in a double integration expression) are the electric or magnetic surface current densities.

The first step in the moment-method solution process is to expand the unknown currents as a finite sum of given basis (or expansion) functions. Then the equations are enforced in discrete points on the surface directly or by the use of "weight" functions.

The unknowns of the problem are the coefficients of the surface current expansion and once found, can be used to calculate the scattered electric and magnetic fields directly from the induced currents.

2.1.3 Finite Difference Time Domain Method

The Finite Difference Time Domain (FDTD) method is a direct solution of Maxwells time dependent curl equations. In its simplest original formulation, it uses simple central-difference approximations to evaluate the space and time derivatives. It is a time stepping procedure where inputs are time-sampled analog signals. The region being modeled is represented by two interleaved grids of discrete points. One grid contains the points at which the magnetic field is evaluated, the second one contains the points at which the electric field is evaluated. By alternately calculating the electric and magnetic fields at each time step, fields are propagated throughout the grid. Time stepping is continued until a steady state solution or the desired response is obtained. At each time step, the equations used to update the field components are fully explicit. No system of linear equations must be solved.

Frequency domain results can be obtained by applying a discrete Fourier transform to the time domain results.

The required computer storage and running time is proportional to the electrical size of the volume being modeled and the grid resolution. Because the basic elements are cubes, curved surfaces on a scatterer must be staircased. For many configurations this does not present a problem, however for configurations with sharp, acute edges, an adequately staircased approximation may require a very small grid size. This can significantly increase the computational size of the problem. This requires additional computation, but a wide-band frequency-domain analysis can be obtained by transforming the systems impulse response. The first significant disadvantages of this technique is that the problem size can easily get out of hand for some configurations. The fineness of the grid is generally determined by the dimensions of the smallest features that need to be modeled. Another disadvantage is that the method introduces an artificial numerical dispersion due to the intrinsic nature of the method. Moreover, dispersive materials are more difficult to model with respect to other methods.

2.1.4 Method of Fictitious Sources

The Method of Fictitious Sources (MFS) is a relatively new method for analyzing EM problems. It is a frequency domain technique that (like the method of moments) is based on the method of weighted residuals. However, this method is unique in that the expansion functions are analytic solutions of the fields generated by sources located some distance away from the surface where the boundary condition is being enforced. Moment methods generally employ expansion functions representing quantities such as charge or current that exist on a boundary surface. The expansion functions of the MFS are wave field solutions corresponding to adequate sources. By locating these sources away from the boundary, the field solutions form a smooth set of expansion functions on the boundary and singularities on the boundary are avoided. Like the method of moments, a system of linear equations is developed and then solved to determine the coefficients of the expansion functions that yield the best solution. Since the expansion functions are already field solutions, it is not necessary to do any further computation to determine the fields. Conventional moment methods determine the currents and/or charges on the surface first and then must integrate these quantities over the entire surface to determine the fields. This integration is not necessary at any stage of the MFS solution. There is little difference in the way dielectric and conducting boundaries are treated by the MFS. The same expansion functions are used. For this reason, a general purpose implementation of the MFS can

model configurations with multiple dielectrics and conductors much more readily than a general purpose moment method technique. On the other hand, moment method techniques, which employ expansion functions that are optimized for a particular type of configuration (e.g. thin wires), are generally much more efficient at modeling that specific type of problem.

The MFS has been developed independently from different groups and in fact it is known with several names, as Generalized Multipole Technique (GMT), Method of Auxiliary Sources (MAS), Multiple Multipole Methods (MMP) and others. The first attempts to use this method were probably due to Kupradze [1]. During the eighties, the method has been discussed and applied, amongst the others, by Hafner, Leviatan and Boag, [2, 3]. In the past decade, fundamental advances on mathematical aspects of the problem has been made in Marseille's group by Tayeb, Cadilhac, Petit, leading to a different approach that produced many theoretical and numeric results [4, 5, 6, 7, 8].

2.2 The basis of the method

In the following chapters, time-harmonic fields are represented by complex vectors using a $e^{-j\omega t}$ dependence. We denote with ϵ_0 and μ_0 the permittivity and permeability of vacuum, by $k_0 = \omega\sqrt{\epsilon_0\mu_0}$ the wave number, and by $\eta_0 = \sqrt{\frac{\mu_0}{\epsilon_0}}$ the vacuum impedance. Where not differently specified, each medium is considered to be non-magnetic ($\mu = \mu_0$).

In order to give a framework to the method, we consider a 3D diffraction problem by a homogeneous, closed object, bounded by a surface \mathcal{S} (see figure 2.1). We call Ω_1 (resp. Ω_2) the exterior (resp. interior) of \mathcal{S} . The domain Ω_1 (resp. Ω_2) is supposed filled with a material of permittivity ϵ_1 (resp. ϵ_2). We assume that on the exterior of the surface we have a material ϵ_1 , while on the interior we have ϵ_2 , both generally complex and with positive imaginary part. The object is illuminated by a known incident field $F^{inc} = (\mathbf{E}^{inc}, \mathbf{H}^{inc})$ and we want to solve the total field $F = (\mathbf{E}, \mathbf{H})$.

It is known from the equivalence principle that the solution of the problem is completely represented by the tangential components of the total electromagnetic field, calculated on the surface \mathcal{S} . This is why it is convenient to represent the unknown total field by defining the couple Φ^1 of vector func-

¹We use $\eta_0\mathbf{H}$ instead of simply \mathbf{H} for numerical reasons. In fact, $|\eta_0\mathbf{H}|$ and $|\mathbf{E}|$ have comparable magnitudes and this may avoid possible numerical instabilities in the solution of the system, in some cases.

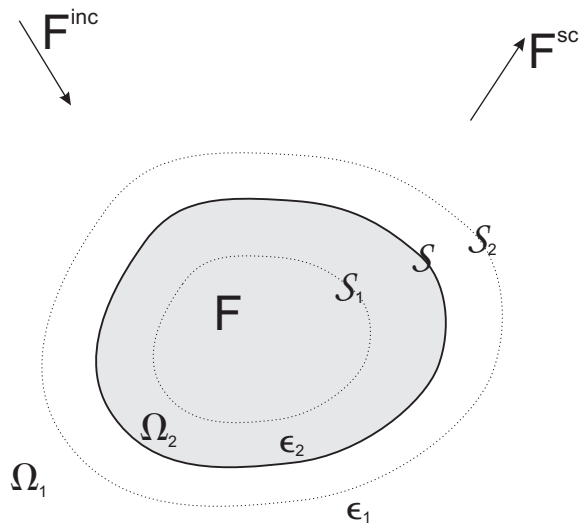


Figure 2.1: The scatterer is the greyed region. Its surface is \mathcal{S} , its interior is Ω_2 , its exterior is Ω_1 . The basic idea is to express the scattered field F^{sc} in Ω_1 as a combination of fields radiated from sources placed in Ω_2 . Viceversa, the field F in Ω_2 is expressed as a combination of fields radiated from sources placed in Ω_1 .

tions, defined on the surface \mathcal{S} :

$$\Phi = (\hat{\mathbf{n}} \times \mathbf{E}, \hat{\mathbf{n}} \times \eta_0 \mathbf{H})|_{\mathcal{S}} \quad (2.1)$$

and, in the same way, the same quantity referred to the incident field only

$$\Phi^{inc} = (\hat{\mathbf{n}} \times \mathbf{E}^{inc}, \hat{\mathbf{n}} \times \eta_0 \mathbf{H}^{inc})|_{\mathcal{S}}. \quad (2.2)$$

Let's eventually define also the scattered field F^{sc} as the difference between the total and the incident field

$$F^{sc} = F - F^{inc}. \quad (2.3)$$

We can now say that the solution of our problem is the total field F that satisfies the following conditions:

- (a) the scattered field F^{sc} satisfies Maxwell's equations in Ω_1 and a radiation condition at infinity,
- (b) the total field F satisfies Maxwell's equations in Ω_2 and
- (c) the boundary conditions on the surface \mathcal{S} of the scatterer are fulfilled.

Let's now consider N sources $S_{1,n}$ ($n = 1, 2, \dots, N$), placed on \mathcal{S}_1 inside Ω_2 and radiating fields $F_{1,n} = (\mathbf{E}_{1,n}, \mathbf{H}_{1,n})$ in the whole space supposed to be filled with a material with permittivity ϵ_1 . These sources, being placed in Ω_2 , generate a Maxwellian field $F_{1,n}$ with no singularities in Ω_1 : thus, $F_{1,n}$ fulfill the condition (a) mentioned above. Moreover, a linear combination $\sum_n c_{1,n} F_{1,n}$ (where $c_{1,n}$ are complex coefficients) still fulfill the same condition. If the coefficients $c_{1,n}$ are appropriately chosen, this linear combination can be regarded as an approximation of F^{sc} in Ω_1 .

In the same way, consider a set of fictitious sources $S_{2,n}$ ($n = 1, 2, \dots, N$) placed on \mathcal{S}_2 inside Ω_1 and radiating fields $F_{2,n} = (\mathbf{E}_{2,n}, \mathbf{H}_{2,n})$ in the whole space supposed to be filled with a material with permittivity ϵ_2 . A linear combination $\sum_n c_{2,n} F_{2,n}$ fulfill the condition (b) and, with the proper choice of $c_{2,n}$, can be regarded as an approximation of F in Ω_2 .

Now, denoting by $\Phi_{1,n}$ and $\Phi_{2,n}$ the boundary values of the fields $F_{1,n}$ and $F_{2,n}$ on \mathcal{S} , we can express the continuity of the total field's tangential component on \mathcal{S} , condition (c), as

$$\Phi^{inc} + \sum_n c_{1,n} \Phi_{1,n} - \sum_n c_{2,n} \Phi_{2,n} = 0. \quad (2.4)$$

From a mathematical point of view, equation 2.4 can be seen as the truncation of a decomposition of Φ on two different total basis $\Phi_{1,n}$ and $\Phi_{2,n}$, according to

$$\Phi^{inc} + \lim_{N \rightarrow \infty} \sum_{n=1}^N c_{1,n} \Phi_{1,n} = \lim_{N \rightarrow \infty} \sum_{n=1}^N c_{2,n} \Phi_{2,n}. \quad (2.5)$$

The truncation is necessary to implement the method, and this leads to an approximate result. From a mathematical point of view, this is an important aspect of the method: details on the effect of this truncation can be found in [9].

Now, equation 2.4 can be fulfilled on surface \mathcal{S} in several ways. The simpler one is the Point Matching method, and it has been applied by many authors to the MFS. It consists in enforcing the boundary condition over a set of sampling points (usually equally spaced) on surface \mathcal{S} . By appropriately choosing their number, one can get a square linear system with as many equations as unknowns, and can obtain a solution which fulfill exactly the boundary condition in this points. On the opposite though, between this points the solution may be badly verified and strong oscillations can be observed.

Our method is different and it is based on the least-square algorithm: the aim is to find, for a given N , a set of coefficients $c_{1,n}$, $c_{2,n}$ that minimize the norm

$$\Delta_N = \min \left\| \Phi^{inc} + \sum_{n=1}^N c_{1,n}(N) \Phi_{1,n} - \sum_{n=1}^N c_{2,n}(N) \Phi_{2,n} \right\|. \quad (2.6)$$

calculated on the surface of the scatterer.

In this way, the number of sampling points M used to enforce boundary condition (c) on \mathcal{S} can be chosen independently from the number of unknowns. We can thus increase the number of sampling points with respect to the point matching method, obtaining a better overall accuracy of the result for almost the same computational effort. Moreover, another important feature of this method is the fact that the normalized error

$$\tilde{\Delta}_N = \Delta_N / \|\Phi^{inc}\| \quad (2.7)$$

can be used to express the accuracy in the boundary condition (c) and so to provide a good index on the precision and convergence of the solution. It must be stressed that this is a precious tool that can avoid the usual procedure of running the same calculation with different number of unknowns and test points, just to check if convergence has been reached.

Once the unknowns $c_{1,n}$, $c_{2,n}$ have been found, it is possible to write the field in each region as

$$F^{sc} = \sum_{n=1}^N c_{1,n} F_{1,n} \text{ in } \Omega_1 \quad (2.8)$$

$$F = \sum_{n=1}^N c_{2,n} F_{2,n} \text{ in } \Omega_2. \quad (2.9)$$

2.2.1 Perfectly conducting scatterer

The case of a perfectly conducting scatterer can be treated in the same way, only keeping in mind that we only need one set of fictitious sources, placed inside the scatterer. In equation (2.5), the $c_{2,n}$ coefficients vanish. The boundary condition includes only the vanishing of the tangential components of \mathbf{E} .

So, the coefficients are obtained by minimizing the norm

$$\left\| \hat{\mathbf{n}} \times \mathbf{E}^{inc} + \sum_{n=1}^N c_{1,n} \hat{\mathbf{n}} \times \mathbf{E}_{1,n} \right\| \quad (2.10)$$

This is naturally due to the fact that the field inside a perfectly conductor scatterer is null.

2.2.2 Case of multiple scatterers

In case of multiple scatterers, a bit of care is needed to understand where a specific set of fictitious source will radiate. In general (see Fig. 2.2) for N scatterers, internal f.s. placed on $\mathcal{S}_{i,in}$ will radiate in $\Omega_1 = (\Omega_2 \cup \Omega_3 \cup \dots \cup \Omega_N)$ as if it was filled with an ϵ_1 material. On the opposite, external f.s. placed on $\mathcal{S}_{i,out}$ will radiate in Ω_i as in a whole space filled with ϵ_i material.

So, the total field in Ω_1 will be a superposition of fields radiated by every distribution of internal fictitious sources and the incident field. The field inside the n -th body instead, will be the result of the radiation of its own external fictitious sources distribution.

2.2.3 Case of excitation inside an object

Radiation problems are usually treated by placing an excitation inside the scatterer. Conceptually, no changes are necessary. The only difference is, keeping figure 2.1 as a reference, that the exciting field must be taken into

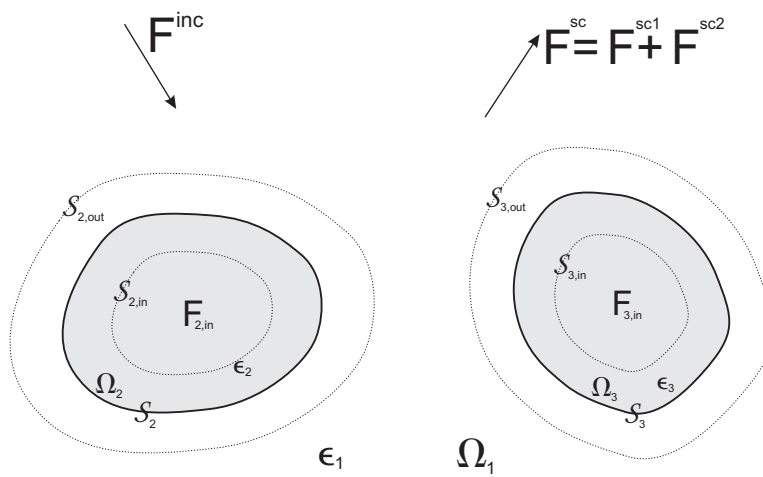


Figure 2.2: Case of multiple scatterers. Every internal f.s. distribution contributes to the field in Ω_1 . The field inside each scatterer is instead given only by its own external f.s. distribution.

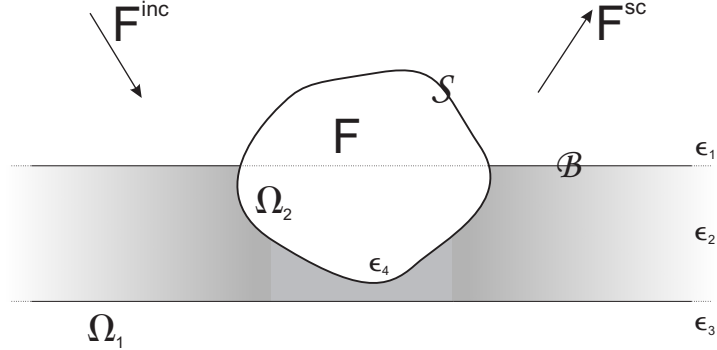


Figure 2.3: An object placed in a stratified medium formed by one layer only. The surface delimiting the object is denoted with \mathcal{S} , its interior is Ω_2 , its exterior is Ω_1 . We want to express the scattered field F^{sc} in Ω_1 as a combination of fields generated by sources placed inside Ω_2 , that radiate in the stratified medium. Viceversa, the field F in Ω_2 is expressed as a combination of fields generated by sources placed in Ω_1 that radiated in a uniform homogeneous space.

account in region Ω_2 only. Equation 2.4 changes accordingly, with Φ^{inc} having a negative sign:

$$-\Phi^{inc} + \sum_n c_{1,n} \Phi_{1,n} - \sum_n c_{2,n} \Phi_{2,n} = 0. \quad (2.11)$$

2.3 Stratified medium problems

With proper modifications, the MFS can be applied to problems involving the presence of a stratified medium.

The basic ideas of the method remains the same, that is, we want to express the fields in the different homogeneous regions of space as a combination of fields radiated by opportunely placed fictitious sources. What is different in this case is that the boundary conditions now must be fulfilled not only on the scatterer finite surface, but also on the interfaces between the layers of the stratified medium. These surfaces are infinite and so the boundary conditions on them cannot be enforced numerically in the usual way, but must be taken into consideration analytically.

We consider a 3D diffraction problem by a homogeneous, closed object, bounded by a surface \mathcal{S} (see fig. 2.3). We call Ω_1 (resp. Ω_2) the exterior

(resp. interior) of \mathcal{S} . The structure is illuminated by a known incident field $F^{inc} = (\mathbf{E}^{inc}, \mathbf{H}^{inc})$ and we want to solve the total field $F = (\mathbf{E}, \mathbf{H})$.

By using the same notation introduced in section 2.2, we can say that the solution of the problem is a field F that satisfies the following conditions:

- (a) the scattered field F^{sc} satisfies Maxwell's equations in Ω_1 , *boundary conditions on the interfaces \mathcal{B}* and a radiation condition at infinity,
- (b) the total field F satisfies Maxwell's equations in Ω_2 and
- (c) the boundary conditions on the surface \mathcal{S} of the scatterer are fulfilled.

The problem is conceptually identical to the one in the free space, with the exception of the boundary condition on \mathcal{B} that must be analytically taken into account into the appropriate fields that we will use. Condition (a) implies that F^{sc} will include these conditions. As F^{sc} will be expressed as a linear combination of sources placed in Ω_2 , these sources must be considered as if they were radiating in the unperturbed stratified medium, thus satisfying the boundary condition.

There is another aspect that must be considered. In fact, in the Ω_1 region the total field will be a superposition of F^{sc} and F^{inc} . Since condition (a) must eventually be satisfied by the total field, all the incident fields must include the boundary condition on \mathcal{B} too, and thus they must be computed as propagating in the unperturbed stratified medium.

In conclusion, a good way to think at the problem is that every field that will be used in the region Ω_1 must be considered as if it was propagating in the unperturbed stratified media. This applies both to incident fields and to the fields radiated by fictitious sources placed in Ω_2 .

This approach to stratified media problem is quite flexible, as it allows to model several kind of problems, like scatterers embedded in a substrate, interaction between scatterers in presence of a layered medium, defects and holes in metallic or dielectric films.

Unfortunately, a closed form, analytical solution for propagation in a stratified medium is known only for a small number of canonical cases, notably planewaves. For dipoles, the computation must be computed numerically and it requires some efforts to be accurate and fast enough to make the method practically usable.

2.3.1 Green's function computation

We used the method proposed by Martin et al. [10], with some modifications, and extended the computation to the magnetic field (as the tangential

components of the magnetic field on the inclusion are also required). The procedure is illustrated for the electric field only, please refer to Appendix A for the computation of the magnetic field.

The Green's function² plays a very important role in many numerical methods, so the problem of its computation has been addressed by many authors. Sommerfeld firstly treated the problem in single-interface stratified media, and other authors later studied it in connection with antennae radiation [11, 12, 13, 14, 15]. Lately, M.Paulus, P.Gay-Balmaz and O. J.F. Martin proposed a computation method, for the general case of multiple interfaces, that proved to be fast and accurate enough to be actually used in numerical methods [10]. In our work, we followed their footsteps and implemented this method, with some minor modifications, using it as the starting point to compute the magnetic field tensor too.

The Green's tensor $\mathbf{G}(\mathbf{r}, \mathbf{r}')$ for an arbitrary scattering system described by the dielectric permittivity $\epsilon(\mathbf{r})$ and the magnetic permeability $\mu(\mathbf{r})$ is the solution of the vector wave equation with a point source term [16]:

$$\nabla \times \mu^{-1}(\mathbf{r}) \nabla \times \mathbf{G}(\mathbf{r}, \mathbf{r}') - k_0^2 \epsilon(\mathbf{r}) \mathbf{G}(\mathbf{r}, \mathbf{r}') = \mu^{-1}(\mathbf{r}) \mathbf{1} \delta(\mathbf{r} - \mathbf{r}') \quad (2.12)$$

where $k_0^2 = \omega^2 \epsilon_0 \mu_0$ is the vacuum wave number. Notice that the time dependence is assumed to be $\exp(-j\omega t)$.

Without going too much into the details the homogeneous Green's function \mathbf{G}_H can be used as a starting point to compute the stratified medium Green's function \mathbf{G} . This can be done by using a Fourier representation of \mathbf{G}_H and performing the integration along z analytically, by using the calculus of residues, thus obtaining a plane-wave representation of \mathbf{G}_H .

Now, given $k_{Bz} = \sqrt{(k_B^2 - k_x^2 - k_y^2)}$, an appropriate orthonormal system can be introduced $\hat{\mathbf{k}}(k_{Bz}), \hat{\mathbf{l}}(k_{Bz}), \hat{\mathbf{m}}(k_{Bz})$ [17] where $\hat{\mathbf{k}}(k_{Bz})$ represents the propagation direction of a given (k_x, k_y) planewave, and $\hat{\mathbf{l}}(k_{Bz}), \hat{\mathbf{m}}(k_{Bz})$ represent respectively s and p polarization components.

By using this reference system, one can easily superpose to each Fourier component of \mathbf{G}_H the additional terms coming from the upgoing and downgoing plane waves that are present due to multiple reflection/transmission through the different interfaces, each one with the right amplitude depending on its polarization. This lead to eq.(9) on [10], which is the basic tensorial equation that express G . We report here the generalized expression for a given component of this equation

²Actually, what is computed is the Green's *tensor*, that is the electric vector field radiated in a given point by three orthogonal dipoles. Thus anytime we will mention the Green's function, we will mean the Green's *tensor* function.

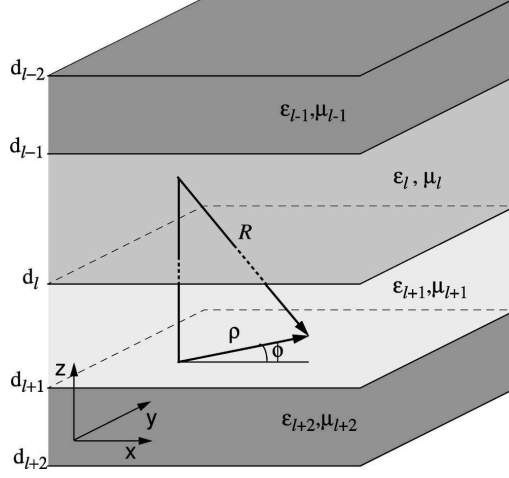


Figure 2.4: Stratified medium consisting of N layers with $(\epsilon_1, \mu_1, \dots, \epsilon_N, \mu_N)$ separated by interfaces at $z = d_1, \dots, d_{N-1}$. The vector $\mathbf{R} = \mathbf{r} - \mathbf{r}'$ defines the relative distance between \mathbf{r} and \mathbf{r}' and $\boldsymbol{\rho} = (x - x', y - y') = (\rho \cos \phi, \rho \sin \phi)$ is the projection of \mathbf{R} onto the xy plane.

$$\begin{aligned}
G_{\alpha\beta}(\mathbf{r}, \mathbf{r}') &= \frac{i}{8\pi^2} \int \int dk_x dk_y \exp\{i[k_x(x - x') \\
&\quad + k_y(y - y')]\} \frac{1}{k_{lz}} \{[\hat{l}_\alpha(\pm k_{lz}) A_{l,\alpha\beta}^s \exp(ik_{lz}z) \\
&\quad + \hat{l}_\alpha(\mp k_{lz}) B_{l,\alpha\beta}^s \exp(-ik_{lz}z)] \hat{l}_\beta(k_{lz}) \\
&\quad + [\hat{m}_\alpha(\pm k_{lz}) A_{l,\alpha\beta}^p \exp(ik_{lz}z) \\
&\quad + \hat{m}_\alpha(\mp k_{lz}) B_{l,\alpha\beta}^p \exp(-ik_{lz}z)] \hat{m}_\beta(k_{lz})\}.
\end{aligned} \tag{2.13}$$

Here, the coefficients $A_{l,\alpha\beta}^s, B_{l,\alpha\beta}^s, A_{l,\alpha\beta}^p, B_{l,\alpha\beta}^p$ are the amplitude coefficients of the upgoing and downgoing waves in the l -th layer, for s - and p -polarizations. The upper sign refers to the case $z > z'$ and the lower sign to the case $z < z'$. It must be noticed that $k_{lz}, \hat{l}, \hat{m}, A^s, B^s, A^p, B^p$ are all function of k_x, k_y .

Equation (2.13) can be simplified by introducing a cylindrical coordinate

system in the xy and $k_x k_y$ planes, via the substitutions

$$\begin{aligned}\mathbf{R} &= (x - x', y - y', z - z') = (\boldsymbol{\rho}, z - z'), \\ \boldsymbol{\rho} &= (\rho \cos \phi, \rho \sin \phi)\end{aligned}$$

$$\begin{aligned}\mathbf{k} &= (k_x, k_y, k_z) = (\mathbf{k}_\rho, k_z), \\ \mathbf{k}_\rho &= (k_\rho \cos k_\phi, k_\rho \sin k_\phi).\end{aligned}$$

The integration over k_ϕ can now be performed analytically by using Bessel functions [18]:

$$J_n(k_\rho \rho) = \frac{i^{-n}}{2\pi} \int_0^{2\pi} dk_\phi \exp(ik_\rho \rho \cos k_\phi) \cos(nk_\phi) \quad (2.14)$$

and this leaves us with only a monodimensional integration to perform, over k_ρ , in the form

$$\mathbf{G}(\mathbf{r}, \mathbf{r}') = -\frac{\hat{z}\hat{z}}{k_l^2} \delta(\mathbf{R}) + \frac{i}{4\pi} \int_0^\infty dk_\rho [\mathbf{f}^s(k_\rho; \mathbf{r}, \mathbf{r}') + \mathbf{f}^p(k_\rho; \mathbf{r}, \mathbf{r}')]. \quad (2.15)$$

The components \mathbf{f}^s and \mathbf{f}^p are given in Appendix B of [10].

Equation (2.15) is a typical Sommerfeld integral in the form

$$\begin{aligned}G(k_\rho; \mathbf{r}, \mathbf{r}') &= g(k_\rho; \mathbf{r}, \mathbf{r}') J_n(k_\rho \rho) [\mathcal{A}(k_\rho, z') \exp(ik_{lz} z) \\ &\quad + \mathcal{B}(k_\rho, z') \exp(-ik_{lz} z)].\end{aligned} \quad (2.16)$$

The numerical computation of this function is not straightforward due to the very awkward behavior of the integrand. The integrand, in fact, has two class of singularities: poles and branch points.

Regarding branch points, they are related to $k_{lz} = \sqrt{(k_l^2 - k_\rho^2)}$ which, being the square root of a complex number, is double valued and branch cuts given by $\text{Im}(k_{lz} = 0)$ intersect the plane of integration. Each branch cut ends in a branch point located in $k_\rho = \pm k_{lz}$. It is possible to demonstrate [19, 20] that those branch cuts and branch points exists only for the two outermost layers, so only for $k_\rho = \pm k_1, \pm k_N$.

We can choose the right sign for the calculation of k_{lz} by physical considerations. In particular, the radiation condition imposes that the integrand must vanish for $z = \pm\infty$, so we must use the value with $\text{Im}(k_{lz}) = 0$.

The second class of singularities are poles, coming from the vanishing denominators in eq.(2.16). For dielectric media (without losses), such poles are in the region $k_\rho < k_{lmax} = \max_l \text{Re}(k_l)$. If there are losses, the singularities

shift in the first quadrant of the plane of integration, but still can cause a problem if they are close enough to the $Re(k_\rho)$ axis (that is, for small losses).

Once the singularities of the integrands have been located, we must chose an appropriate integration path that accurately avoids them and suitable numerical quadrature algorithms. The basic idea is to pass in the fourth quadrant of the complex plane, in such a way to surround the singularities. This can be done along an ellipse starting in $k_\rho = 0$, with a major axis equal to at least k_{lmax} . The minor axis instead is a balance between the need to be far from the singularities but without extending too much into the negative imaginary direction, where the integrand increases rapidly.

For the rest of the integration, it is not possible to find a path which is always valid, like in the case of the ellipse. In fact, the behavior of the integrands along the real k_ρ axis is quite variable depending on the value of $k_\rho\rho$ and $|z - z'|$. In particular, in the case where $|z - z'|$ is small enough, the exponential damping of equation(2.16) that normally makes the integrand vanish for $k_\rho \rightarrow \infty$ are quite weak and reveals the oscillatory nature of the integrands, thus making the quadrature more difficult. In that case, it is more convenient to use an integration path which is parallel to the imaginary axis, by transforming the integrands making use of the Hankel functions:

$$\begin{aligned} J_n(k_\rho\rho) &= \frac{1}{2}[H_n^{(1)}(k_\rho\rho) + H_n^{(2)}(k_\rho\rho)] \\ &= \frac{1}{2}[H_n^{(1)}(k_\rho\rho) + [H_n^{(1)}((k_\rho\rho)^*)]^*]. \end{aligned} \quad (2.17)$$

For large values of $k_\rho\rho$ in fact, the Hankel function has the following asymptotic behavior

$$\lim_{|k_\rho\rho| \rightarrow \infty} = \sqrt{\frac{2}{\pi k_\rho\rho}} e^{[ik_\rho\rho - \frac{1}{2}i\pi(n + \frac{1}{2})]} \quad (2.18)$$

that ensures, with its exponential term, a fast convergence when $Im(k_\rho\rho) \rightarrow \infty$.

When trying to implement this strategy, we found that it is quite hard to find a given value $|z - z'|$ that can be used to decide between the real or the imaginary axis integration path. In fact, while it is surely true that the integrands becomes oscillatory under a given value, it is also true that the asymptotic behavior 2.18 is both dependent on ρ and k_ρ . This means that in case of very small values of ρ , the integrands vanishes so slowly along the imaginary axis that it can actually be more convenient to keep integrating on the real axis.

So, instead of using a given value of $|z - z'|$ to switch between integration paths, we have identified a relation $\rho = f(|z - z'|)$ who defines a given

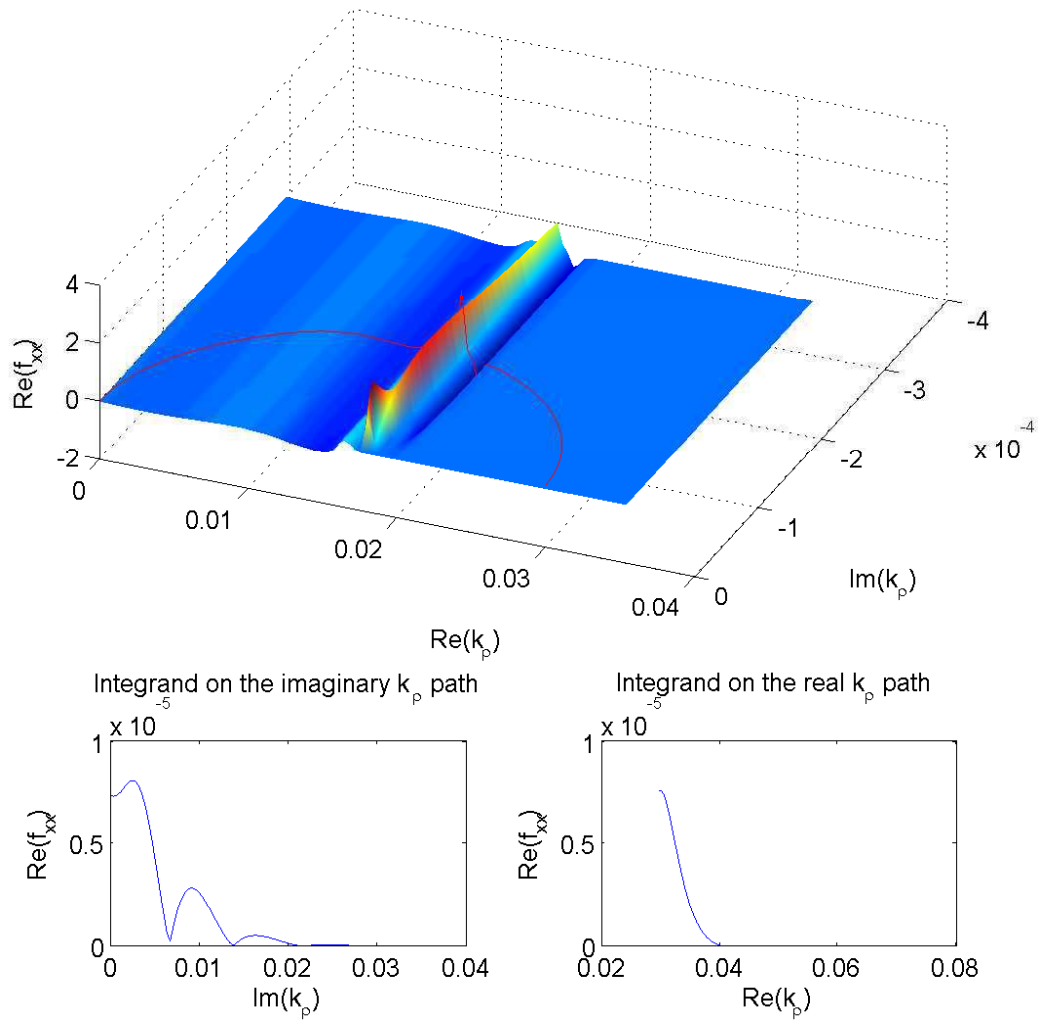


Figure 2.5: Real part of the integrand(xx component), taken for a three layers media, with $\epsilon_1 = 1$, $\epsilon_2 = 4$, $\epsilon_3 = 3$. The wavelength is 633 and the central layer extends from -300 to 300 . The source is placed in $(x', y', z') = (0, 0, -150)$ while the observation point is in $(x, y, z) = (150, 150, -100)$.

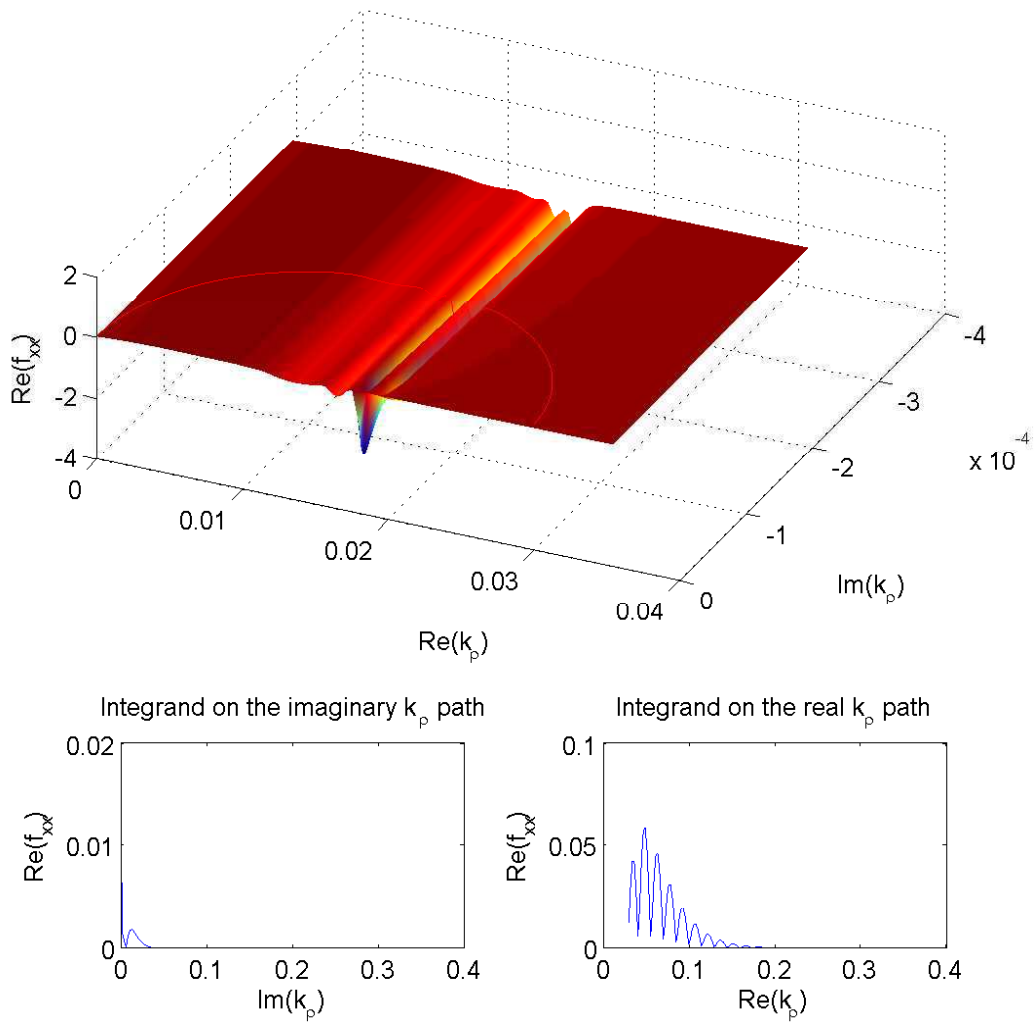


Figure 2.6: Same as in figure2.6 but here $z = 250$. It can be observed how the integrand's behavior on the real k_p is much more oscillatory.

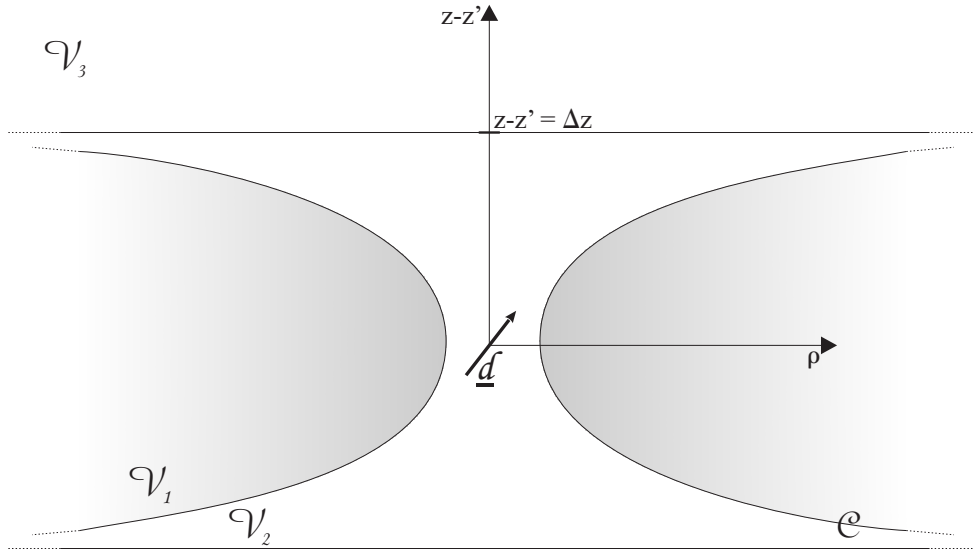


Figure 2.7: Integration strategy. Imaginary-axis integration is used in volume \mathcal{V}_1 only, while in \mathcal{V}_2 and \mathcal{V}_3 , a real-axis path is used.

surface \mathcal{C} . Every observation point falling in the region $\rho \leq f(|z - z'|)$ will be solved with the real-axis integration path, other points will be solved with the imaginary-axis integration path.

After running several examples, we empirically identified a suitable surface \mathcal{C} , and expressed it through polynomial interpolation. Such relation is illustrated in figure 2.7.

2.4 Implementation

There are some aspects of the method, which have not been put in evidence so far, that must be taken into consideration in order to implement it. In particular, it must be noticed how there are several degrees of freedom in the choice of:

- Type of sources (dipoles, multipoles, others...)
- Position of the sources (distance between sources and surface of the scatterer)
- Number of sources (truncation of the series in eq.2.5)
- Number of surface points (number of points where boundary conditions will be enforced)

Every choice regarding these aspects has an impact on the accuracy of the method. Moreover, solutions that are well adapted to a given class of problems, can be completely unappropriate for others. Thus, it is very important to produce a code which is as flexible as possible with regards to these choices.

All the results produced in this report are obtained by using dipoles as fictitious sources. They are ranged in such a way to form couples of crossed dipoles, oriented tangentially with respect to the scatterer's surface. See Figure 2.8 for an example in the case of a sphere. The choice of dipoles is deliberate: in fact, while some authors [2] suggest to mix dipoles with special sources (multipoles or line sources) at given positions in order to minimize the number of unknowns, we prefer to have more unknowns, but that do not need special care in their placement (apart from the distance from the surface of the scatterer). This produces a more generic approach which is in general able to solve any kind of objects without necessarily knowing much about the properties of the solution.

In addition, in order to solve problems in stratified media, we must be able to calculate the field radiated by fictitious sources in such a medium (see Appendix A). This is a quite demanding task and dipoles, in this sense, are the best compromise between accuracy and difficulty of calculation and eventually could be used as a base for more complicated source types. On the other hand, some other sources could be easier to calculate.

Regarding the fictitious surfaces used to place f.s., our experience, and that of other authors, show that in the majority of the cases the best results are obtained using a surface perfectly conformal to the shape of the scatterer.

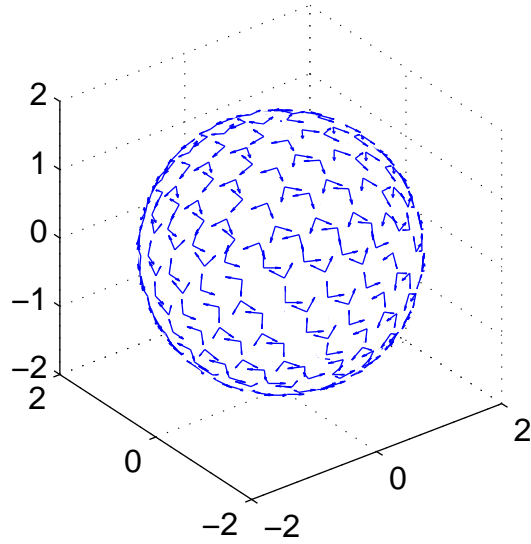
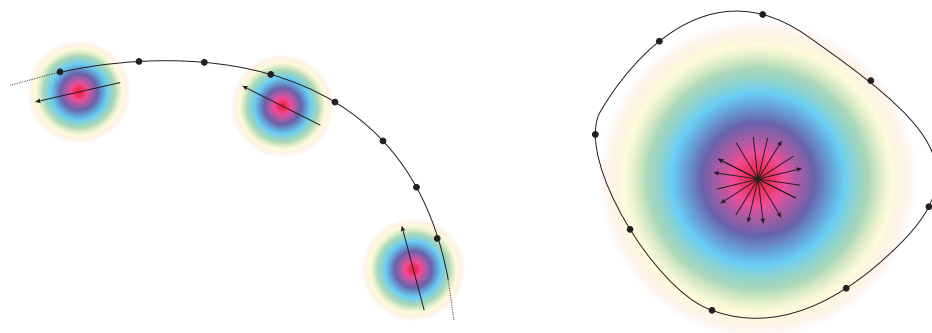


Figure 2.8: Crossed dipoles distributed tangentially on the surface of a sphere.



(a) Too small distance between source and surface. The matrix produced is singular. (b) Too high distance between source and surface. The matrix produced is degenerate.

Figure 2.9: Extreme choices of d_{os}

Other aspects that must be taken into consideration are the total number of fictitious sources N_s , their reciprocal distance d_{ss} and their distance from the scatterer surface d_{os} . The distance d_{os} has an influence on the accuracy of the solution in the sense that a small d_{os} can degrade the accuracy of the numerical solution, while a large d_{os} can make the matrix unsuitable for numerical computation [21, 22].

An empirical explanation of this phenomenon is given by figure 2.9 where the two extremes are illustrated. For a too small d_{os} , each source radiates a very high field in the few points in its proximity and a quasi-null field elsewhere. This produces a very ill-conditioned matrix, where the diagonal contains values several order of magnitude higher than the rest of it. For a too high d_{os} , one source is almost indistinguishable from the others, thus giving a degenerate matrix, that contains almost the same values on each column of the same row.

The problem is a little bit more complicated from the fact that the range of acceptable values for d_{os} depends also on the choice of N_s or d_{ss} . Nevertheless, we found that this range is large enough to allow some degrees of freedom in the f.s. placement. For objects that are not too small with respect to the wavelength, we use a starting distance equal to approximately one half of the scatterer dimension, using the normalized error 2.7 as a reference to fine-tune.

Once the d_{os} and N_s parameters are chosen for inner fictitious sources, the same values are usually used for external ones. We have observed though that the quality of the solution is much less sensitive to external sources than to internal ones.

2.5 Results

2.5.1 Free-space problems

We present here the results of some typical scattering problems solved with the fictitious sources method. All the problems are completely frequency-scalable, so some dimensions are presented in arbitrary units.

Sphere

This problem involves a dielectric ($\epsilon_r = 3$) sphere of radius $R = 2.3$. Taking figure 2.10 as a reference, the incident field is a plane wave with propagation vector $\hat{k} = (\hat{x}, \hat{y}, \hat{z}) = (0, 0, -1)$, and x -polarized electric field, with wavelength 2π .

The surface of the scatterer is meshed with 500 points, while two spheres with 320 points are used for fictitious sources placement, placed at a distance $d = 0.7R$ from the scatterer's surface. On each point of the surface, four scalar equations are enforced, imposing the continuity of the tangential components of the electric and magnetic fields. The fictitious sources are ranged in such a way to have two crossed dipoles on each of the 320 points (see Figure 2.11).

This leads to a linear system with 2000 equations and 1280 unknowns. On a standard laptop PC, around 80 seconds are needed to solve the system and trace a 100x100 points field map.

Figure 2.12 shows the far scattered field. The bistatic cross section is shown, as defined in [23], pag. 401.

Figure 2.13 shows the normalized error on the surface of the scatterer: it is computed as

$$\frac{1}{\|\Phi^{inc}\|} \left| \Phi^{inc} + \sum_{n=1}^N c_{1,n}(N)\Phi_{1,n} - \sum_{n=1}^N c_{2,n}(N)\Phi_{2,n} \right|. \quad (2.19)$$

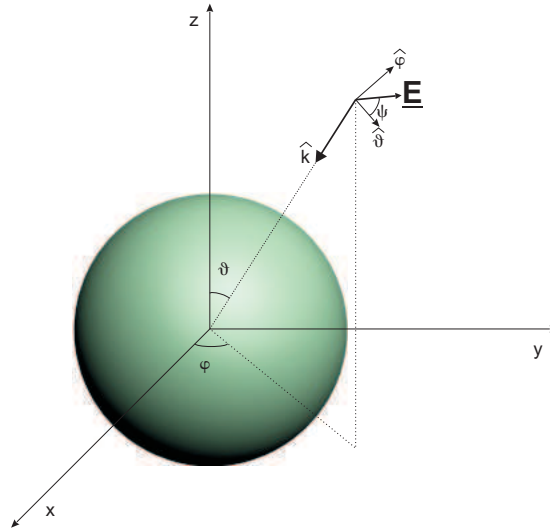


Figure 2.10: A typical scattering problem with an incident plane wave. The polarization is described in terms of the angle that the electric field forms with the $\hat{\theta}$ unitary vector.

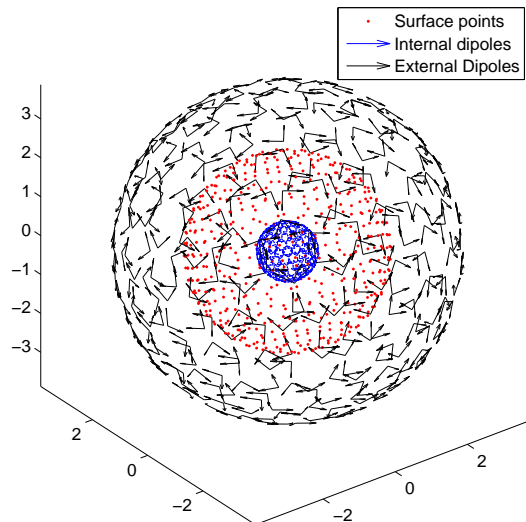


Figure 2.11: Surface mesh and crossed dipoles used as fictitious sources.

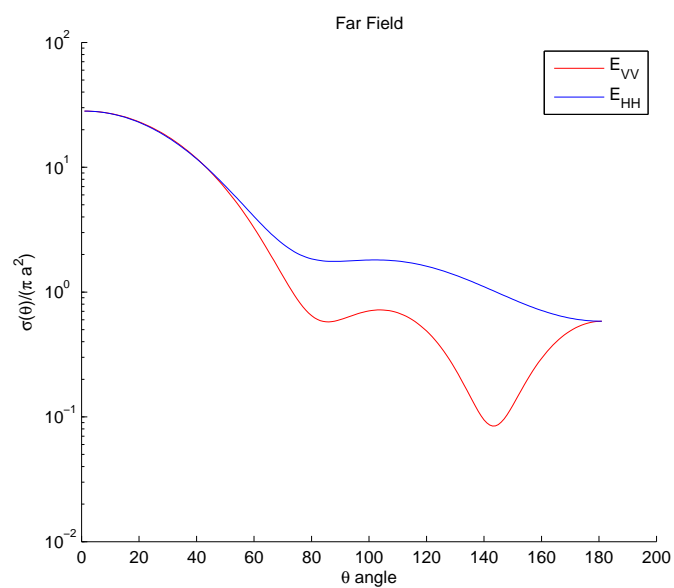


Figure 2.12: Bistatic Scattering Cross Section of the dielectric sphere. E_{VV} is the θ -component of the electric field, computed in the $\phi = 0$ plane. E_{HH} is the ϕ -component of the electric field, computed in the $\phi = \pi/2$ plane.

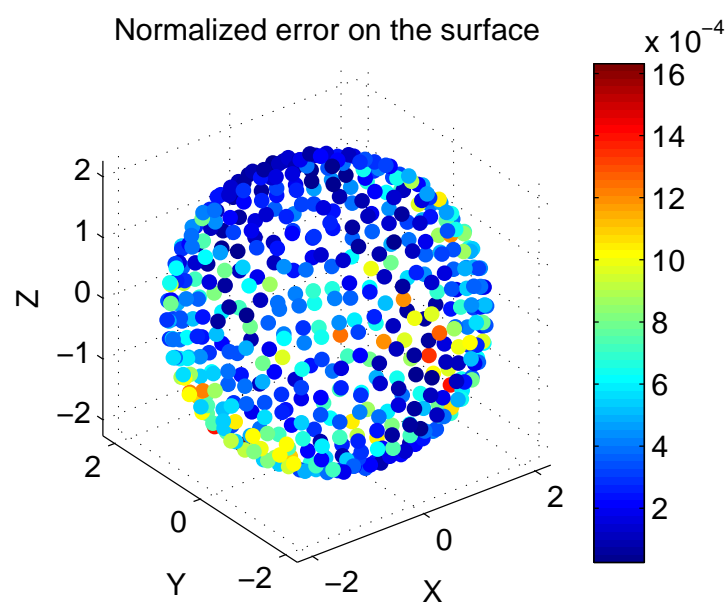


Figure 2.13: The maximum error in the boundary conditions is in the magnitude of 10^{-3} .

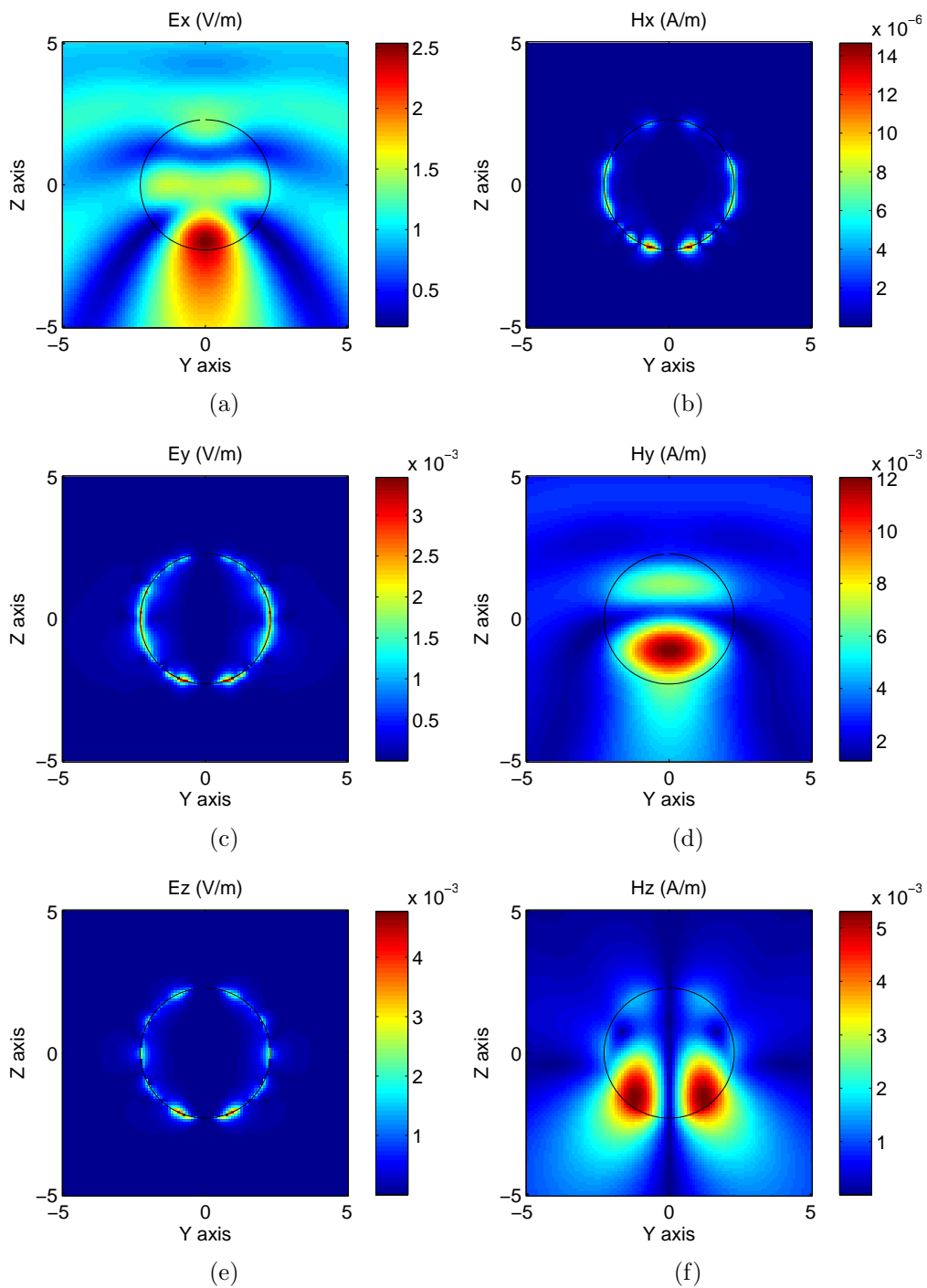


Figure 2.14: Electric and Magnetic field components on the YZ axis. It should be recalled that the incident planewave is X-polarized. In particular from 2.14(a) it can be verified that, in this plane, the X component of the total electric field (incident+scattered) is continue everywhere on the surface of the sphere, as it is expected. 28

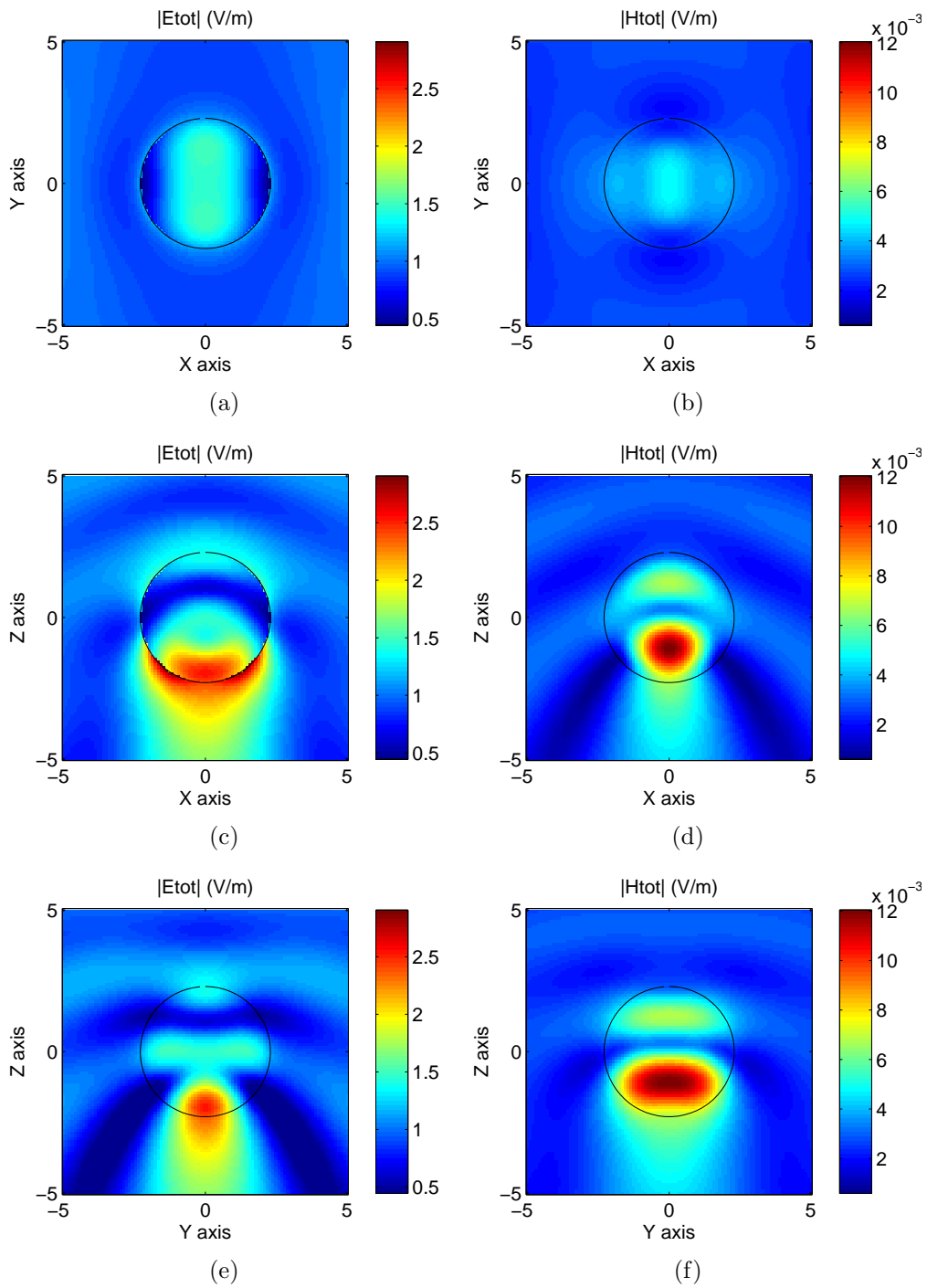


Figure 2.15: Absolute value of the total Electric and Magnetic field, on the three main planes XY, XZ and YZ cutting through the sphere.

Cube

Objects with edges are known to give accuracy problems, especially to represent fields around the edges [24]. In our implementation though, we found that it is always possible to improve the precision by increasing the number of fictitious sources without the need to approach them to the edge. It must be noticed, however, that due to the particular surface mesh we use (see Appendix B), no points are ever placed exactly on corners or vertexes. In our vision, this doesn't represent a limitation, because for real-world problems, objects are always smoothed at a certain scale.

Figure (2.16) shows that the corners are indeed the regions where the error is higher, but still very acceptable (around 10^{-2} at least).

The scatterer is a dielectric cube ($\epsilon_r = 2.2$) with side equal to $L = 11.9 \cdot 10^{-2}$. Taking figure 2.10 as a reference, the incident field is a plane wave with propagation vector $\hat{k} = (\hat{x}, \hat{y}, \hat{z}) = (0, 0, -1)$, and polarized as $\psi = 45^\circ$, with wavelength $7.5 \cdot 10^{-2}$.

The surface of the scatterer is meshed with 972 points, while two cubes with 588 points are used for fictitious sources placement, placed at a distance $d = 0.7L$ from the scatterer's surface. This leads to a linear system with 3888 equations and 2352 unknowns. On a standard laptop PC, around 110 seconds are needed to solve the system and trace a 100x100 points field map.

Figure 2.17 show the far scattered field.

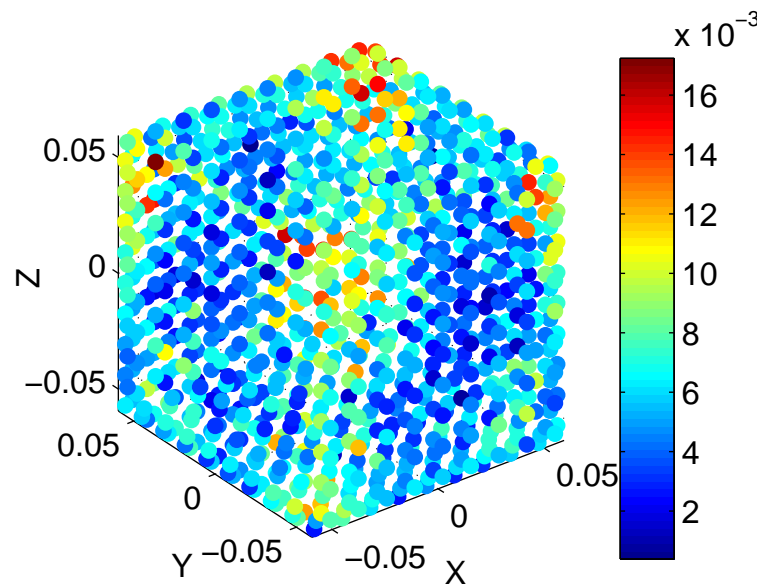


Figure 2.16: The maximum error in the boundary conditions is in the magnitude of 10^{-2} .

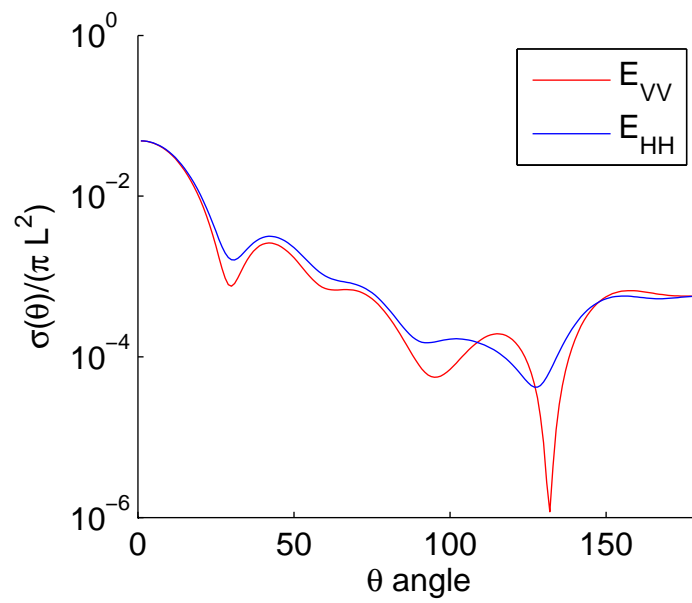


Figure 2.17: Bistatic Scattering Cross Section of the dielectric cube. E_{VV} is the θ -component of the electric field, computed in the $\phi = 0$ plane. E_{HH} is the ϕ -component of the electric field, computed in the $\phi = \pi/2$ plane.

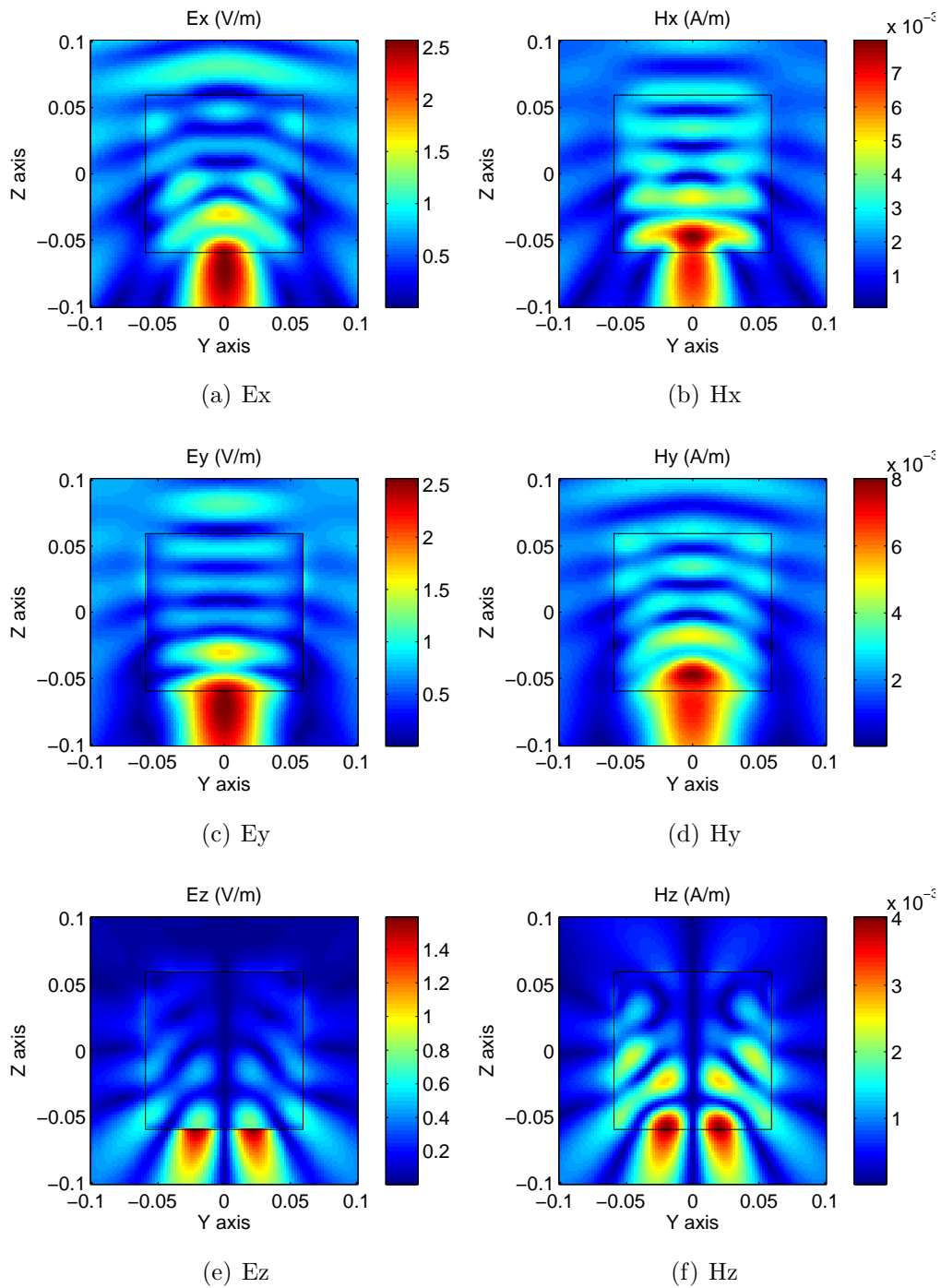


Figure 2.18: Electric and Magnetic field components on the YZ plane. It should be recalled that the incident planewave has both a X- and a Y- polarized component.

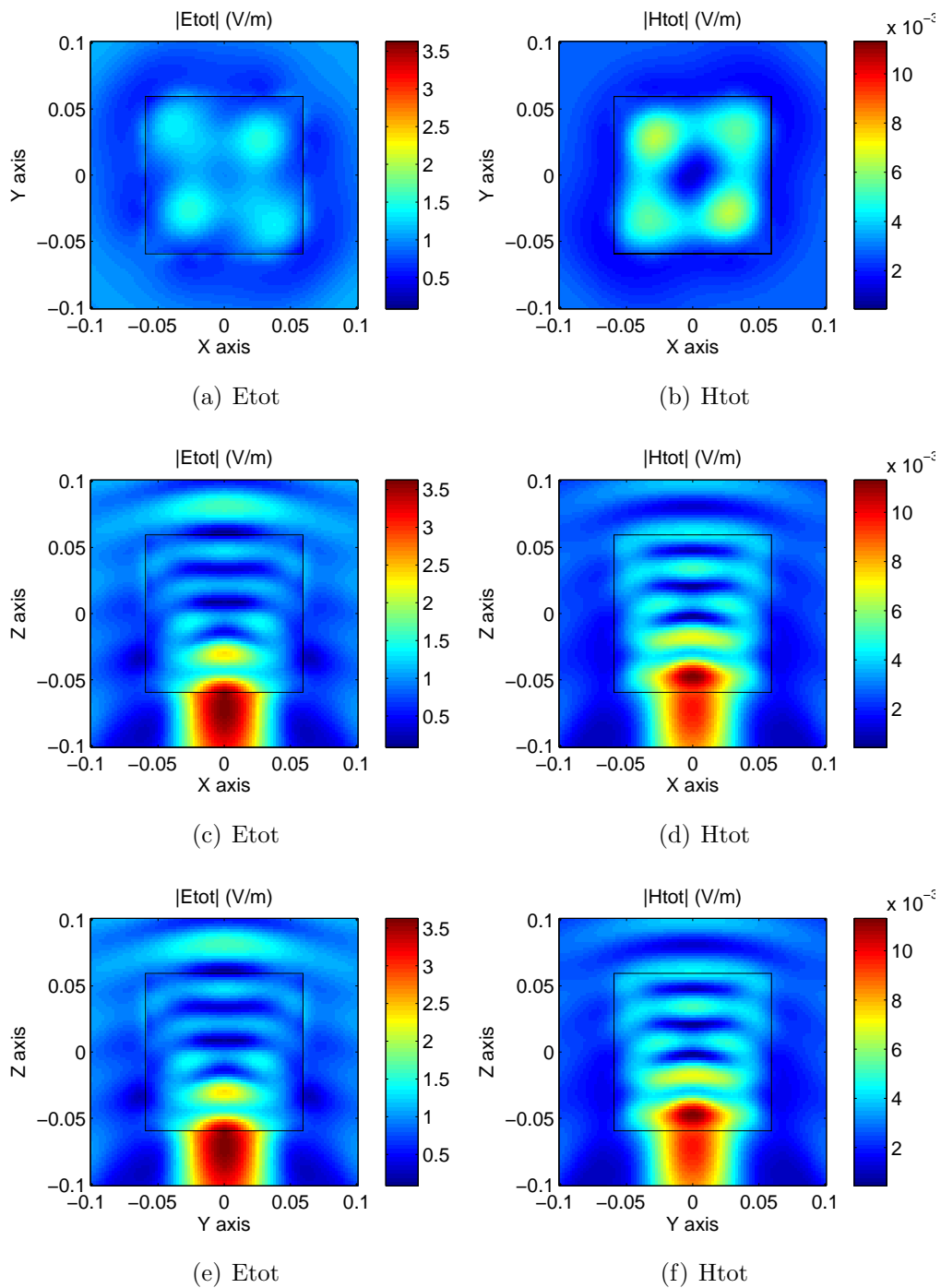


Figure 2.19: Absolute value of the total Electric and Magnetic field, on the three main planes XY, XZ and YZ cutting through the cube.

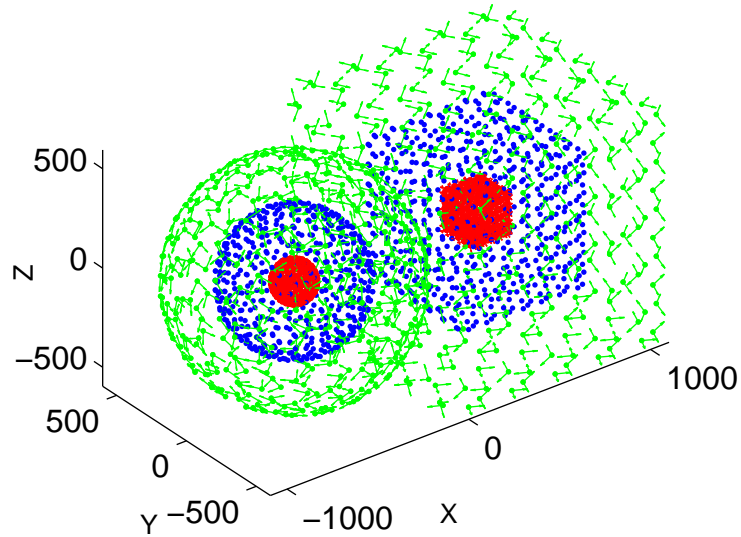


Figure 2.20: A spherical and a cubic scatterer (in blue), with inner (red) and outer (green) f.s. distributions.

Multiple scatterers

An example of multiple-scatterer problems is given here, showing the case of two dielectric objects: a sphere and a cube. The sphere has radius $R = 350$, center $C_s = (-500, 0, 0)$ and relative permittivity $\epsilon_r = 3$. The cube has side $D = 700$, it is centered in $C_c = (500, 0, 0)$ and it has relative permittivity $\epsilon_r = 2.2$. The problem is solved for a wavelength equal to 800, under the excitation of an incident planewave with propagation vector defined by the angles $\theta = 45^\circ$, $\phi = 45^\circ$, $\psi = 0^\circ$.

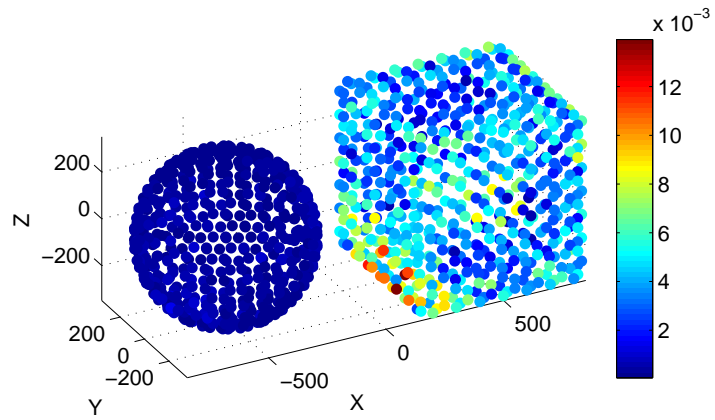


Figure 2.21: The maximum error in the boundary conditions is in the magnitude of 10^{-2} .

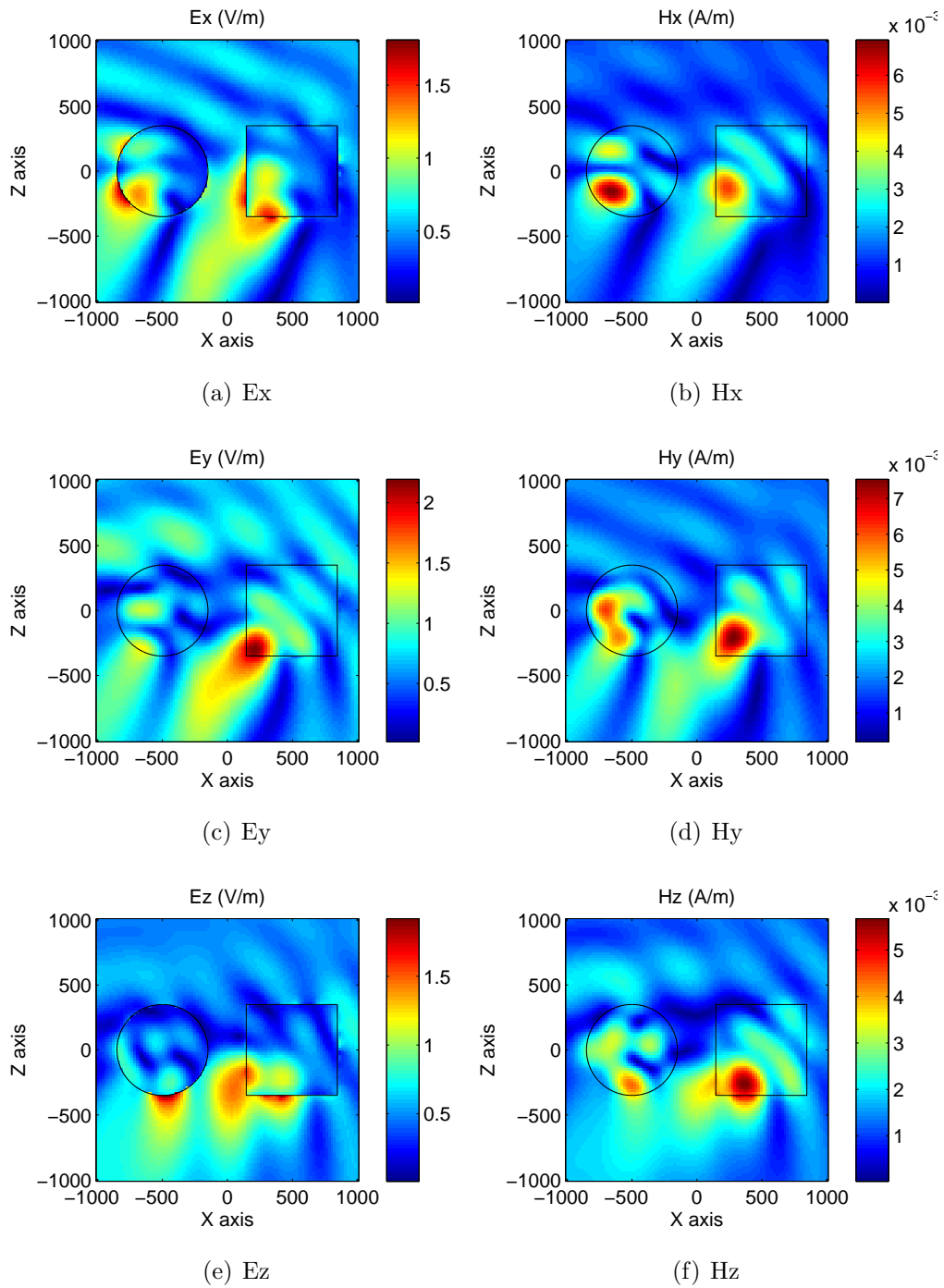


Figure 2.22: Electric and Magnetic field components on the XZ plane.

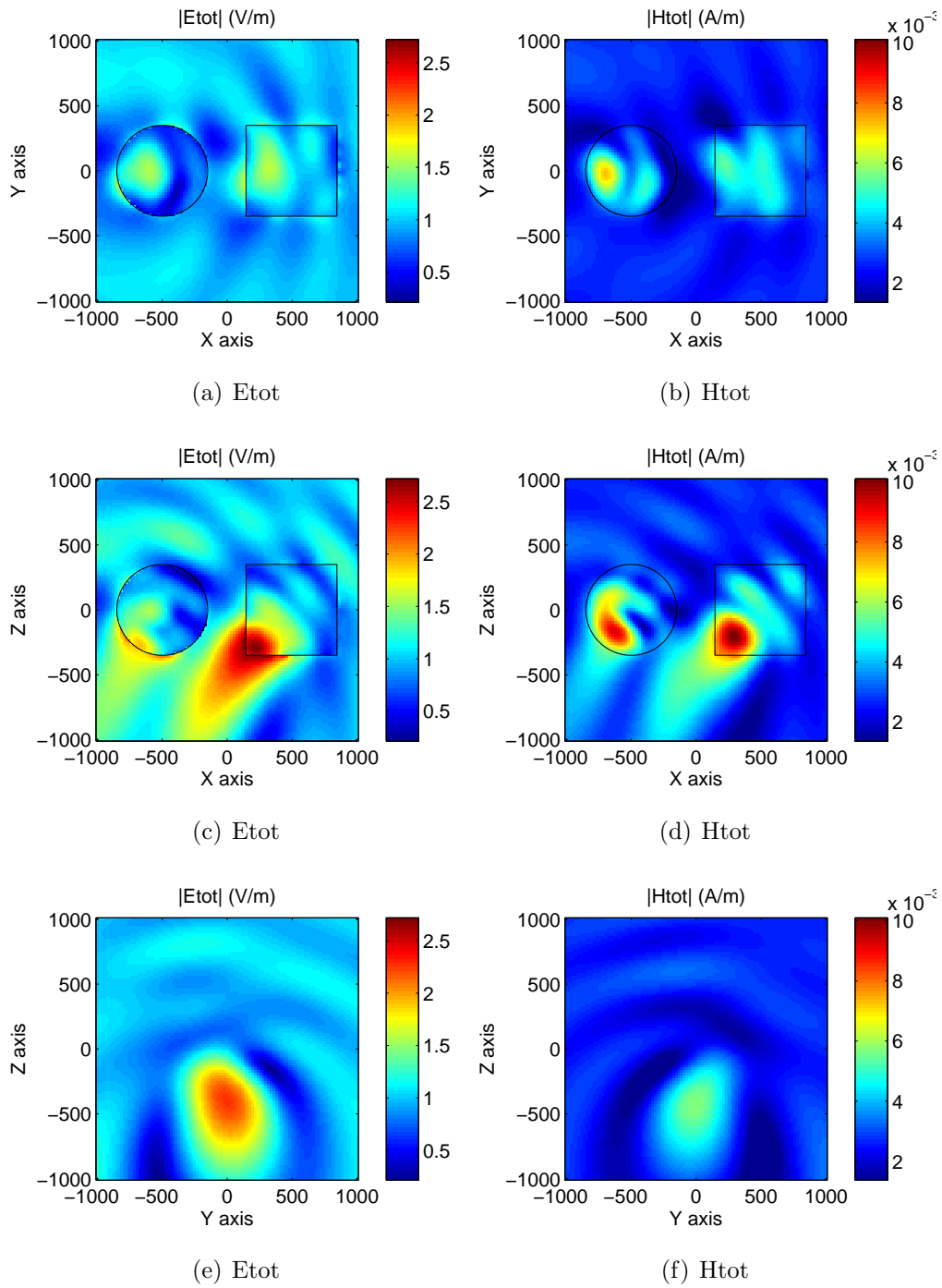


Figure 2.23: Absolute value of the total Electric and Magnetic field, on the three main planes XY, XZ and YZ cutting through the scatterers.

2.5.2 Stratified medium problems

Our aim when dealing with stratified media, is to be able to model plasmonic devices. Such devices include, amongst the others, sub-wavelength holes in metallic layers, metal-dielectric interfaces, metallic nanocavities or defects on metallic surfaces.

We present here some results we have obtained for some of these configurations.

Spherical cavity in a metallic layer

An example of a defect on a metallic surface has been modeled by partially superimposing a spherical scatterer filled with air to a metallic layer. The metallic layer has an air superstrate and substrate. It has a complex relative permittivity equal to $\epsilon_r = (-9.89 + i1.05)$ and extends from $z = -400\text{nm}$ to $z = 200\text{nm}$. The sphere has a radius equal to $R = 350\text{nm}$ and it is centered in the origin of the coordinate system.

A repartition of sources on spheres of radius 245 nm and 455 nm (resp. for the internal and external sources) has been found to give accurate results for reasonable computational burden (see Fig. 2.24). We used 640 fictitious sources on each spheres (two crossed dipoles on each of the 320 points on the spheres) and the boundary conditions are computed on 500 points on the spherical inclusion. With this configuration we have about one point for each $(\lambda/15)^2$ area on the spherical inclusion. Thus, the least square problem consist in minimizing the error on the continuity of the two tangential components of the electric and magnetic fields on 500 points (i.e. 2000 equations) by choosing the 1280 amplitudes of the fictitious sources.

Fig. 2.26 shows a map of the modulus of the electric field when the structure is enlightened by a plane wave coming from the top of the figure, with a normal incidence (with respect to the stratified media), linearly polarized along x-axis and a wavelength equal to 800 nm. The enhancement of field inside the cavity shows that a resonance of the cavity has been excited, but note that the parameters have not been optimized with this aim. In order to illustrate that point we have plotted on Fig. 2.25 the residual error on each point of the embedded object. Note that the error is always less than 9.10^{-3} .

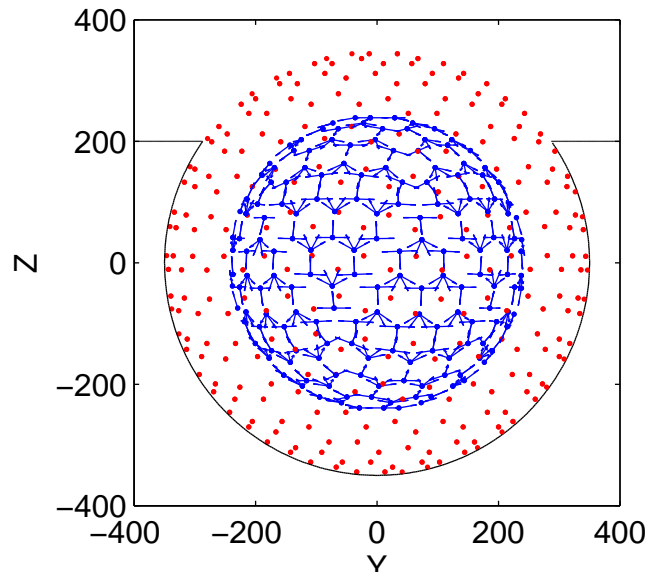


Figure 2.24: A sketch of the sphere mesh (in red) and of interior fictitious sources placement (in blue). The illustrated fictitious sources radiate in the unperturbed stratified medium.

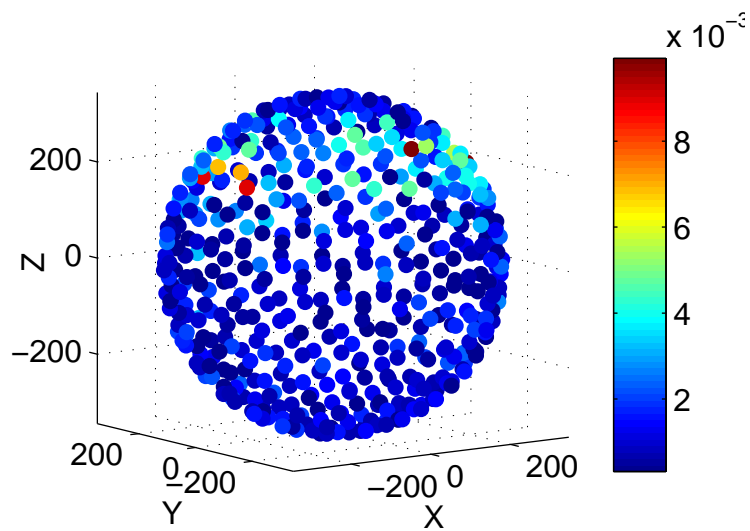


Figure 2.25: The maximum error in the boundary conditions is in the magnitude of 10^{-2} and it is concentrated in the upper part of the sphere, and on the sphere-layer interface in particular.

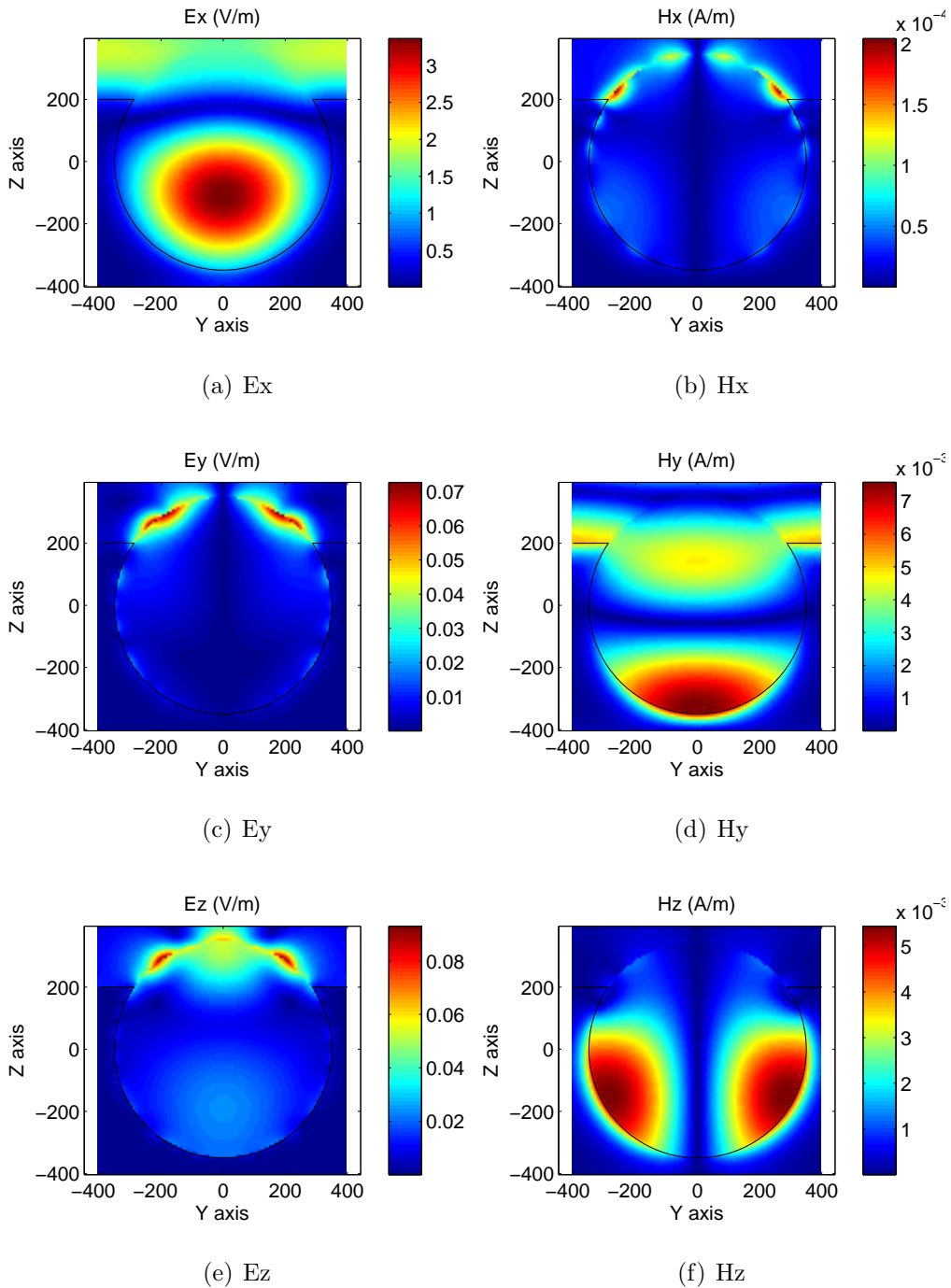


Figure 2.26: Electric and Magnetic field components on the YZ plane. It should be recalled that the incident planewave is X polarized.

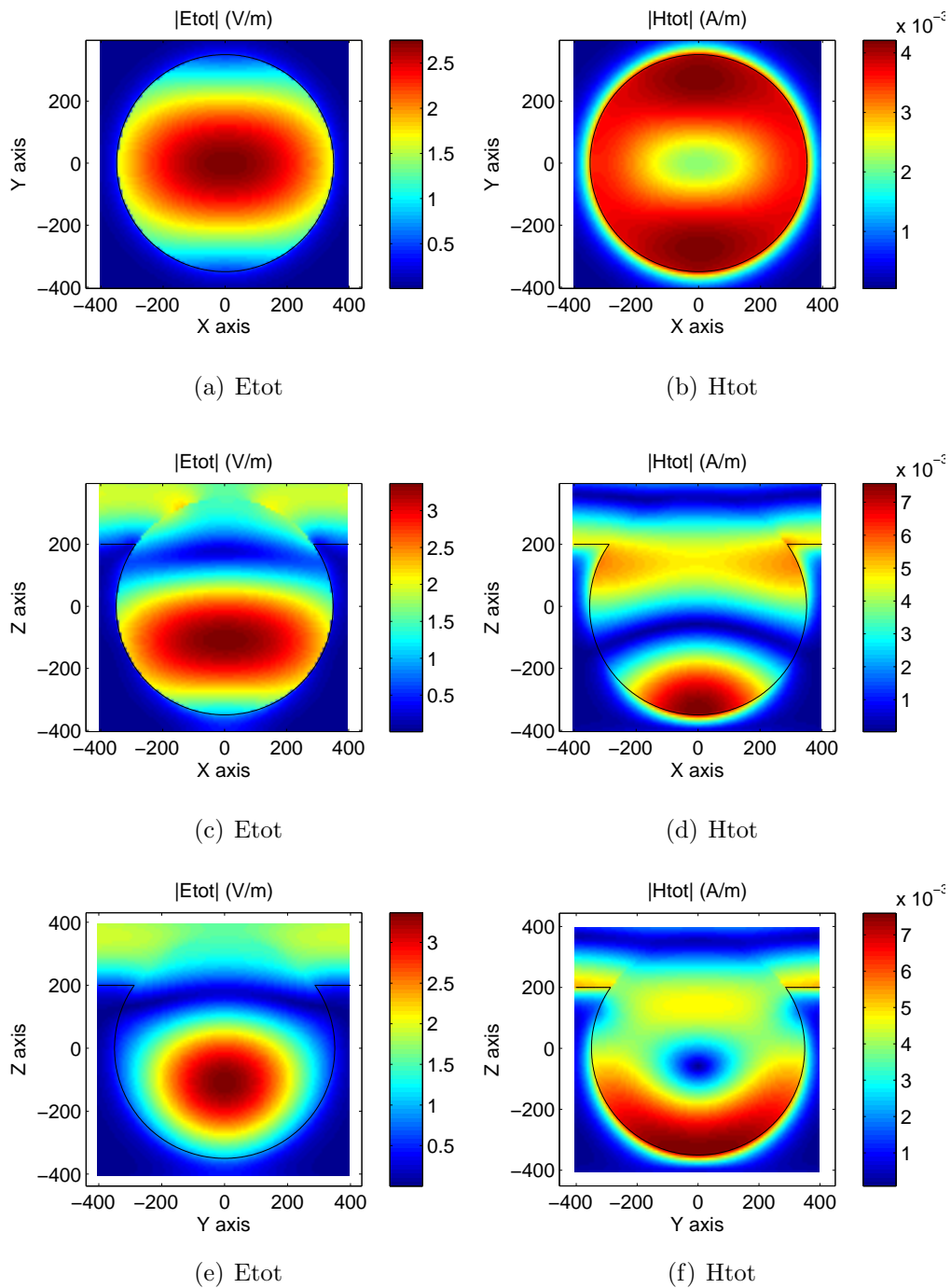


Figure 2.27: Absolute value of the total Electric and Magnetic field, on the three main planes XY, XZ and YZ cutting through the sphere.

Cylindrical hole

The second example is a single hole in a dielectric layer surrounded by air. The hole is assumed to be invariant along z , and has a circular cross section with radius 50 nm. As the structures we have in mind to model are nano-holes or nano-objects for optical applications this is not really a limitation and is realistic for actual devices. The thickness of the layer is 160 nm and the permittivity is 2.25. The considered wavelength is 400 nm. Note that the embedded object is a cylinder whose edges have been rounded with a radius of 20 nm (the total height of the rounded cylinder is 200 nm, see white dashed line in Fig. 4). The exact location and shape of the upper and lower faces of the cylinder doesn't change the results as the hole is assumed to be filled by air as are the substrate and superstrate, but it allows us to avoid sharp edges that may cause numerical instabilities. We have checked that 1632 sources and 800 points on the object give satisfactory results. Fig 2.28 shows the map of the modulus of the electric and magnetic fields when the structure is enlighten by a plane wave incident from the top with normal incidence and linearly polarized along the x -axis.

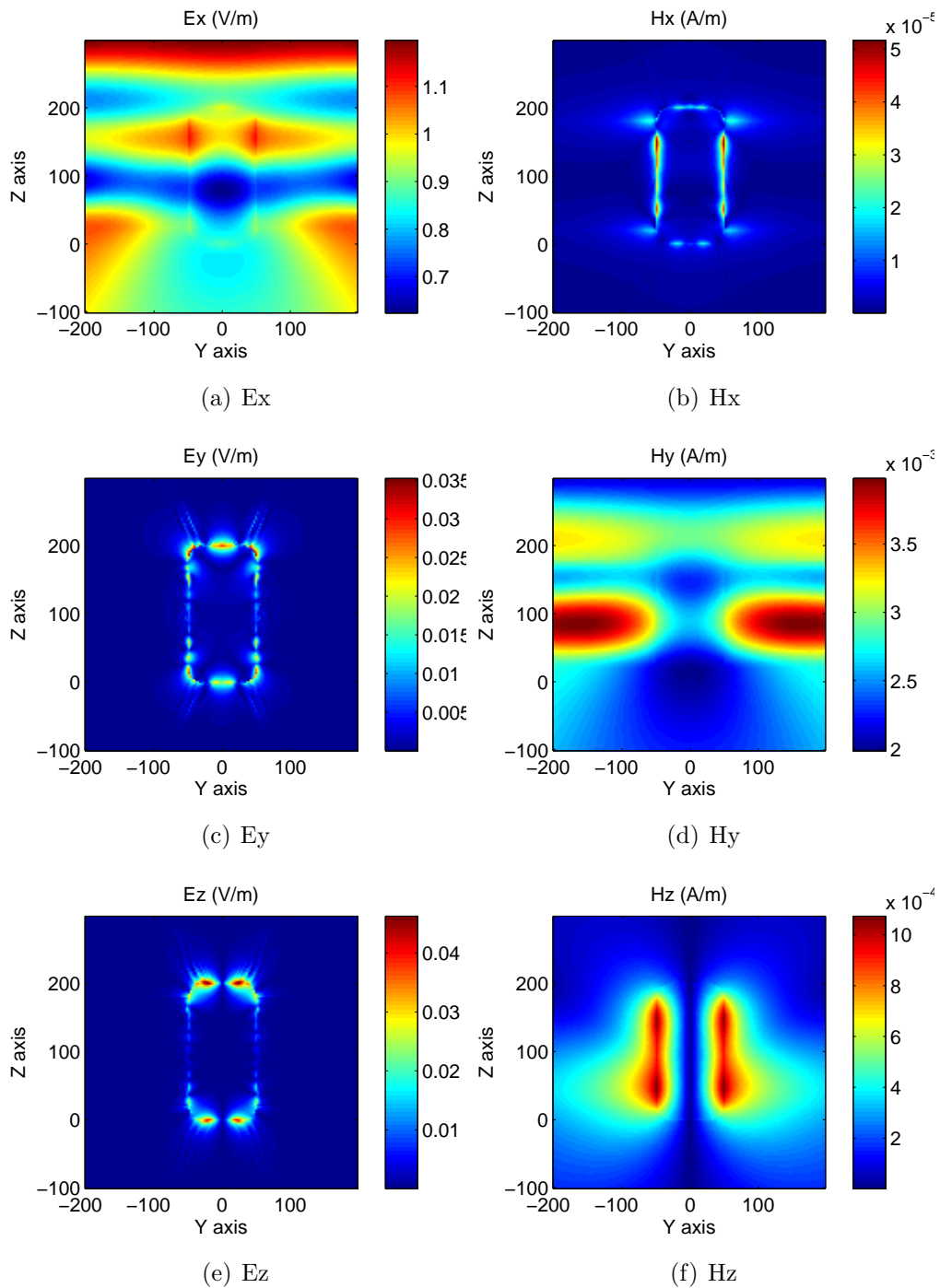


Figure 2.28: Electric and Magnetic field components on the YZ plane. It should be recalled that the incident planewave is X polarized.

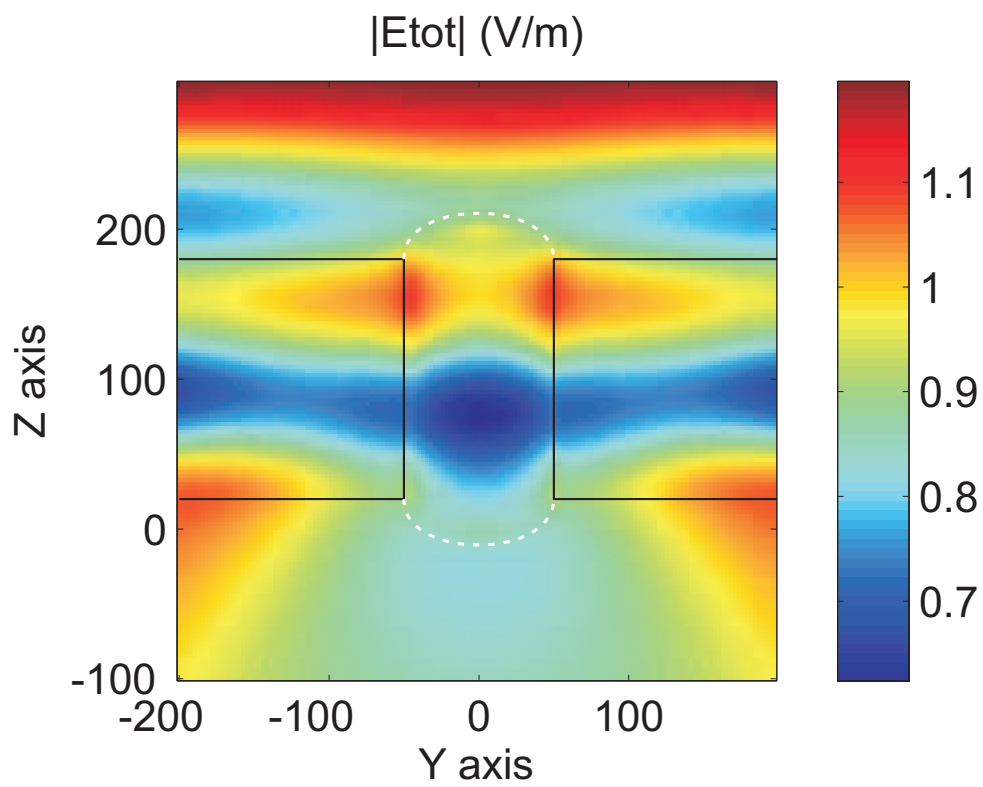


Figure 2.29: Detail on the shape used to model a cylindrical hole. Rounded edges are present to avoid possible instabilities due to sharp corners.

Chapter 3

A compact planar antenna

3.1 Introduction.

Satellite communications are widely used nowadays in several sectors of human activities. There are several reasons why they are preferred over other kind of connections. Amongst the others, a single satellite can cover at once millions of users (theoretically, almost the entire earth could be covered by only 3 of them), even those otherwise difficult to reach with wired connections. Moreover, some applications couldn't be realized otherwise (GPS, remote sensing). This is why the demand for satellite communication capacity is constantly increasing: GPS, mobile satellite telephones, remote monitoring systems, digital and analog television, telephony, digital radio and many other new satellite applications are all pushing the limits of actual satellite devices.

But the growing demand for ever-more bandwidth and space segment is being offset by new satellites and by a more efficient use of existing transponder capacity, achieved by improving the performance of all the devices involved in the earth-satellite link, amongst the others, the antennas.

The most common type of antenna used on satellites is multi-beam antennas. Such devices are able to cover very large zones of the earth with a high level of signal. They are normally made of a number of smaller, similar antennas, each of them able to cover a small area (called spot). By putting them side by side, an array is created which is able to cover a large area with several spots, through a direct radiation or via the use of (usually parabolic) reflectors.

In order to efficiently superpose these spots, each antenna must satisfy certain constraint, the main one being to have small lateral dimensions. Moreover, they must be able to handle high powers (the power loss in the

earth-satellite link is dramatic), be light (the heavier the satellite, the higher the launch cost) and limit the use of dielectric materials (performance degradation).

The project described in this report is included in this scenario and it regards the design of a compact planar antenna for satellite application. This project is a cooperation between Alcatel Space France and the Institut Fresnel, Université Paul Cézanne Aix-Marseille III. The detailed requested specifics are:

- Planar antenna with lateral dimensions $2.8\lambda \times 2.8\lambda$.
- High surface efficiency ($> 90\%$).
- Single access.
- High power handling.
- Bandwidth of at least 2.5%.
- Low level of crosspolar radiation.
- Low level of side lobe levels.

3.2 Fundamental antenna parameters

We present here a brief resume on the main antenna parameters that will be used through this report.

The electromagnetic field radiated by every antenna satisfies, in the far zone (Fraunhofer zone), the following properties:

- the electric (\mathbf{E}) and magnetic (\mathbf{H}) fields propagate as a spherical wave, that can be locally described as a uniform planewave propagating in the radial direction $\hat{\mathbf{r}}$.
- \mathbf{E} and \mathbf{H} are perpendicular to each other and to the propagating direction. Their modules decrease as $\frac{1}{r}$ and the ratio between them is constant and equal to the characteristic impedance of the medium $\eta = \sqrt{\frac{\mu}{\epsilon}}$

The **Power Density** [W/m^2] radiated from an antenna is given by the module of the Poynting vector \mathbf{P} , defined as

$$\mathbf{P}(r, \theta, \phi) = \frac{1}{2} \mathbf{E}(r, \theta, \phi) \times \mathbf{H}^*(r, \theta, \phi) = \frac{1}{2\eta} \frac{|\mathbf{E}(\theta, \phi)|^2}{r^2} \hat{\mathbf{r}} \quad (3.1)$$

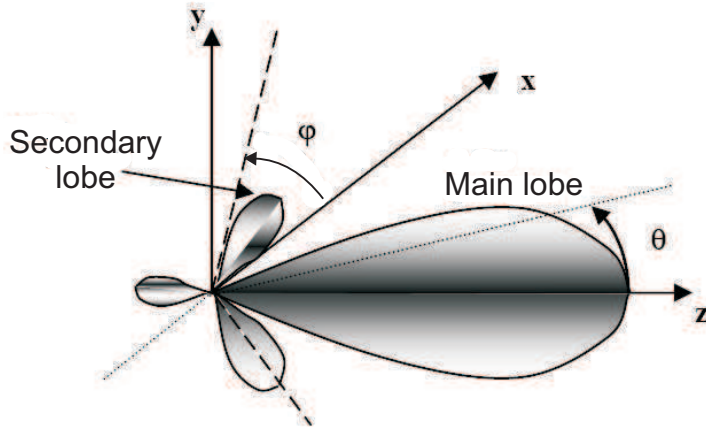


Figure 3.1: A radiation pattern.

which decreases as $\frac{1}{r^2}$. It is convenient to define a quantity which is independent from the distance from the antenna, called **Radiation Intensity** [$W/srad$],

$$U(\theta, \phi) = r^2 P(r, \theta, \phi) \quad (3.2)$$

that represents the power radiated in direction (θ, ϕ) per unit of solid angle. The **Total Power** radiated from the antenna can be obtained by integrating $U(\theta, \phi)$ as

$$W_t = \oint_S P(r, \theta, \phi) dS = \oint_S \frac{U(\theta, \phi)}{r^2} dS = \oint_{4\pi} U(\theta, \phi) d\Omega \quad (3.3)$$

$U(\theta, \phi)$ characterizes the directional properties of the antenna and can be used to plot its **Radiation Pattern** (Fig. 3.1). For directive antennas, usually a main lobe is present, in the direction where the radiation is concentrated, and minor secondary lobes. The ratio between the amplitude of the highest secondary lobe(s) and the amplitude of the main lobe is called **Side Lobe Level (SLL)** and it is usually measured in dBs. By cutting the radiation pattern through sections at constant ϕ or θ , bi-dimensional charts can be obtained called **Antenna Patterns**. For linearly polarized antennas, two cuts are most important:

- E plane: plane containing both the direction of maximum radiation and the electric field \mathbf{E}
- H plane: plane containing both the direction of maximum radiation and the electric field \mathbf{H}

In each of these planes, two different radiation patterns can be defined: the **Copolar** radiation, which represents, in the E plane (resp. H plane), the component of the e.m. field with electric (respectively magnetic) field component lying in the E (resp.H) plane. Viceversa, the **Crosspolar** component represents, in the E plane (resp. H plane), the component of the e.m. field with electric (respectively magnetic) field component orthogonal to the E (resp.H) plane.

The antenna **Directivity** is useful to express the ability of the antenna to concentrate the radiation in one direction, with respect to an isotropic antenna that radiates the same power W_t .

$$D(\theta, \phi) = \frac{U(\theta, \phi)}{U_{iso}} = \frac{U(\theta, \phi)}{W_t/4\pi} \quad (3.4)$$

The **Gain** is a very similar quantity which is instead defined with respect to the power W_{in} which *enters* the antenna.

$$G(\theta, \phi) = \frac{P(r, \theta, \phi)}{W_{in}/4\pi r^2} = \frac{U(\theta, \phi)}{W_{in}/4\pi} \quad (3.5)$$

The powers W_t and W_{in} differ only for the power losses possibly present in the antenna. For lossless antennas, Directivity and Gain are synonymous: this is the case of the antenna presented in this report, where the two terms will sometimes be present, with the same meaning. It must be noticed how these quantities are usually expressed in dB following the definition (equally valid for D and G):

$$G_{dB} = 10 \log_{10}(G). \quad (3.6)$$

Very often, Gain and Directivity are normalized with respect to their maximum value, in such a way to have a value of 0dB in the direction of maximum radiation.

For aperture antennas, another important parameter related to directivity is **Surface efficiency**. It is calculated in relation to the radiation characteristic of a uniformly illuminated aperture on a ground plane. For such antennas, the maximum directivity is given by

$$D^{uniform} = \frac{4\pi}{\lambda^2} A_p \quad (3.7)$$

where A_p is the physical area of the antenna. For any other aperture antenna, the maximum directivity is smaller. Thus, for an antenna with maximum directivity D_0 , a surface efficiency ϵ_{ap} can be expressed as

$$\epsilon_{ap} = \frac{D_0}{D_{uniform}} \quad (3.8)$$

The Surface efficiency is a measure of how efficiently the physical area of the antenna is utilized.

Other fundamental parameters are defined in regard to the antenna impedance matching. Normally in fact, not all the power available from the generator can enter the antenna and be radiated, but only a fraction of it. We are naturally interested to maximize this fraction. When we consider the antenna attached to a transmission line, as in Fig. 3.2, we know that there are incident current and tension waves that can be expressed like

$$V(l) = V^+ e^{j\beta l} + V^- e^{-j\beta l} \quad (3.9)$$

$$I(l) = \frac{V^+}{Z_0} e^{j\beta l} + \frac{V^-}{Z_0} e^{-j\beta l} \quad (3.10)$$

The **Reflection Coefficient** in $l = 0$ corresponds to the \mathbf{S}_{11} parameters of the Scattering matrix representation of a two-port junction, and it's defined as

$$S_{11} = \Gamma(0) = \frac{V^-}{V^+}. \quad (3.11)$$

It represents the incident wave reflection at the antenna as a fraction of the incident one. If one wants an index of the *power* reflected at the antenna, one could use the following (in dB)

$$10 \log_{10} \left| \frac{V^-}{V^+} \right|^2 = 20 \log_{10} \left| \frac{V^-}{V^+} \right| = 20 \log_{10}(S_{11}). \quad (3.12)$$

With such a definition, $S_{11} = -3dB$ corresponds to a 50% of power reflection, $S_{11} = -10dB$ corresponds to a 10% power reflection, and so on.

It must be noticed how a low value of S_{11} does not necessarily imply a well-matched antenna. Instead, it is a necessary prerequisite to the design of an appropriate matching device, which is not treated in this report.

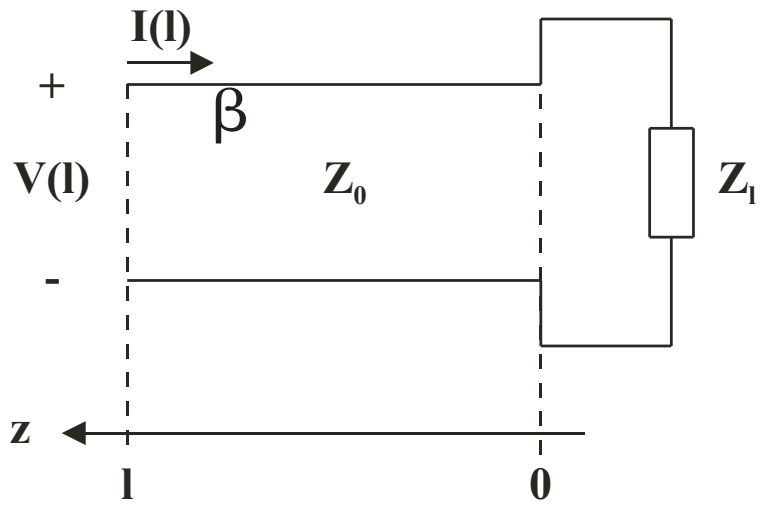


Figure 3.2: Schematic representation of a transmission line attached to a complex load (possibly representing an antenna), with incident tension and current waves.

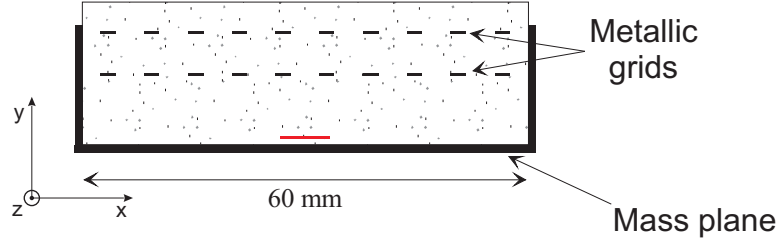


Figure 3.3: 2D model for the cavity antenna. The model it is based on, is a Fabry-Perot cavity, around 5 times larger in the x direction. Notice that this structure is invariant in the z direction.

3.3 Initial configuration: Fabry-Perot antenna.

In order to simplify the project and define some of the several variables involved in the design, a 2D model was initially created. The structure described in Fig. 3.3 shows this model.

It is inspired by the antenna described in [25]: a Fabry-Perot cavity, whose mirrors are constituted by parallel wires or strips designed (distance, wires diameter or strips width) in such a way to have the desired reflection coefficients. A source is placed in proximity of the mass plane (a patch or an open ended waveguide). This kind of antenna is known to give a high directivity, at the cost of a quite large surface (around 10λ). In order to obtain a compact antenna, the large Fabry-Perot cavity is "truncated", as shown in Fig. 3.3, by means of two metallic walls in such a way to obtain the desired dimension of 2.8λ . Since the antenna is designed to work at 14 GHz, its size is 60 mm.

This structure has been initially simulated by means of a 2D rigorous modal method using the S-matrices of each scatterer (the structure is divided in several rectangular scatterers)[26]. The same method has been used to optimize parameters such as the total number of grids, the widths of the strips or wires and the distance between these latter and the mass plane. All the optimizations have been done with the aim of obtaining a high directivity. At this stage of the project, no considerations on impedance matching are done.

Since the aim is to get a surface efficiency of $\epsilon_{ap} \sim 90\%$, the 3D directivity is given by

$$D_{3D} = \epsilon_{ap} \frac{4\pi(2.8\lambda)^2}{\lambda^2} = 89 \quad (3.13)$$

which, using approximate formulas for directive antennas (§2.5, [27]), gives for the principal radiation lobe a half-power beamwidth $\Delta\theta$ equal to

$$D_{3D} = 89 = \frac{4\pi}{\Delta\theta^2} \implies \Delta\theta = 21.5^\circ \quad (3.14)$$

that, in the 2D case, corresponds to a targeted directivity of

$$D_{2D} = \frac{2\pi}{\Delta\theta} = 16.7 \quad (3.15)$$

The grid is made of a periodical arrangement of infinitely conducting strips, with period d fixed and strips width w . The thickness of the strips is equal to 0.14 mm, which corresponds to the thickness of the metallic plate used to etch the grid in the experiment. In the numerical optimization, the parameters are the grid position (distance h to the ground plane) and the width of the strips w . The cost function used for the optimization is aimed to give a directivity as close as possible to a given D_{goal} in a given frequency range. This range is chosen to be 5%, centered on 14 GHz. We have used $d = 5.8$ mm, and in that case the result of the optimization is $w = 2.1$ mm, and $h = 10.9$ mm. The maximum directivity that we obtained in this configuration is shown in figure 3.4 and though not optimal, was considered a good starting point to build a prototype and to test the validity of our approach.

From this 2D model, a 3D one has been derived, by simply truncating the 2D cavity in the transversal direction in such a way to obtain a square cavity. A second set of parallel strips has been added, orthogonal to the first one, thus obtaining a regular grid, see Fig. 3.5. A patch antenna, appropriately designed to resonate in the frequency band of interest¹, has been added on the mass plane to constitute the excitation.

This antenna has been built and measured in the anechoic chamber of the Institut Fresnel, showing an almost perfect coincidence with the simulations (see Fig.3.6). While the results in terms of directivity and radiation pattern are good, this antenna suffers from a very poor impedance matching, as Fig. 3.7 shows. This result is not surprising, because for this prototype impedance matching has never been included as a goal of the optimization.

¹The patch was initially designed assuming it was placed in the free space. The interaction between the cavity and the patch has been investigated once the prototype has been built.

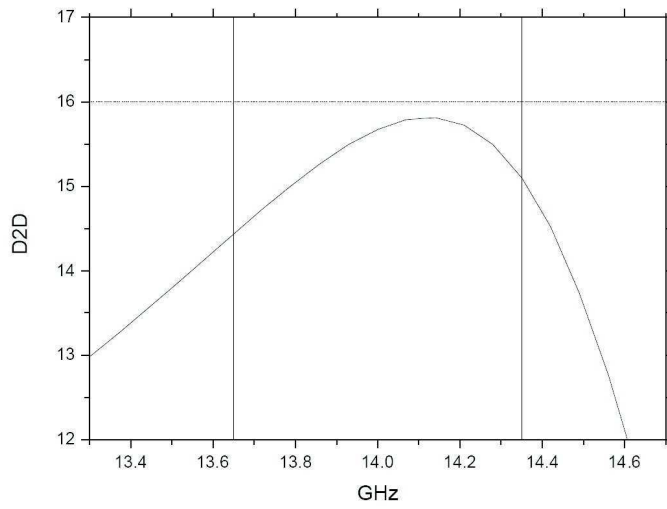


Figure 3.4: 2D directivity, best optimization result with one grid. The two vertical lines delimit the frequency range.

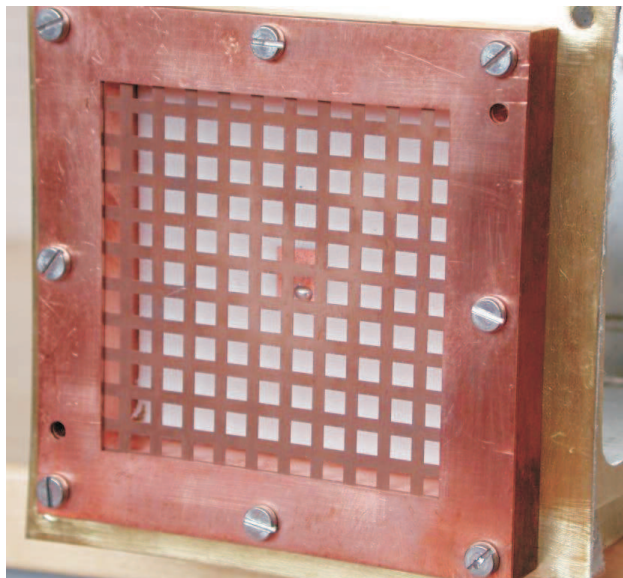


Figure 3.5: The cavity antenna excited by a patch.

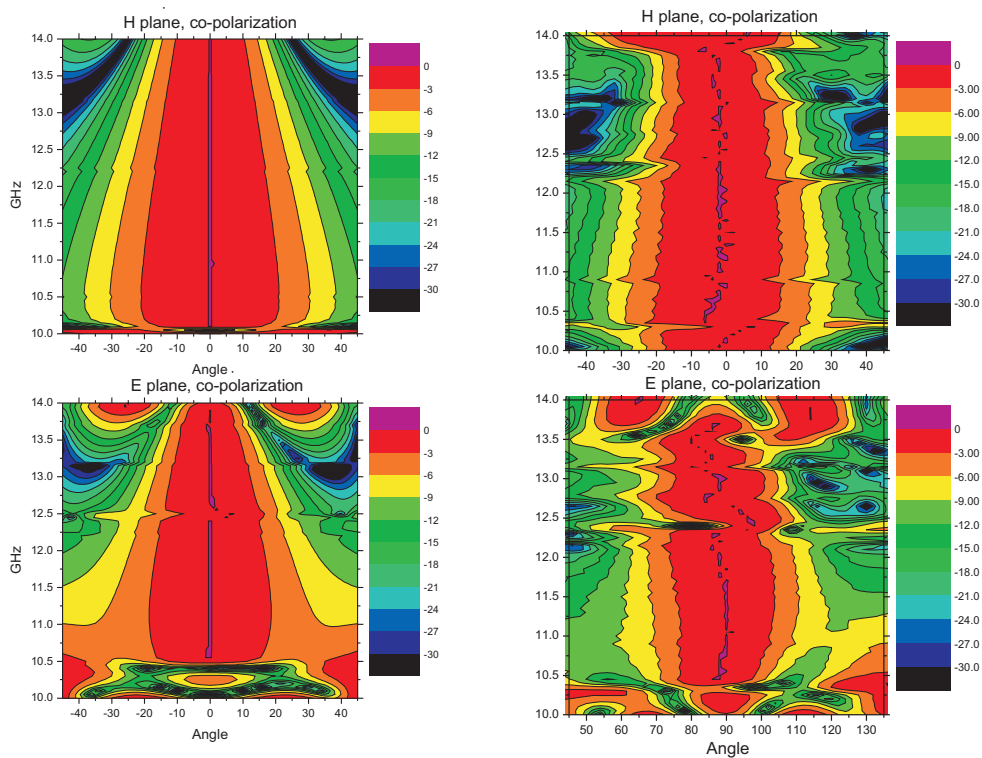
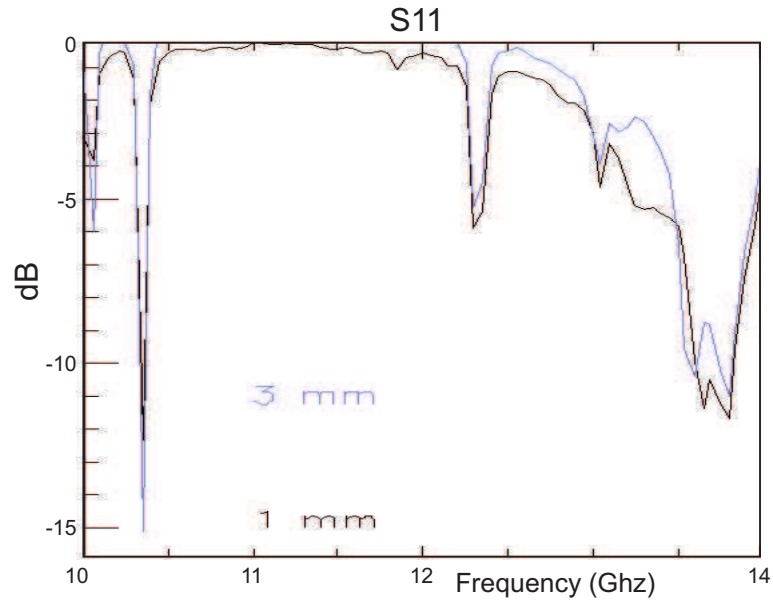
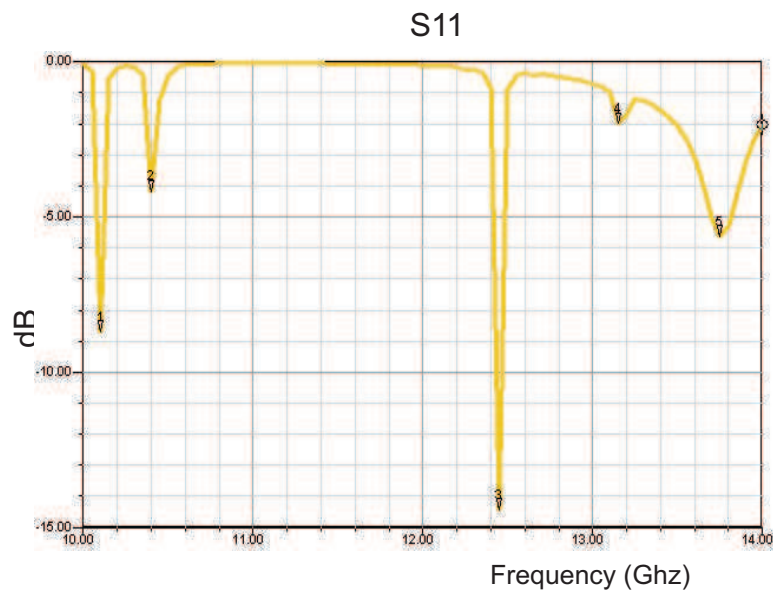


Figure 3.6: Comparison between simulations(left) and measurements(right) of the antenna shown in figure 3.5. Only copolar components of the fields are shown. These plots are produced by normalizing radiation patterns *independently for each different frequency*. Thus, the 0dB level at a given frequency is not comparable, in absolute value, to the 0dB value at a different frequency.



(a) Measures (black line).



(b) Simulations

Figure 3.7: S_{11} parameter, in dB, versus frequency, showing the poor impedance matching of the antenna.

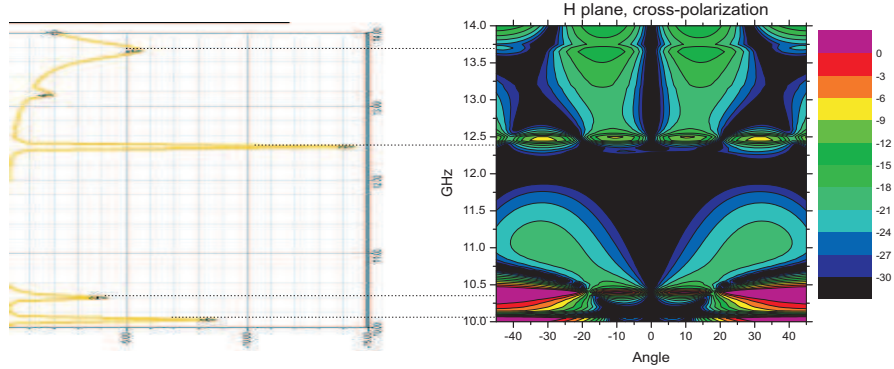


Figure 3.8: Relation between peaks in S_{11} and crosspolars level.

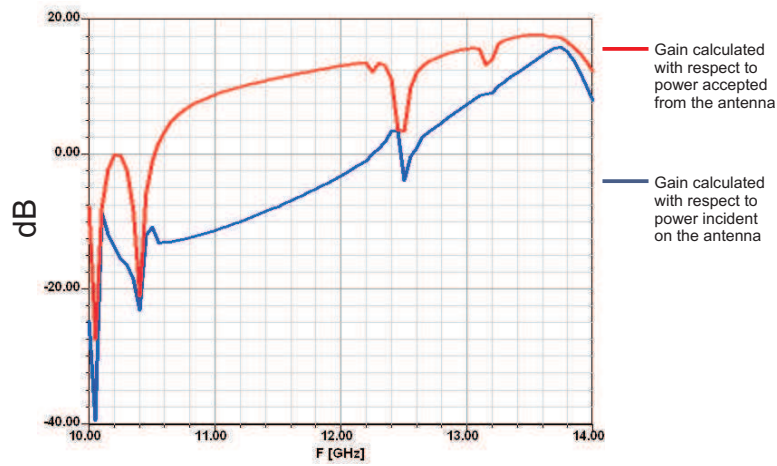
3.3.1 First conclusions

This experience showed how the concept of a strip grating cavity-backed antenna is indeed promising: a planar directive antenna can be obtained with compact size. The behavior of the cavity, though, and its interaction with the source had to be further investigated, with the aim of a higher directivity and, most of all, a good impedance matching.

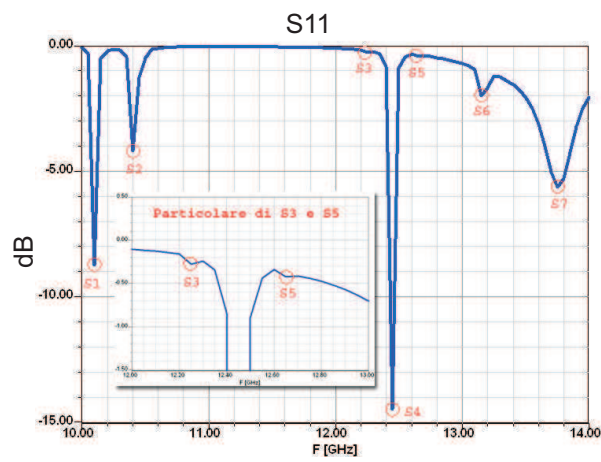
From this preliminary results, we could understand that the size of the cavity plays a fundamental role for both directivity and impedance matching. In particular, the S_{11} measurements revealed the presence of phenomena that can be interpreted as resonances of the cavity. As Fig. 3.7 illustrates, at certain frequencies the power absorbed from the cavity (and then converted to radiated power) has a maximum (minimum values for S_{11}). Moreover, these peaks are in strict relation with negative peaks in the Gain curve, changes in the radiation pattern and a sudden increase in the level of crosspolars, as Figs. 3.8 and 3.9 show. All these observations suggest a multi-resonant nature of the cavity.

Once the multi-resonant nature of the cavity has been revealed, it remains to understand what mode corresponds to each peak. In order to do so, a first easy test is to run several simulations, varying one dimension of the cavity at a time. In such a way, one can understand if a given mode is resonant (or multi-resonant) along one, two or all three sides of the cavity.

One results of this kind of investigation is shown in Figures 3.10, where the frequency of each S_{11} peak is shown as a function of cavity sides (always keeping the cavity square and for the same cavity height). It appears evident



(a) Gain versus frequency



(b) S_{11} versus frequency

Figure 3.9: Gain and S_{11} curves, showing typical corresponding peaks at the same frequencies.

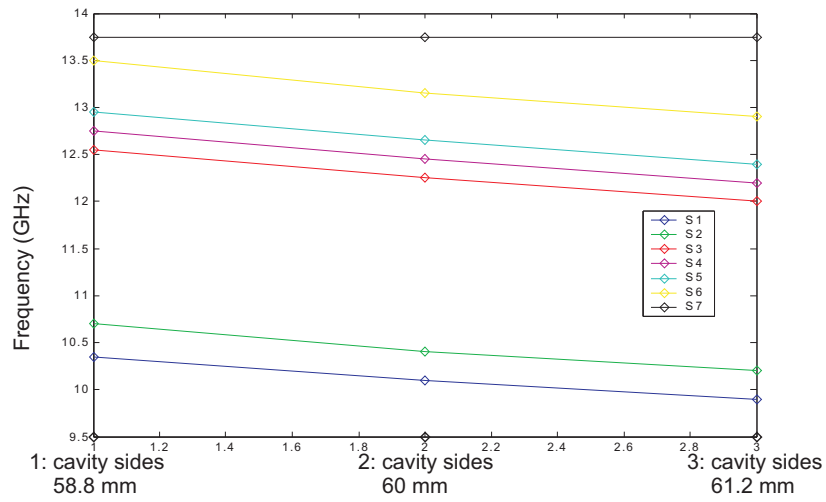


Figure 3.10: S_{11} peaks migration with respect to cavity size.

that the peaks from S1 to S6 are dependent from the cavity sides (shift to lower frequencies for bigger size), while S7 seems unaffected from this parameter. Our hypothesis is that S7 corresponds to a mode whose resonant frequency depends only from the cavity height (distance mass plane-grid).

3.4 A 3D finite elements method

In order to continue our investigation and to deepen the observations made so far, a fully 3D numerical method is needed, which is able to include all the parameters of interest of our antenna, and which is able to visualize the field distribution inside the cavity.

We thus chose to use a commercial software based on the finite element method. It includes a fully 3D CAD², which allowed us to model in detail our antenna and to see how a change in the design could affect the performance.

The finite element method works by dividing the model into several small homogeneous pieces (finite elements), where simple approximated field expressions are used. The total number of finite elements depends on the size of the model and on the size of the smaller details. As this number grows, the computational resources needed to solve the problem grow very rapidly, so it's very important to keep it as low as possible.

In our case, a model of the whole antenna (we remember, approximately $2.8\lambda \times 2.8\lambda$) would produce a number of finite elements too high to be practically usable. Fortunately, we could exploit the intrinsic symmetry of the antenna by modeling only one quarter of the structure and using symmetry planes, thus proportionally reducing the number of finite elements and the computational resources needed. Figure 3.11 shows the model of the antenna and also introduces some modifications that have been requested from Alcatel with respect to the antenna shown in the previous sections. In particular, the patch excitation used so far has been substituted with a waveguide opening directly into the mass plane. This kind of excitation is preferable to a patch when, as in our case, high power handling is needed. Moreover, the guided access allows us to build an antenna with no dielectric components: this is an advantage for an antenna designed to be mounted on satellites, where dielectrics suffer from fragility and performance degradation.

3.4.1 New kinds of grid

At first, we wanted to investigate the effects of a different kind of grid, again obtained by orthogonally crossing two sets of parallel strips which are the result of 2D optimizations, with grids of 20 strips instead of the previous 10. A first optimization was run, with strips of constant width. A second, much more complex optimization, aimed to obtain grids with a variable strip width. Without going too much into the details of the optimization, we can say that the strip width has been described as a function of the x coordinate,

²Computer Aided Design

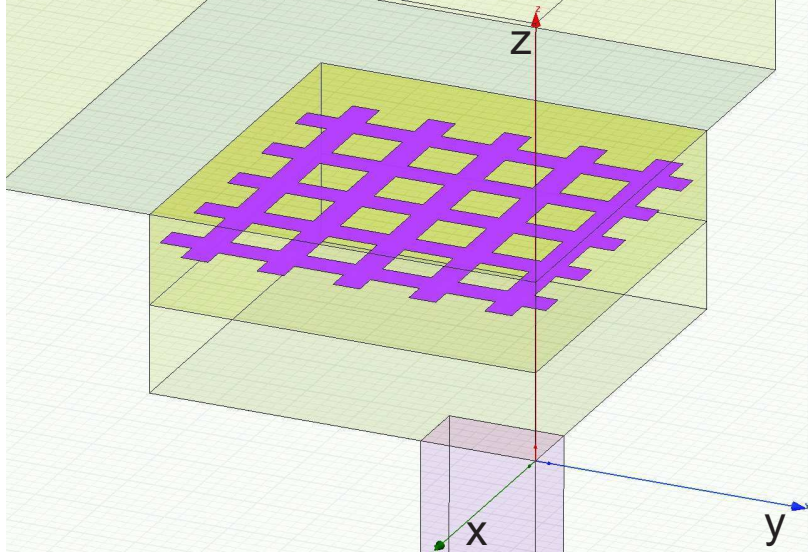


Figure 3.11: The model of the cavity antenna. Notice that only one quarter of the antenna is modeled by using symmetry planes, in order to reduce the number of finite elements and the computational resources needed. Plane yz has a "Perfect E symmetry" boundary condition, while plane xz has a "Perfect H symmetry" boundary condition (see Fig. 3.12).

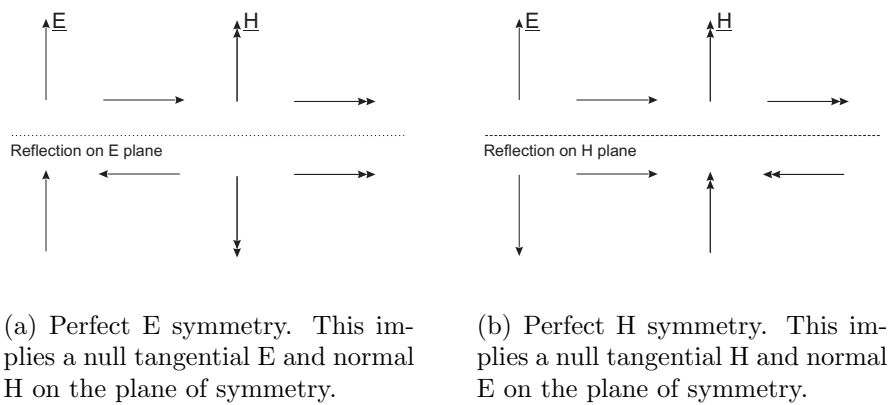


Figure 3.12: E and H symmetries boundary conditions.

and forced to satisfy a polynomial law. The cost function has been modified in such a way to penalize widths that are too small to be actually realizable. The distance between the grid and the mass plane has also been included in the parameters to be optimized.

It must be noticed also that, due to a change in the specifics requested from Alcatel Space, the whole antenna has been resized to work at 20 GHz and not at 14 GHz anymore. Taking Fig. 3.13 as a reference, the (x, y) dimensions of the cavity are, in the order, (42, 42)mm. The waveguide we used is a standard WR42, whose section (x, y) measures (4.32, 10.67)mm.

The two grids that we obtained are shown in Figure 3.13, followed by the results in terms of Gain and S_{11} . The parameters of the two grids are the following (for the VW grid, the measures are given from the cavity edge towards the center):

	CW	VW
Grid Height(mm)	11	10.8
Grid Step(mm)	2.1	2.1
Strip Width(mm)	0.65	0.1926 0.3561 1.0434 1.3278 1.1000 1.1047 1.2476 1.3716 1.3721 1.3242

The results of these simulations allowed us to make some fundamental observations. First of all, the frequency where the Gain is maximum is higher with the VW grid than with the CW (19.8GHz versus 19.4GHz, Fig. 3.14). The maximum value itself is around 1dB higher with the VW grid than with the CW one. Peaks in S_{11} and G are observed, similarly to the observations made at 14 GHz with the previous grids, but while with the CW grids some power enters the antenna around 19.5GHz, the VW grid produce an almost total reflection at all frequencies (Fig. 3.15).

These observations suggested us again to compare the behavior of the antenna to the one of a resonant cavity. In particular, one of our hypothesis is that the maximum Gain frequency corresponds to the presence of a given cavity mode, which is resonant in the z direction. In this case, the observed frequency shift could be related to the different cavity height. In fact, the

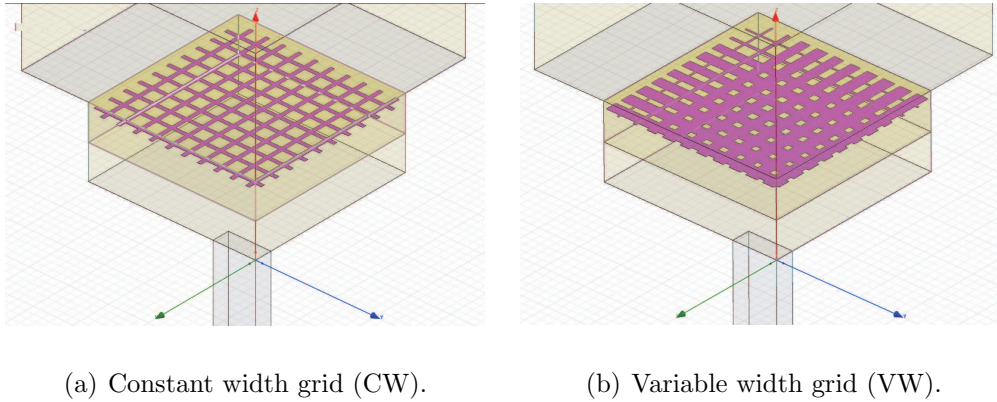


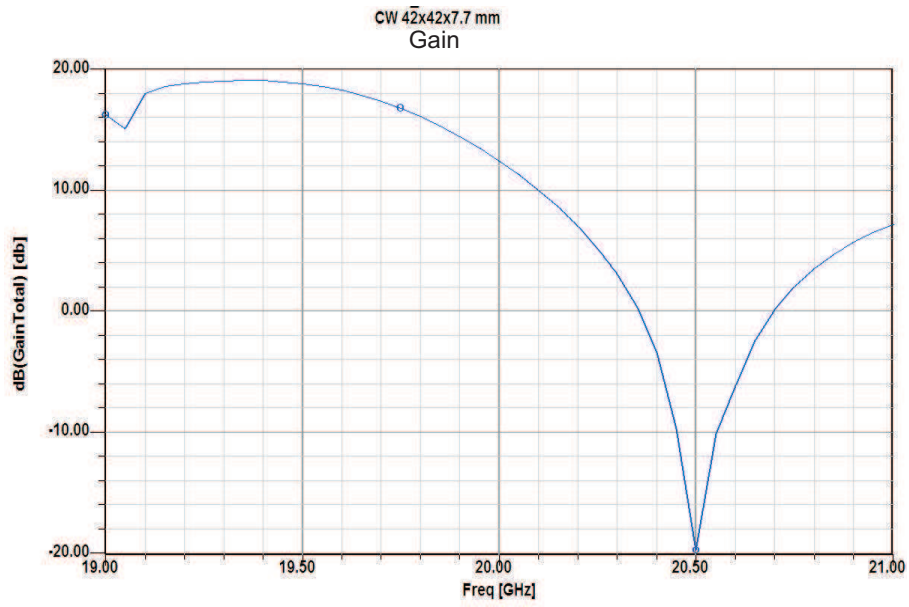
Figure 3.13: The new grids made of 20x20 crossed strips.

maximum Gain point has a 2% shift towards lower frequencies for a 1.8% thicker cavity.

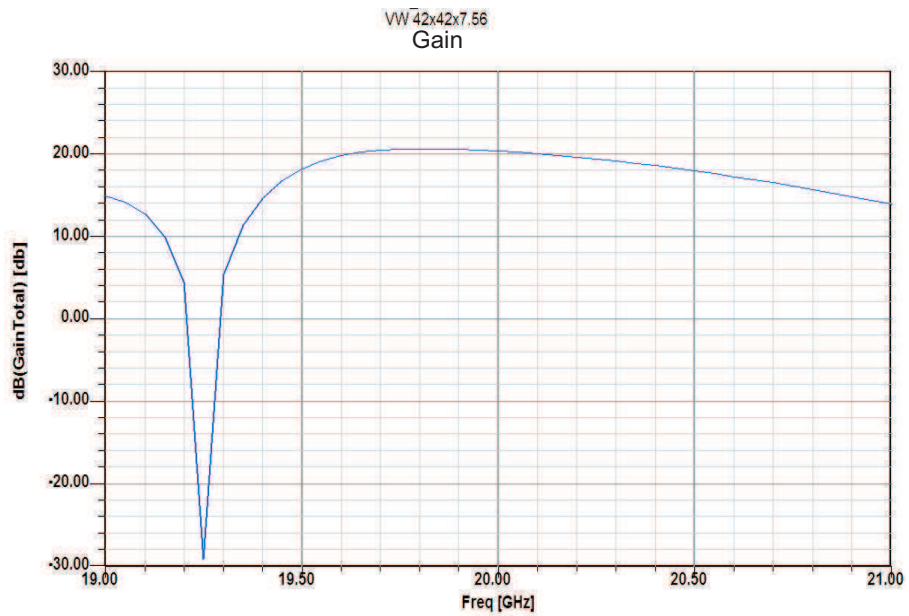
A second hypothesis is that the grid can be compared to a lossy wall: when losses are low (VW grid, with much thicker strips), the Gain is higher but a much lower power leaves the antenna in the form of radiation; when losses are lower, the gain is lower too, but more power is able to leave the cavity and be radiated.

We proceeded then to trace field charts inside the cavity, which are shown in Fig. 3.17 and Fig. 3.18 for the VW grid. They are traced at the frequency of 19.2 GHz (first minimum of gain and power absorption) and at 20.1 GHz (maximum gain). The field charts are evidently the ones of the modes TE₂₅₀ and TE₀₁₁.

It's the presence of the TE₀₁₁ mode that generates a good radiation pattern with a satisfying Gain (see Fig. 3.16). This mode in fact has the most uniform field distribution in the plane xy, and it generates a very constant illumination of the grid, which is fundamental to obtain a good Gain. On the opposite, the presence of the 250 mode is undesirable and should be avoided if possible.

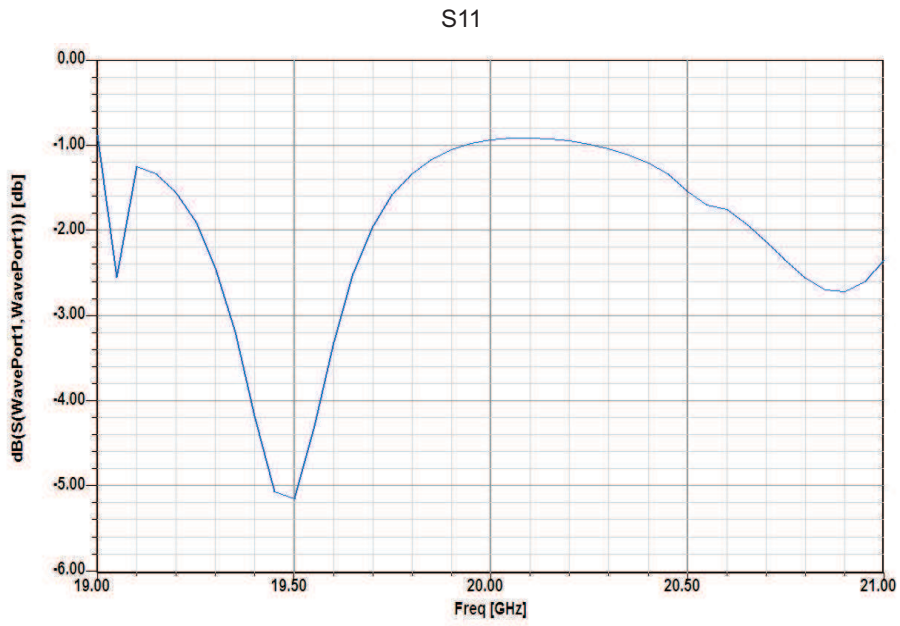


(a) Gain with the grid CW.

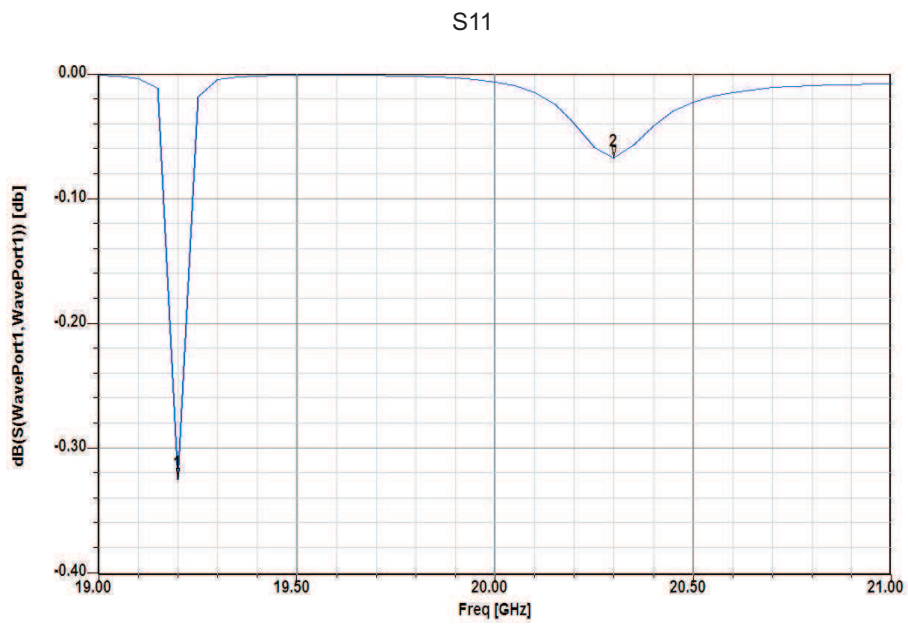


(b) Gain with the grid VW.

Figure 3.14: Gain with 20x20 crossed strips.



(a) S_{11} with the grid CW.



(b) S_{11} with the grid VW.

Figure 3.15: Power reflection with 20x20 crossed strips.

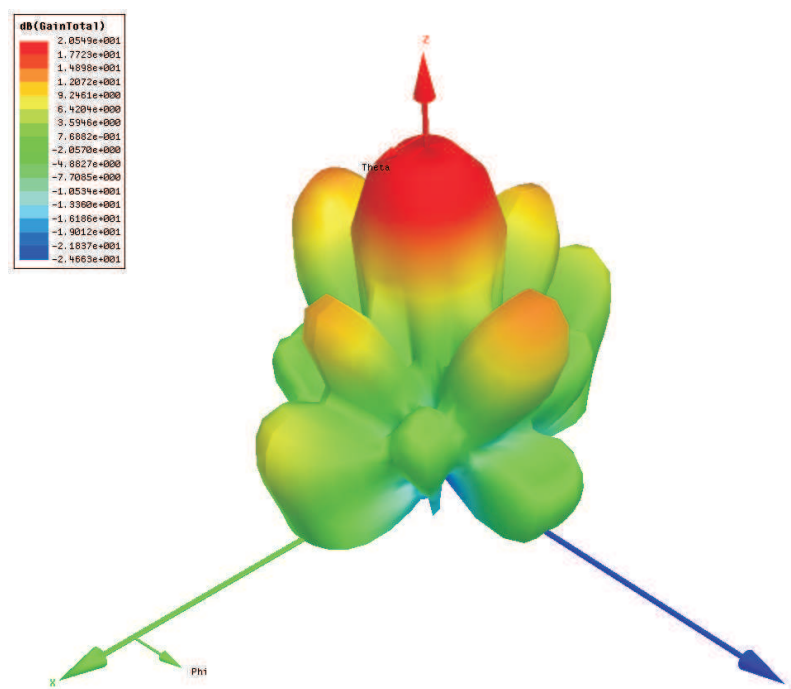
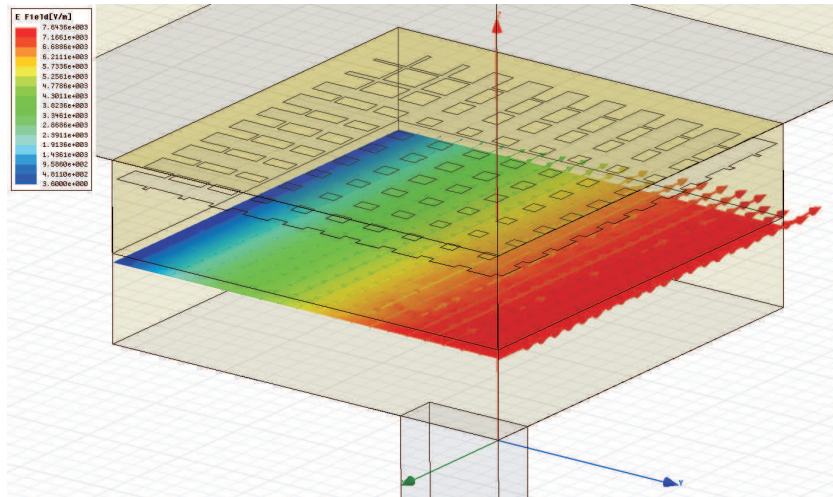
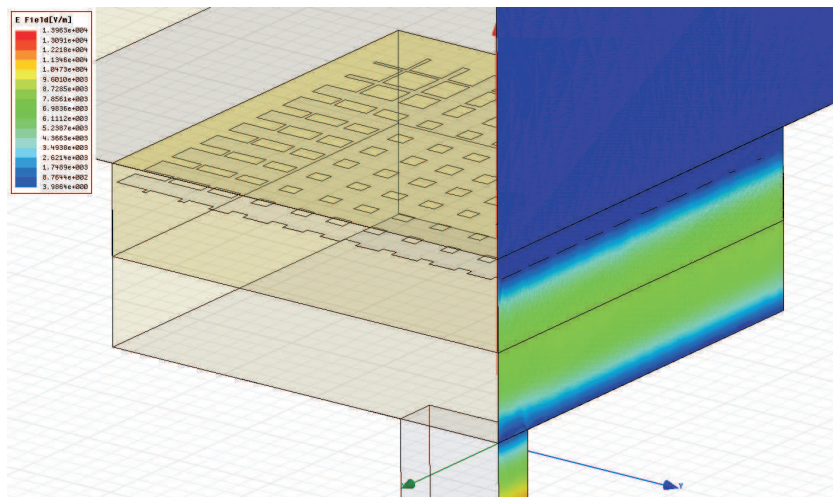


Figure 3.16: 3D Polar plot of the radiation pattern obtained using the VW grid.

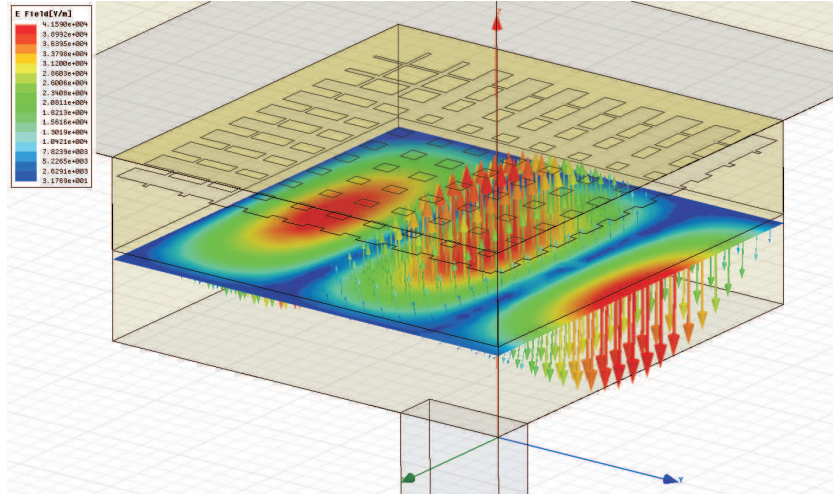


(a) Electric field amplitude and direction on a xy cut at $z=3.78\text{mm}$.

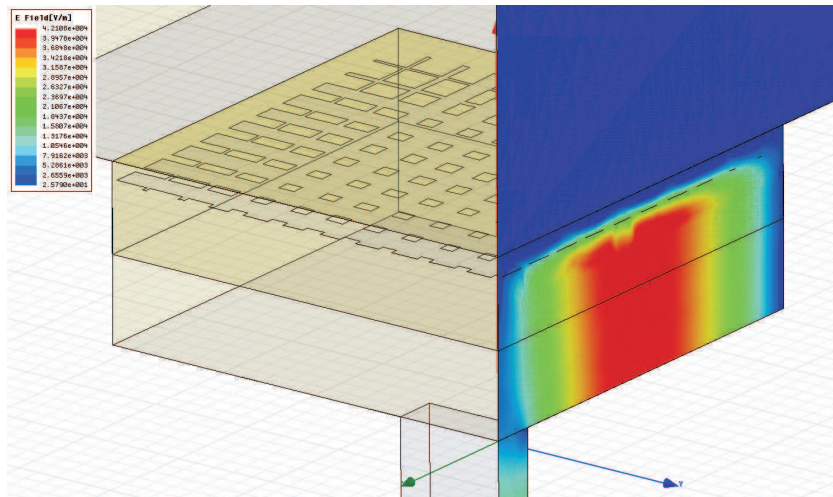


(b) Electric field amplitude on a xz plane in $y=0\text{mm}$.

Figure 3.17: Electric field distribution at 20.1 GHz inside the cavity. It can be identified with a TE₀₁₁ mode.



(a) Electric field amplitude and direction on a xy cut at $z=3.78\text{mm}$.



(b) Electric field amplitude on a xz plane in $y=0\text{mm}$.

Figure 3.18: Electric field distribution at 19.2 GHz inside the cavity. It can be identified with a TE₂₅₀ mode.

3.5 A method to dimension the cavity.

For a perfectly metallic cavity, the cut frequencies of each mode can be easily calculated analytically starting from the modes of a rectangular waveguide. For the details of this calculation, see Appendix C. It is straightforward to implement such formulas into a spreadsheet and thus calculate the cut frequencies of each mode that could be supported from a perfectly metallic cavity of arbitrary size in a certain frequency range.

If we make this calculation for a perfect cavity of the same size of our antenna, in the range 19-21GHz, we find an almost perfect match for modes 011 and 250, as the following table shows.

x	y	z	Perfect cavity	Cavity antenna
2	5	0	19.233	19.2
5	2	0	19.233	
0	0	1	19.841	
0	1	1	20.160	20.1
1	0	1	20.160	
4	4	0	20.203	
1	1	1	20.474	
3	5	0	20.825	
5	3	0	20.825	

All the modes calculated analytically and not present in the simulations, do not get excited inside the antenna due to the nature of the exciting field. The waveguide aperture on the bottom of the cavity has in fact an x-polarized field, which is constant in the x direction and sinusoidal in the y direction, with a maximum in $y=0$. This allows, for example, only modes with an odd symmetry in the y direction.

This strong analogy between the cavity antenna and a closed, metallic cavity is a precious tool that can help us design individually each side of the antenna. In this way, we can work on the y and z dimensions of the antenna to excite the desired mode TE₀₁₁ at 20GHz. The cut frequency of this mode in fact is independent from the x dimension. This gives us a degree of freedom that can be used to move the undesired TE₂₅₀ mode (whose cut frequency instead depends also on the x size) away from the frequency range of interest.

With a longer x side, the TE₂₅₀ mode will be moved to lower frequencies. The following table shows the modes that are expected for a (44, 42, 7.56)mm cavity, together with what is found from the simulations on a similar antenna.

x	y	z	Perfect cavity	Cavity antenna
2	5	0	19.115	19.15
4	4	0	19.749	
0	0	1	19.841	
1	0	1	20.132	20.10
5	3	0	20.133	
0	1	1	20.160	
1	1	1	20.446	
6	0	0	20.455	
3	5	0	20.578	
6	1	0	20.764	20.70
2	0	1	20.980	

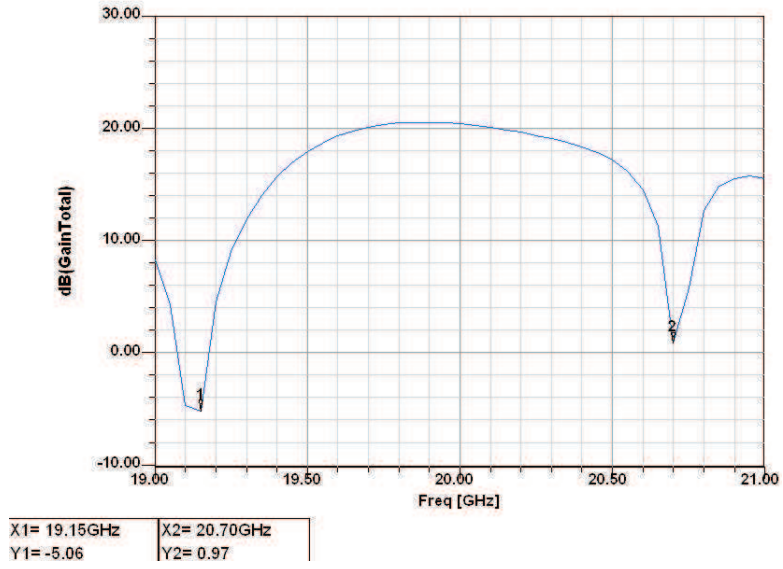


Figure 3.19: Gain obtained with VW grid, 44x42x7.56mm cavity.

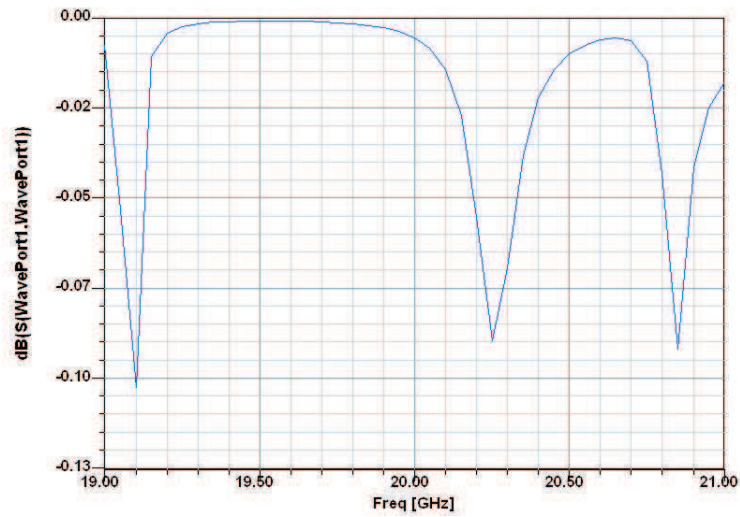


Figure 3.20: S_{11} obtained with VW grid, 44x42x7.56mm cavity.

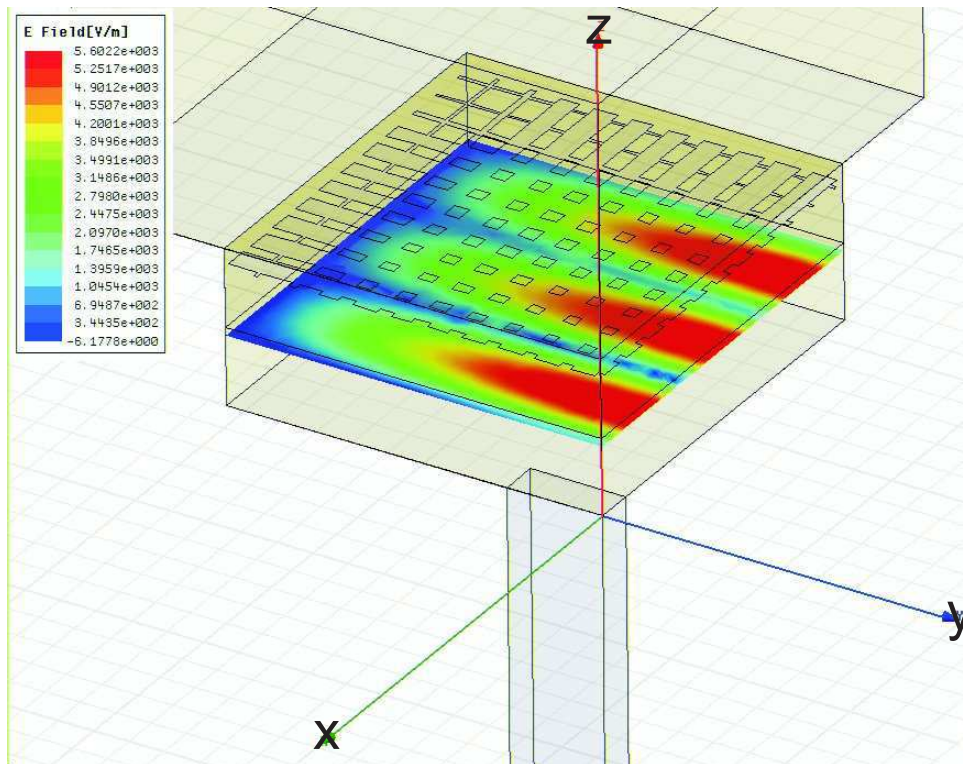
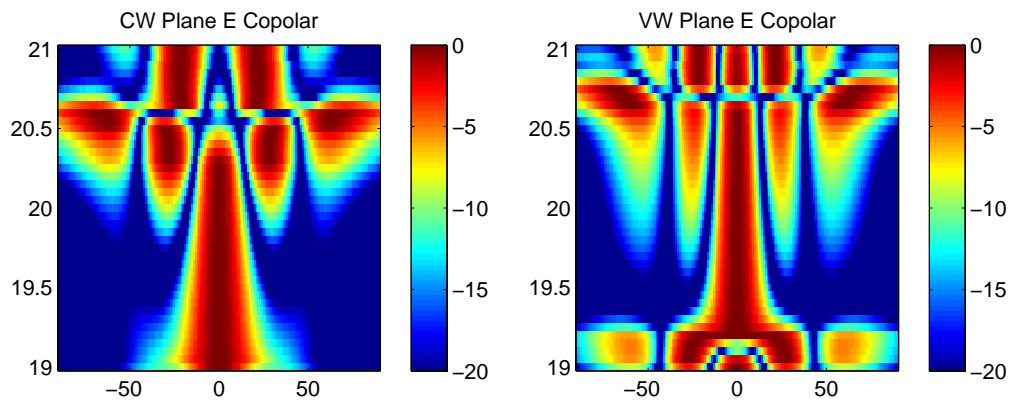
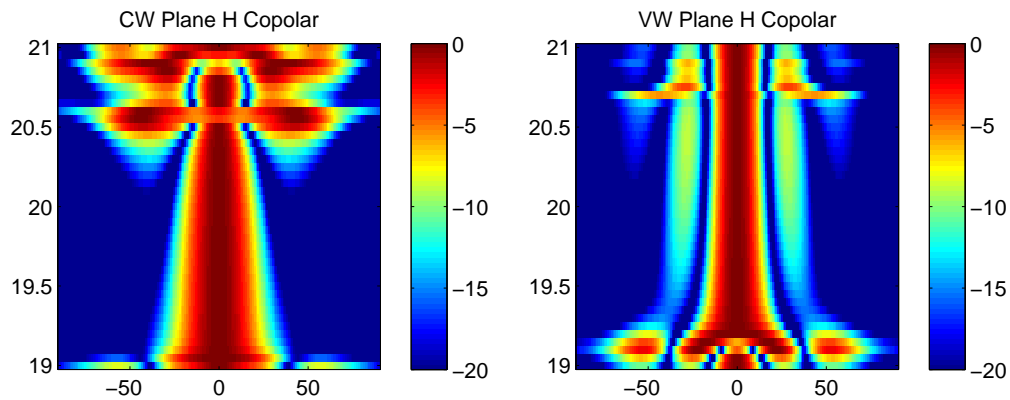


Figure 3.21: Mode TE₆₁₀ gets excited inside the antenna at 20.7 GHz.

Again the matching between the analytical calculation and the simulations is perfect. The same procedure has been applied to the case of CW grid, with similar results.



(a) CW Plane E copolar radiation pattern. (b) VW Plane E copolar radiation pattern.



(c) CW Plane H copolar radiation pattern. (d) VW Plane H copolar radiation pattern.

Figure 3.22: Radiation patterns for 20x20 strip grids, 44x42mm cavity. Grid CW shows a low Side Lobe Level ($< -20dB$) in a large range of frequencies.

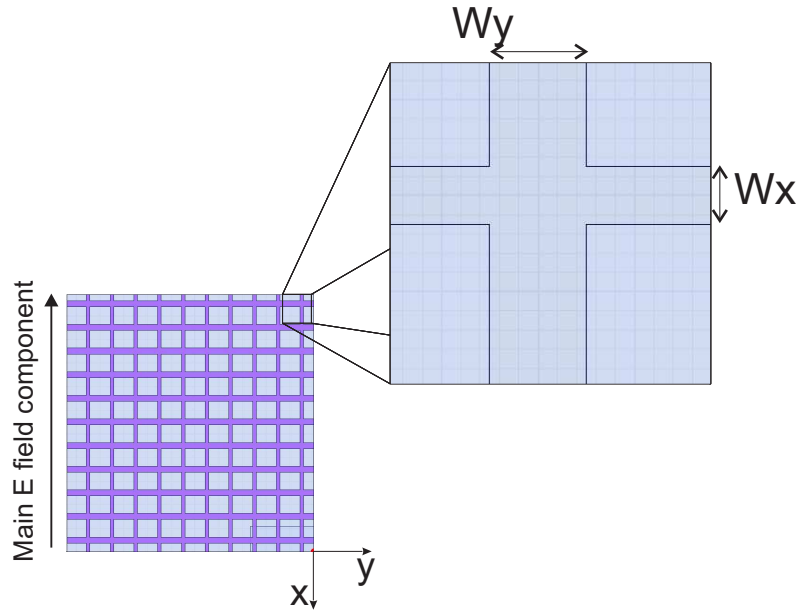


Figure 3.23: Optimization of strip widths separately along the x and y axis.

3.6 Grids for a better impedance matching

Now that we have a tool to correctly dimension the cavity, we focalize our attention on the grid and try to apply the observations done in the previous sections.

In particular, we know that the cavity mode we want to excite is the TE011, which doesn't have the same field distribution along x and y. So, there is no special reason to use a grid which has the same design along x and along y. Instead, we would like to design separately the strip widths along x and along y, trying to look for the best compromise between Gain and Impedance matching.

In order to minimize the number of parameters to be optimized, we worked on the type of grid CW, that is with a constant strip width. In this case though, the strip widths will be different along the x and the y directions. The choice of this grid is due to a lower side lobe levels exhibited in the radiation pattern (see Fig. 3.22) and to a slightly better impedance matching.

Two different parametric simulations are done: with reference to Fig. 3.23, a first simulation aims to optimize the value of W_y , keeping W_x constant to the 0.2mm used so far. W_y is the most important parameter, being

the width of the strips that are parallel to the electric field, the ones that interacts more strongly with the cavity field. W_x has a smaller influence on the behavior of the antenna, as already observed in the previous simulations, and its dimension mostly modifies the level of crosspolars and the impedance matching.

Once an optimum W_y is be found, a second simulation optimizes the value of W_x , keeping W_y constant. By reiterating this process, successive refinements are possible.

Figs. 3.24 and 3.25 show the Gain and S_{11} curves as a function of W_y . It can be observed that for bigger W_y , the power reflected from the antenna is higher, while at the same time the Gain gets higher. What is more important though, is that the frequencies of maximum gain and maximum power absorption are shifted, for all cases, with respect to each other: this gives a narrower overall bandwidth. Moreover, they both shift towards lower frequencies for thinner W_y .

It is clear that a tradeoff between a high Gain and a low power reflection is necessary. Let's define B_S as the bandwidth in terms of S_{11} requisites only and B_G as the bandwidth in terms of Gain requisites only:

- B_S : frequency range where $S_{11} < \text{targeted } S_{11}$
- B_G : frequency range where $G > \text{targeted } G$.

Our choice of $W_y = 0.5\text{mm}$ gives a value of $B_G(G > 19\text{db})$ equal to 400MHz, centered in 19.7GHz; a value of $B_S(S < -3\text{db})$ equal to 300MHz, centered in 19.85GHz.

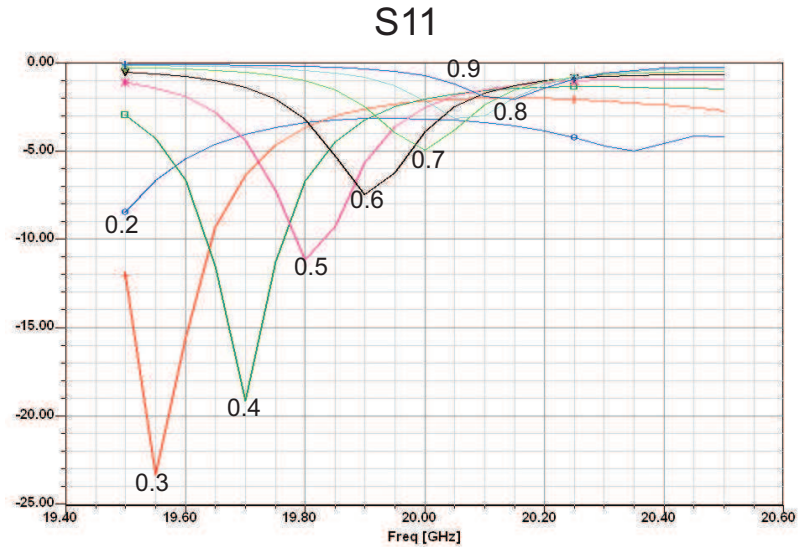


Figure 3.24: S_{11} variation for different strip widths W_y .

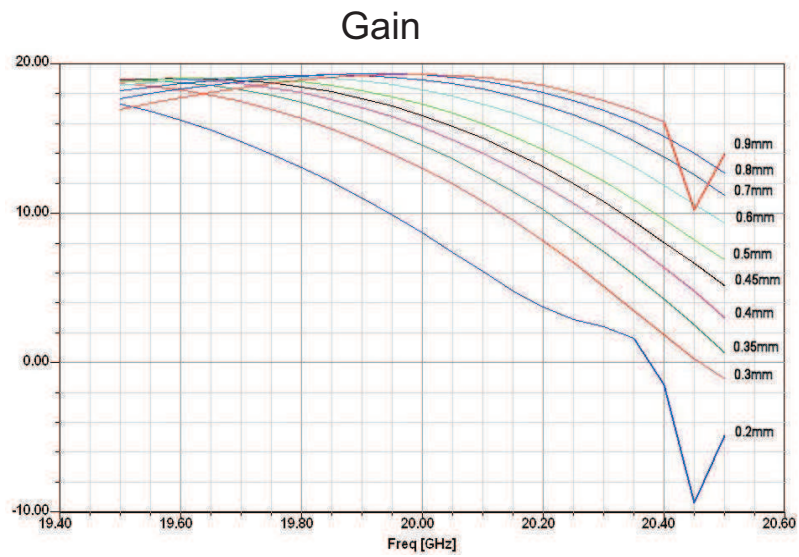


Figure 3.25: Gain variation for different strip widths W_y .

Let's now proceed to the analysis of the variation of W_x , keeping $W_y = 0.5\text{mm}$. It can be observed from figures 3.26 and 3.27 how W_x influences the antenna behavior similarly to W_y , even if less dramatically. That is, for bigger W_x , the power reflected from the antenna is higher but the Gain curve is better. Again, a choice of compromise is necessary, and W_x must be chosen in such a way to have a good impedance matching without sacrificing too much the Gain curve. A value of $W_x = 0.4\text{mm}$ allows to obtain the following performances:

- $S_{11} < -3\text{dB}$ in the range $19.7 - 20\text{GHz}$
- $S_{11} < -5\text{dB}$ in the range $19.75 - 19.95\text{GHz}$
- $G > 18\text{dB}$ in the range $19.35 - 20\text{GHz}$
- $G > 19\text{dB}$ in the range $19.6 - 19.8\text{GHz}$

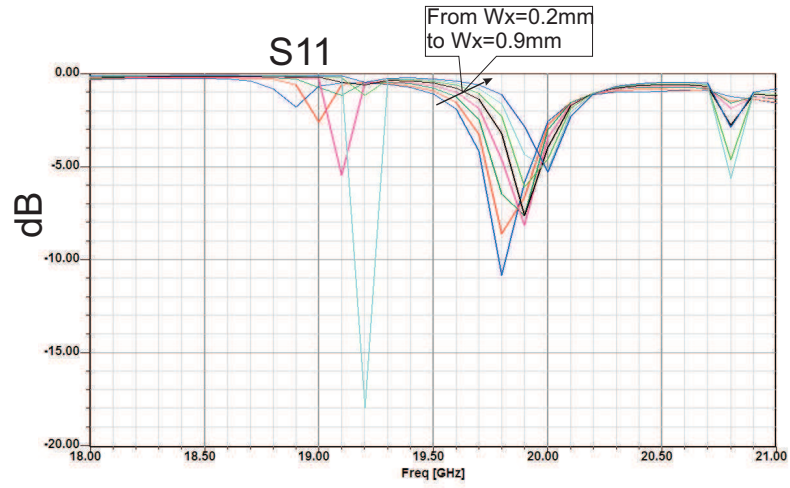


Figure 3.26: S_{11} variation for different strip widths W_x .

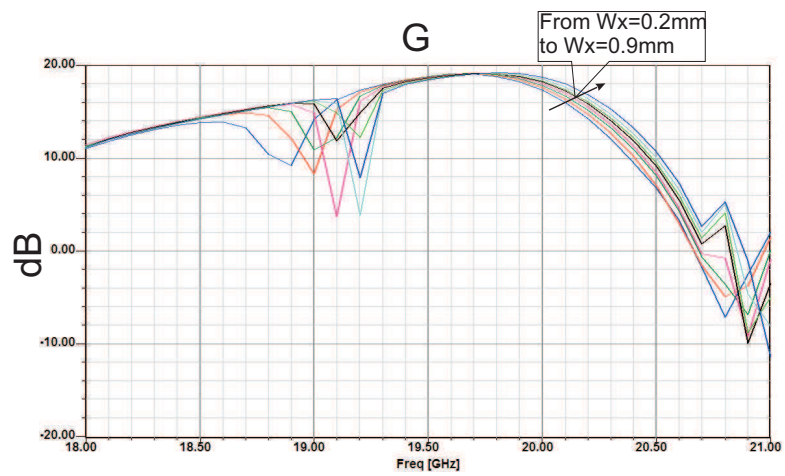


Figure 3.27: Gain variation for different strip widths W_x .

3.7 The introduction of perfectly magnetic walls.

Our conclusions, after the optimizations described in the previous parameters, were not completely satisfactory. The overall bandwidth of the antenna is narrow ($\sim 1.5\%$) and it was obtained in exchange of a lower maximum Gain (19dB against the 20dB that could be reached with different grids). A big part of the problem is that the center frequencies of the bands B_S and B_G are shifted, thus reducing the overall bandwidth.

We tried to find a solution to this problem by reverting to the basic principles of this antenna: the more uniform the illumination of the grating, the better the performances, at least in terms of directivity. For a metallic cavity, the TE₀₁₁ is the first z-resonant mode that can be excited (see Appendix C), with a sinusoidal field distribution along the x axis, and a constant field distribution along the y axis (see Fig.3.17).

Could it be possible to modify the cavity in such a way to obtain a cavity mode which is resonant along the z axis, but with a constant illumination both along the x and along the y axis? The answer to this question must necessarily be searched in a change of boundary conditions in the lateral walls of the cavity. In particular, if the x-aligned walls are made of a perfectly magnetic material, a TEM mode can be present in the cavity and resonate along the z axis (see Appendix C). This would give the best possible aperture illumination and so the best possible surface efficiency.

A first attempt in this sense has been made by simply taking the antenna with the optimized grid described in the last section, and by changing the boundary conditions of the lateral (x-aligned) walls, with the aim of just demonstrate the feasibility of the idea. The result was an immediate improvement of the maximum gain of around 1dB, as Fig. 3.28 shows, with the expected field distribution inside the cavity (Fig. 3.30).

At around 19.7GHz, a resonant peak appears, in correspondence to a sudden degradation of the Gain curve. At a second analysis, it appears to be a 450 mode (Fig.3.29). This mode is far enough from the work frequency and doesn't represent a problem, nevertheless it will be moved at slightly higher frequency by means of a small cavity resize, using the same analytical tool used previously for the metallic cavity.

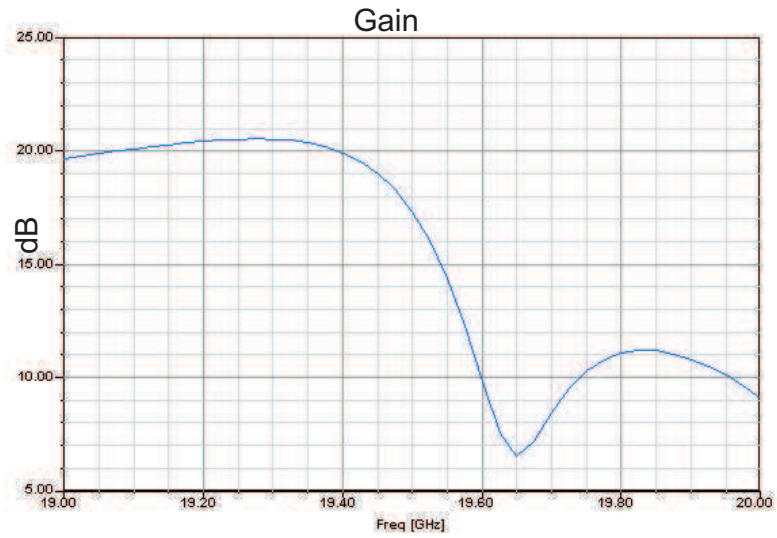


Figure 3.28: Gain curve obtained by using two perfectly magnetic walls.

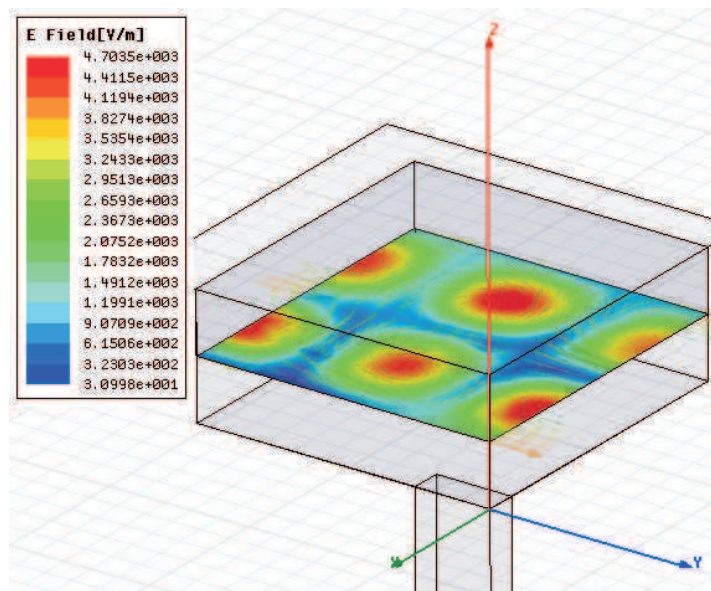


Figure 3.29: TE450 mode appearing when using a PEC/PMC cavity

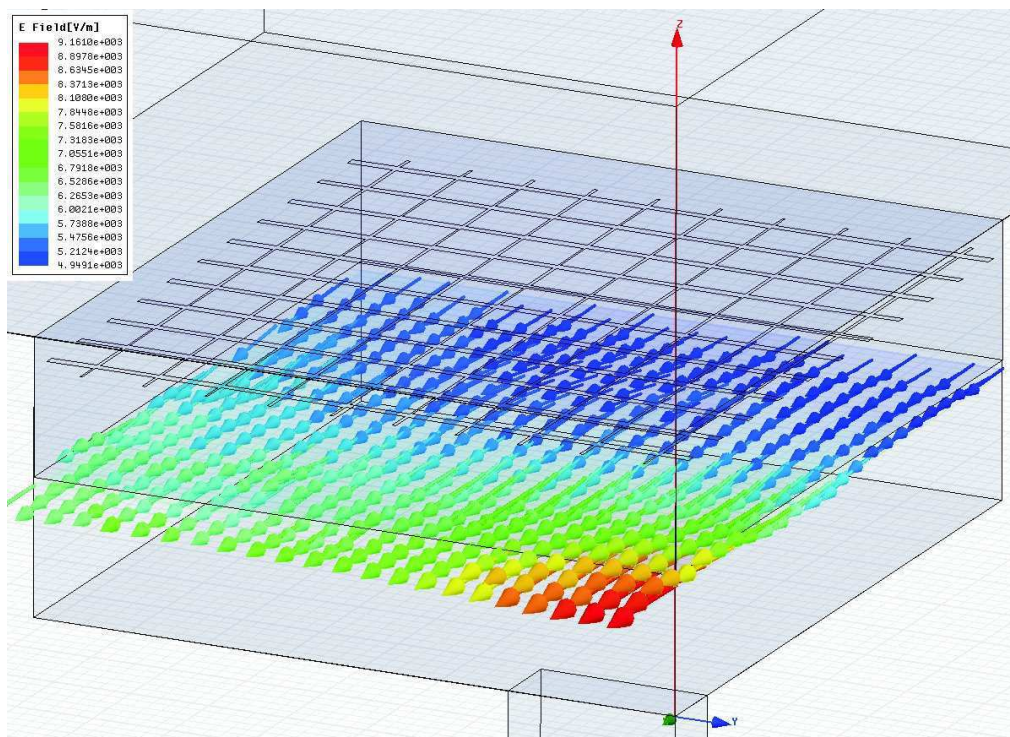


Figure 3.30: Electric field magnitude and polarization, at 19.2 GHz, in a PEC/PMC cavity. It can be noticed how the field amplitude is almost constant in the xy plane.

3.7.1 Grid optimization with metallic walls

The previous result has been obtained with a grid optimized for a fully metallic cavity and a TE011 mode illumination. This grid is surely not optimal in this case, where the cavity mode has a constant distribution both along the x and along the y axis. A new grid optimization thus has been ran, in order to maximize Gain and Impedance matching.

A procedure similar to the one depicted in §3.6 has been adopted. The first step consists in optimizing the width W_y while keeping the value $W_x = 0.3\text{mm}$. The influence of W_y on Gain and Impedance Matching is shown in Fig. 3.32. Larger widths W_y shift the point of minimum power reflection and maximum gains at higher frequencies, as already observed with metallic walls. The usual compromise between Gain and Impedance Matching is again present, though in this case the Gain values are between 1 and 2 dBs higher than in the case of metallic walls.

A value of $W_y = 0.1\text{mm}$ has been chosen as the best $G \sim S_{11}$ tradeoff. The hypothesis of thinner values has not been investigated, because for the technologies used at this scale, it is near to the lowest realizable value.

The second step was the optimization of W_x , keeping $W_y = 0.1\text{mm}$. Again, this parameter has a smaller impact on the Gain and S_{11} curves, but still it must be carefully chosen to obtain a well-tuned antenna. The choice of $W_x = 0.3$ finally seems the best and gives the following performances:

- $S_{11} < -3\text{dB}$ in the range 19.10 – 19.40GHz
- $S_{11} < -5\text{dB}$ in the range 19.15 – 19.35GHz
- In the same range of frequencies, G is equal or higher than 20dB, except between 19.35 and 19.40 GHz, where anyway it remains higher than 19 dB.

We remember that this has been obtained with a cavity size of $(x = 43.56, y = 41, z = 7.53)\text{mm}$. The surface efficiency can easily be calculated from the value of 20dB of directivity, at 19.25GHz, as

$$\epsilon_{ap} = \frac{100}{43.56 \cdot 41 \frac{4\pi}{15.6^2}} \sim 1 \quad (3.16)$$

The total bandwidth of the antenna is 1.56%, centered on 19.25GHz, whit a Gain of 20dB on most of it.

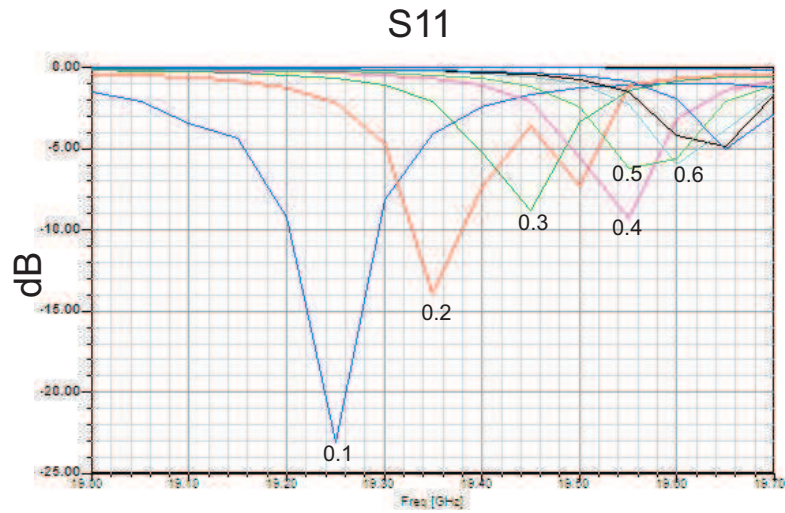


Figure 3.31: S_{11} variation for different strip widths W_y , keeping $W_x = 0.3\text{mm}$.

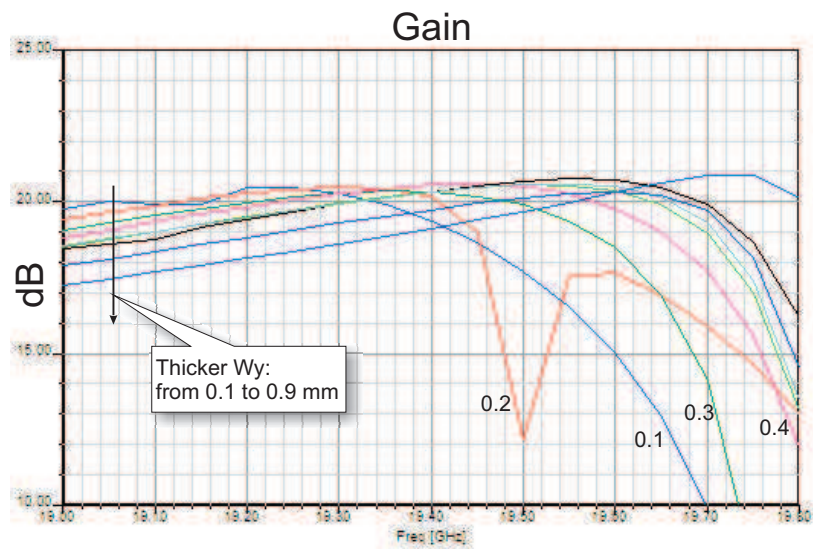


Figure 3.32: Gain variation for different strip widths W_y , keeping $W_x = 0.3\text{mm}$.

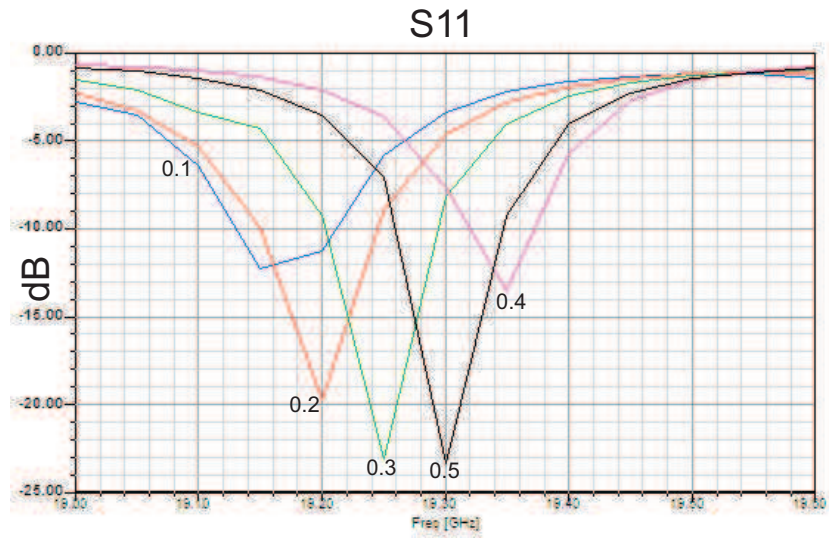


Figure 3.33: S_{11} variation for different strip widths W_x , keeping $W_y = 0.1\text{mm}$.

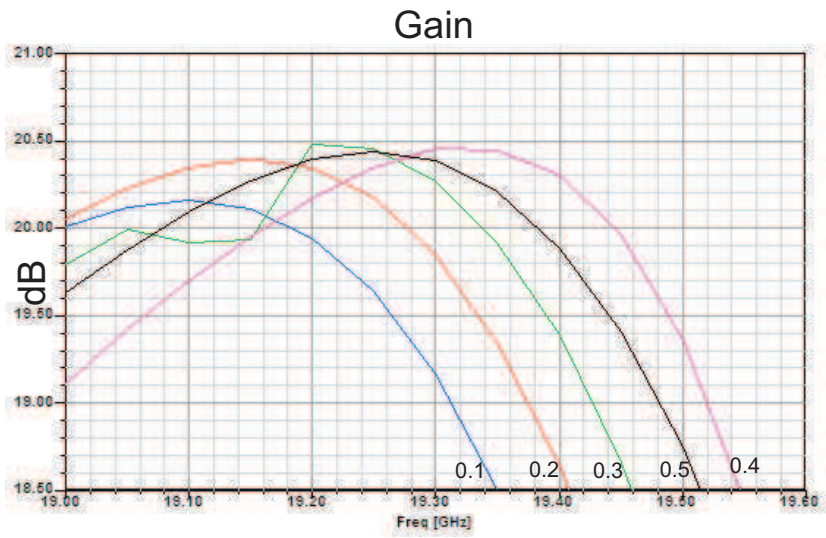


Figure 3.34: Gain variation for different strip widths W_x , keeping $W_y = 0.1\text{mm}$.

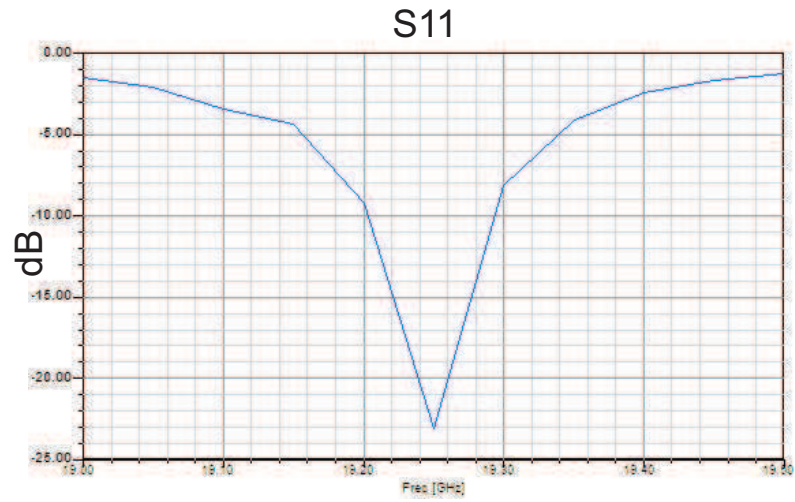


Figure 3.35: Detail on S_{11} for the grid optimized in presence of the magnetic walls.

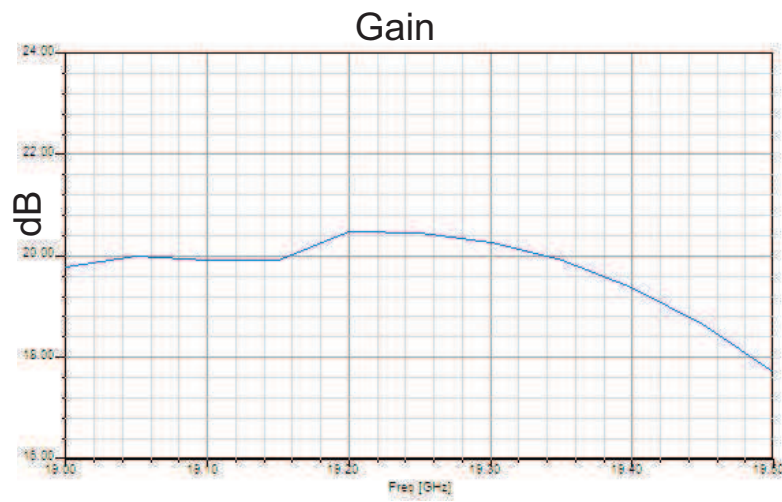


Figure 3.36: Detail on G for the grid optimized in presence of the magnetic walls.

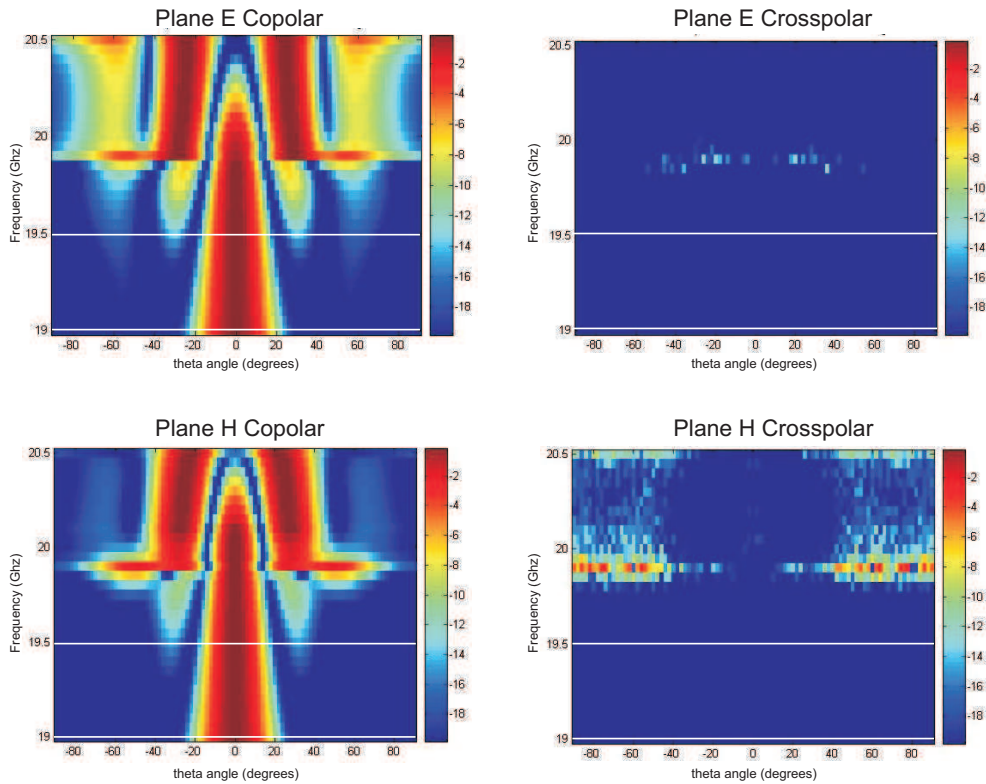


Figure 3.37: Radiation pattern of the PEC/PMC cavity with optimized grid. The white lines identify the frequency range of utilization.

3.8 Conclusions

In the course of this report, we have addressed the problem of designing a compact planar antenna for satellite applications. The main goals of the designs were surface efficiency, high power handling, compact size. The initial designs, inspired by a Photonic Band Gap antenna, have been modified to meet our needs and led to a cavity-backed, metallic grid antenna. With the help of accurate Finite Elements simulations and measures of prototypes, we have gained a good insight of the physical behavior of the antenna. This allowed us to develop an analytical tool that can support the design of the cavity size for different frequencies. Finally, by exploiting the properties of artificial surfaces, we have designed the final PEC/PMC configuration, which has allowed us to meet most of the requested specifics.

The main advantages of this antenna is the compact size in terms of thickness. For a comparable aperture size when compared to a typical pyramidal

horn, this antenna is on order of magnitude thinner ($\lambda/2$ against the 6λ of a typical corrugated horn. This gives a wider flexibility for reciprocal antenna placement when designing arrays and allows conformal surface mounting. Moreover, it grants a major weight decrease, which is a crucial factor for satellite antennas.

Several perspective works arise from this project. At first, the design and realization of an artificial surface which can behave as a PMC in the frequency range of interest will be needed. Several papers and practical realizations are available from other authors and it will be interesting to see how these surfaces will behave when embedded in our design.

A second effort should be done to be able to support circular polarizations. Some experiments have been done in this sense during these project, and have been abandoned mostly for problems in the realization of prototypes. Basing on our observations, we have strong clues that very good performances can be achieved by using a square cavity in conjunction with feeding system made of two in-phase waveguides. This structure is in our opinion the best candidate to form the basis of a circularly polarized antenna.

Last but not least, the major inconvenient of this antenna is the bandwidth, which is the parameter that satisfies the worst the requested value. The resonant nature of the cavity in fact is an intrinsic limit. This limit could be overtaken, in our opinion, only in exchange of a lower maximum directivity, as the measures and simulations we showed demonstrate.

Finally, an impedance matching device must be designed. This has never been a goal of our project, which has instead been assigned to an independent team. The effects of such a device on the bandwidth of this antenna should be investigated.

References

- [1] V.D. Kupradze. On the approximate solutions of problems in mathematical physics. *Russ. Math. Surveys*, 22:58–108, 1967.
- [2] C. Hafner. *The generalized multipole technique for computational electromagnetics*. Artech house books, Boston, 1990.
- [3] A. Boag Y. Leviatan. Analysis of electromagnetics scattering from dielectric cylinders using a multifilament current method. *IEEE Trans. Ant. Prop.*, 35:1119–1127, 1987.
- [4] G. Tayeb. *Contribution à l'étude de la diffraction des ondes électromagnétiques par des reseaux. Reflexions sur les methodes existantes et sur leur extension aux milieux anisotropes*. PhD thesis, Université Paul Cézanne Aix-Marseille III, 1990.
- [5] G.Tayeb. The method of fictitious sources applied to diffraction gratings. *Appl. Comput. Electromagnetics Soc. J.*, 9:90–100, 1994.
- [6] G. Tayeb, R. Petit, and M. Cadilhac. The synthesis method applied to the problem of diffraction by gratings: the method of fictitious sources. In *Internat. Conf. Appl. Theory Periodic Structures SPIE*, volume 1545, pages 95–105.
- [7] F. Zolla, R. Petit, and M. Cadilhac. Electromagnetic theory of diffraction by a system of parallel rods: the method of fictitious sources. *J. Opt. Soc. Am. A*, 11:1087–1096, 1994.
- [8] F. Zolla and R. Petit. Method of fictitious sources as applied to the electromagnetic diffraction of a plane wave by a grating in conical diffraction mounts. *J. Opt. Soc. Am. A*, 13:796–802, 1996.
- [9] Cadilhac, M. and Petit,R. *Huyghens Principle 16901990, Theory and Applications*, chapter On the diffraction problem in electromagnetic theory: A discussion based on concepts of functional analysis including an

- example of practical application., page 249272. Elsevier, Amsterdam, 1992.
- [10] M. Paulus, P. Gay-Balmaz, and O.J.F. Martin. Accurate and efficient computation of the green's tensor for stratified media. *Physical Review E*, 62(4):5797–5807, October 2000.
 - [11] A. Sommerfeld. *Ann.Phys. (Leipzig)*, 28:665, 1909.
 - [12] J.R. Mosig and F.E. Gardiol. *IEE Proc. Pt.H: Microwaves. Opt. Antennas*, 130:175, 1983.
 - [13] A.Banos. *Dipole Radiation in the Presence of a Conducting Half-Space*. Pergamon Press, Oxford, 1966.
 - [14] J.R. Wait. *Electromagnetic Waves in Stratified Media*. IEEE Press, New York, 1996.
 - [15] J.R. Mosig and P.Gay-Balmaz. *Int. J. Microwave and Millimeter wave CAE*, 3:330, 1997.
 - [16] P.M. Morse and H. Feshbach. *Methods of Theoretical Physics*. McGraw-Hill, New York, 1953.
 - [17] J. A. Kong. *Electromagnetic Wave Theory*. Wiley, New York, 1986.
 - [18] P. Davis and P. Rabinowitz. *Methods of Numerical Integration*. Academic Press, Inc., Orlando, FL, 1984.
 - [19] L.B. Felsen and N. Marcuvitz. *Radiation and Scattering of Waves*. IEEE Press, New York, 1994.
 - [20] W.C. Chew. *Waves and Fields in Inhomogeneous Media*. IEEE Press, New York, 1995.
 - [21] H.T. Anastassiou, D.G. Lymperopoulos, and D.I. Kaklamani. Accuracy analysis and optimization of the method of auxiliary sources (MAS) applied to TE scattering by a perfectly conducting circular cylinder. In *ICECom 2003 17th International Conference on Applied Electromagnetics and Communication*, pages 411–414, 1-3 October 2003.
 - [22] Hyung-Gi Na and Hyo-Tae Kim. Convergence of the fictitious-current model. *IEEE Proc.-Microw. Antennas Propag.*, 143(2):163–168, April 1996.

- [23] P.L.E. Uslenghi J.J. Bowman, T.B.A. Senior. *Electromagnetic and acoustic scattering by simple shapes*. North-Holland Publishing Company, 1969.
- [24] Dimitra I. Kaklamani and Hristos T. Anastassiou. Aspects of the method of auxiliary sources (MAS) in computational electromagnetics. *IEEE Ant. Prop. Mag.*, 44(3):48–64, June 2002.
- [25] N. Guérin, S. Enoch, G. Tayeb, P. Sabouroux, P. Vincent, and H. Legay. A metallic fabry-perot directive antenna. *IEEE Trans. Ant. Prop.*, 54(1):220–224, 2006.
- [26] D. Felbacq, G. Tayeb, and D. Maystre. Scattering by a random set of parallel cylinders. *J. Opt. Soc. Am. A*, 1:2526–2538, 1994.
- [27] Constantin A. Balanis. *Antenna Theory, Analysis and Design*. John Wiley and Sons, Inc., 1997.

Appendix A

Green's function magnetic field.

The magnetic field can be obtained from the electric field, for each single Fourier component, via the Maxwell equation

$$\mathbf{H} = \frac{j}{\omega\mu} \nabla \times \mathbf{E} \quad (\text{A.1})$$

In our case, we start from the G tensor, whose components we have called $G_{\alpha\beta}$. We can now introduce the vector \mathbf{G}_β , which represent the electric field radiated by a dipole oriented in the direction β , where β is one of the cartesian unitary vector. In the same way, we introduce the vector $\mathbf{G}_{H\beta}$ for the magnetic field. Following equation A.1, we can write

$$\begin{aligned} \nabla \times \mathbf{G}_\beta = & \left(\frac{\partial}{\partial y} G_{z\beta} - \frac{\partial}{\partial z} G_{y\beta} \right) \hat{x} + \\ & \left(\frac{\partial}{\partial z} G_{x\beta} - \frac{\partial}{\partial x} G_{z\beta} \right) \hat{y} + \\ & \left(\frac{\partial}{\partial x} G_{y\beta} - \frac{\partial}{\partial y} G_{x\beta} \right) \hat{z} \end{aligned} \quad (\text{A.2})$$

The computation will be performed on equation (2.13), and in a second time the passage in cylindrical coordinate will be performed. The k_x, k_y integration and the rotational are performed on independent variables, so the order of the operands will be swapped.

A.1 s- polarization

The generic form of the s- polarized component of \mathbf{G} is

$$\begin{aligned}
G_{\alpha\beta}^s(\mathbf{r}, \mathbf{r}') &= \frac{i}{8\pi^2} \int \int dk_x dk_y \exp\{i[k_x(x-x') \\
&+ k_y(y-y')]\} \frac{1}{k_{lz}} \{[\hat{l}_\alpha(\pm k_{lz}) A_{l,\alpha\beta}^s \exp(ik_{lz}z) \\
&+ \hat{l}_\alpha(\mp k_{lz}) B_{l,\alpha\beta}^s \exp(-ik_{lz}z)] \hat{l}_\beta(k_{lz})\}
\end{aligned} \tag{A.3}$$

where

$$\begin{aligned}
\hat{l} &= (\sin k_\phi, -\cos k_\phi, 0) \\
\hat{m} &= \left(\frac{k_{lz}}{k_l} \cos k_\phi, \frac{k_{lz}}{k_l} \sin k_\phi, \frac{k_\rho}{k_l} \right)
\end{aligned} \tag{A.4}$$

A small simplification can be introduced by noticing that $\hat{l}(+k_{lz}) = \hat{l}(-k_{lz})$. Moreover, being $\hat{l}_z = 0$, we can conclude that

$$\begin{aligned}
G_{h,x\beta}^s &= -\frac{\partial}{\partial z} G_{y\beta}^s \\
G_{h,y\beta}^s &= \frac{\partial}{\partial z} G_{x\beta}^s \\
G_{h,z\beta}^s &= \frac{\partial}{\partial x} G_{y\beta}^s - \frac{\partial}{\partial y} G_{x\beta}^s
\end{aligned} \tag{A.5}$$

We provide the details of the calculations for the first component only of the (A.5); the calculation for the other components is absolutely similar.

$$G_{h,x\beta}^s = \frac{-i}{8\pi^2} \int \int dk_x dk_y \frac{1}{k_{lz}} [\hat{l}_y \hat{l}_\beta \frac{\partial}{\partial z} (A^s e^{ik_{lz}z} + B^s e^{-ik_{lz}z})] e^{i[k_x(x-x') + k_y(y-y')]} \tag{A.6}$$

where

$$\begin{aligned}
A^s(z, z') &= A_0^s(z') + \Theta(z - z') e^{-ik_{l'z}z'} \Rightarrow \frac{\partial}{\partial z} A^s = \delta(z - z') e^{-ik_{l'z}z'} \\
B^s(z, z') &= B_0^s(z') + \Theta(z' - z) e^{ik_{l'z}z'} \Rightarrow \frac{\partial}{\partial z} B^s = -\delta(z - z') e^{ik_{l'z}z'}.
\end{aligned} \tag{A.7}$$

which leads us to the expression

$$\begin{aligned}
G_{h,x\beta}^s &= \left(\dots \right) \frac{1}{k_{lz}} \left[\hat{l}_y \hat{l}_\beta \left(\delta(z - z') e^{i(k_{lz}z - k_{l'z}z')} - \delta(z - z') e^{-i(k_{lz}z - k_{l'z}z')} \right. \right. \\
&\quad \left. \left. + ik_{lz} A^s e^{ik_{lz}z} - ik_{lz} B^s e^{-ik_{lz}z} \right) \right].
\end{aligned} \tag{A.8}$$

In $z = z'$, it is also true that $k_{lz} = k_{l'z}$, so the two Dirac-delta terms cancel each other, thus giving the expression

$$G_{h,x\beta}^s = \left(\dots \right) \frac{1}{k_{lz}} \left[\hat{l}_y \hat{l}_\beta \left(ik_{lz} A^s e^{ik_{lz}z} - ik_{lz} B^s e^{-ik_{lz}z} \right) \right]. \quad (\text{A.9})$$

By passing in cylindrical coordinates, and using 2.14 to perform the integration along k_ϕ , we obtain, in analogy to the 2.15, the integrand terms

$$f_{h,xx}^s = -i \left[-k_\rho J_0(k_\rho \rho) + \frac{2}{\rho} J_1(k_\rho \rho) \right] \sin(\phi) \cos(\phi) \quad (\text{A.10})$$

$$\cdot \left[A^s \exp^{ik_{lz}z} - B^s \exp^{-ik_{lz}z} \right]$$

$$f_{h,xy}^s = -i \left[k_\rho J_0(k_\rho \rho) \cos^2 \phi - \frac{1}{\rho} J_1(k_\rho \rho) \cos(2\phi) \right] \quad (\text{A.11})$$

$$\cdot \left[A^s \exp^{ik_{lz}z} - B^s \exp^{-ik_{lz}z} \right].$$

With similar calculations, the other components can be computed, obtaining

$$f_{h,xz}^s = 0 \quad (\text{A.12})$$

$$f_{h,yx}^s = i \left[k_\rho J_0(k_\rho \rho) \sin^2 \phi + \frac{1}{\rho} J_1(k_\rho \rho) \cos(2\phi) \right] \quad (\text{A.13})$$

$$\cdot \left[A^s e^{ik_{lz}z} - B^s e^{-ik_{lz}z} \right]$$

$$f_{h,yy}^s = f_{h,xx}^s \quad (\text{A.14})$$

$$f_{h,yz}^s = 0 \quad (\text{A.15})$$

$$f_{h,zx}^s = \frac{k_\rho^2}{k_{lz}} J_1(k_\rho \rho) \sin \phi \left[A^s e^{ik_{lz}z} + B^s e^{-ik_{lz}z} \right] \quad (\text{A.16})$$

$$f_{h,zy}^s = -\frac{k_\rho^2}{k_{lz}} J_1(k_\rho \rho) \cos \phi \left[A^s e^{ik_{lz}z} + B^s e^{-ik_{lz}z} \right] \quad (\text{A.17})$$

$$f_{h,zz}^s = 0 \quad (\text{A.18})$$

$$(\text{A.19})$$

A.2 p- polarization

The generic form of the p- polarized component of \mathbf{G} is

$$\begin{aligned}
G_{\alpha\beta}^p(\mathbf{r}, \mathbf{r}') &= \frac{i}{8\pi^2} \int \int dk_x dk_y \exp\{i[k_x(x-x') \\
&\quad + k_y(y-y')]\} \frac{1}{k_{lz}} \{[\hat{m}_\alpha(\pm k_{lz}) A_{l,\alpha\beta}^p \exp(ik_{lz}z) \\
&\quad + \hat{m}_\alpha(\mp k_{lz}) B_{l,\alpha\beta}^p \exp(-ik_{lz}z)] \hat{m}_\beta(k_{lz})\}
\end{aligned} \tag{A.20}$$

The components of $\mathbf{G}_{H\beta}$ are given by

$$G_{h,x\beta}^p = \frac{\partial}{\partial y} G_{z\beta}^p - \frac{\partial}{\partial z} G_{y\beta}^p \tag{A.21}$$

$$G_{h,y\beta}^p = \frac{\partial}{\partial z} G_{x\beta}^p - \frac{\partial}{\partial x} G_{z\beta}^p \tag{A.22}$$

$$G_{h,z\beta}^p = \frac{\partial}{\partial x} G_{y\beta}^p - \frac{\partial}{\partial y} G_{x\beta}^p \tag{A.23}$$

but we will provide here the details of the calculation only for $G_{h,xx}^p$. In general, it is

$$\begin{aligned}
\frac{\partial}{\partial y} G_{z\beta}^p &= ik_y G_{z\beta}^p = \\
\frac{1}{8\pi^2} \int \int dk_x dk_y \frac{ik_y}{k_{lz}} &\left\{ \hat{m}_z \cdot \hat{m}_\beta \left(A_{z\beta}^p e^{ik_{lz}z} + B_{z\beta}^p e^{-ik_{lz}z} \right) \right\} e^{i[k_x(x-x') + k_y(y-y')]}
\end{aligned} \tag{A.24}$$

that, in the case $\beta = x$ and passing in cylindrical coordinates, becomes

$$-i \frac{k_\rho^3}{k_l^2} \sin(k_\phi) \cos(k_\phi) \left(A_{z,x}^p e^{ik_{lz}z} + B_{z,x}^p e^{-ik_{lz}z} \right) e^{ik_\rho \rho \cos(k_\phi - \phi)} \tag{A.25}$$

which, by using Bessel identity, gives us the first part of the monodimensional integrand in (A.21), that I call

$$f_{h,xx}^{p(1)} = i \frac{k_\rho^2}{k_l^2} \left[-k_\rho J_0(k_\rho \rho) + \frac{2}{\rho} J_1(k_\rho \rho) \right] \sin(\phi) \cos(\phi) \left(A_{zx}^p e^{ik_{lz}z} + B_{zx}^p e^{-ik_{lz}z} \right). \tag{A.26}$$

The second part of equation (A.21) is

$$\begin{aligned} \frac{\partial}{\partial z} G_{y\beta}^p = & \\ & \frac{1}{8\pi^2} \int \int dk_x dk_y \frac{1}{k_{lz}} \left\{ \pm \hat{m}_y \hat{m}_\beta \left[\left(\frac{\partial}{\partial z} A_{y\beta}^p \right) e^{ik_{lz}z} + ik_{lz} A_{y\beta}^p e^{ik_{lz}z} \right. \right. \\ & \left. \left. - \left(\frac{\partial}{\partial z} B_{y\beta}^p \right) e^{-ik_{lz}z} + ik_{lz} B_{y\beta}^p e^{-ik_{lz}z} \right] \hat{m}_\beta \right\} e^{i[k_x(x-x') + k_y(y-y')]} \end{aligned} \quad (\text{A.27})$$

where

$$A_{y\beta}^p(z, z') = \begin{cases} \pm A_{y\beta 0}^p(z') \pm \Theta(z - z') e^{-ik_{l'z}z'} & \text{if } \beta \neq z \\ A_{y\beta 1}^p(z') + \Theta(z - z') e^{-ik_{l'z}z'} & \text{if } \beta = z \end{cases} \quad (\text{A.28})$$

$$B_{y\beta}^p(z, z') = \begin{cases} \mp B_{y\beta 0}^p(z') \mp \Theta(z' - z) e^{ik_{l'z}z'} & \text{if } \beta \neq z \\ B_{y\beta 1}^p(z') + \Theta(z' - z) e^{ik_{l'z}z'} & \text{if } \beta = z \end{cases} \quad (\text{A.29})$$

By calculating the z derivative of these expressions, we get

$$\frac{\partial}{\partial z} A_{y\beta}^p(z, z') = \begin{cases} \delta(z - z') (2A_{y\beta 0}^p + e^{-ik_{l'z}z'}) & \text{if } \beta \neq z \\ \delta(z - z') e^{-ik_{l'z}z'} & \text{if } \beta = z \end{cases} \quad (\text{A.30})$$

$$\frac{\partial}{\partial z} B_{y\beta}^p(z, z') = \begin{cases} -\delta(z - z') (2B_{y\beta 0}^p + e^{ik_{l'z}z'}) & \text{if } \beta \neq z \\ -\delta(z - z') e^{ik_{l'z}z'} & \text{if } \beta = z. \end{cases} \quad (\text{A.31})$$

By substituting into equation (A.27), in the case $\beta = z$ we obtain

$$\begin{aligned} \frac{\partial}{\partial z} G_{y\beta}^p = & \\ = & \frac{1}{8\pi^2} \int \int dk_x dk_y \frac{1}{k_{lz}} \left\{ \pm \frac{k_{lz}^2}{k_l} \cos(k_\phi) \sin(k_\phi) \left[ik_{lz} \left(A_{yx}^p e^{ik_{lz}z} + B_{yx}^p e^{-ik_{lz}z} \right) \right. \right. \\ & \left. \left. + \delta(z - z') \left(2A_{yx0}^p + e^{-ik_{l'z}z'} \right) e^{ik_{lz}z} + \delta(z - z') \left(2B_{yx0}^p + e^{ik_{l'z}z'} \right) e^{-ik_{lz}z} \right] \right\} \\ & \cdot e^{i[k_x(x-x') + k_y(y-y')]} \end{aligned} \quad (\text{A.32})$$

that, passing in cylindrical coordinate and using Bessel identity, gives us the second part of the monodimensional integrand,

$$\begin{aligned} f_{h,xx}^{p(2)} = & \mp i \left(\frac{k_{lz}}{k_l} \right)^2 \left[k_\rho J_0(k_\rho \rho) - \frac{2}{\rho} J_1(k_\rho \rho) \right] \sin(\phi) \cos(\phi) \left(A_{yx}^p e^{ik_{lz}z} + B_{yx}^p e^{-ik_{lz}z} \right) \\ & - \delta(z - z') \left\{ 2 \frac{k_{lz}}{k_l^2} \left[k_\rho J_0(k_\rho \rho) - \frac{2}{\rho} J_1(k_\rho \rho) \right] \sin(\phi) \cos(\phi) \left(A_{yx0}^p e^{ik_{lz}z} + B_{yx0}^p e^{-ik_{lz}z} + 1 \right) \right\}. \end{aligned} \quad (\text{A.33})$$

To sum up, we provide here the complete expressions for $f_{h,\alpha\beta}^p$:

$$f_{h,xx}^p = i \frac{k_\rho^2}{k_l^2} \left[-k_\rho J_0(k_\rho \rho) + \frac{2}{\rho} J_1(k_\rho \rho) \right] \sin(\phi) \cos(\phi) \left(A_{zx}^p e^{ik_{lz}z} + B_{zx}^p e^{-ik_{lz}z} \right) \quad (\text{A.34})$$

$$\begin{aligned} & \mp i \left(\frac{k_{lz}}{k_l} \right)^2 \left[k_\rho J_0(k_\rho \rho) - \frac{2}{\rho} J_1(k_\rho \rho) \right] \sin(\phi) \cos(\phi) \left(A_{yx}^p e^{ik_{lz}z} + B_{yx}^p e^{-ik_{lz}z} \right) \\ & - \delta(z-z') \left\{ 2 \frac{k_{lz}}{k_l^2} \left[k_\rho J_0(k_\rho \rho) - \frac{2}{\rho} J_1(k_\rho \rho) \right] \sin(\phi) \cos(\phi) \left(A_{yx0}^p e^{ik_{lz}z} + B_{yx0}^p e^{-ik_{lz}z} + 1 \right) \right\} \\ f_{h,xy}^p &= -i \frac{k_\rho^2}{k_l^2} \left[k_\rho J_0(k_\rho \rho) \sin^2(\phi) + \frac{1}{\rho} J_1(k_\rho \rho) \cos(2\phi) \right] \left(A_{zy}^p e^{ik_{lz}z} + B_{zy}^p e^{-ik_{lz}z} \right) \quad (\text{A.35}) \\ & \mp i \left(\frac{k_{lz}}{k_l} \right)^2 \left[k_\rho J_0(k_\rho \rho) \sin^2(\phi) + \frac{1}{\rho} J_1(k_\rho \rho) \cos(2\phi) \right] \left(A_{yy}^p e^{ik_{lz}z} + B_{yy}^p e^{-ik_{lz}z} \right) \\ & - \delta(z-z') \left\{ 2 \frac{k_{lz}}{k_l^2} \left[k_\rho J_0(k_\rho \rho) \sin^2(\phi) + \frac{1}{\rho} J_1(k_\rho \rho) \cos(2\phi) \right] \left(A_{yy0}^p e^{ik_{lz}z} + B_{yy0}^p e^{-ik_{lz}z} + 1 \right) \right\} \end{aligned}$$

$$\begin{aligned} f_{h,xz}^p &= -\frac{k_\rho}{k_{lz} k_l^2} \sin(\phi) J_1(k_\rho \rho) \left(A_{zz}^p e^{ik_{lz}z} + B_{zz}^p e^{-ik_{lz}z} \right) \quad (\text{A.36}) \\ & \mp \frac{k_\rho^2 k_{lz}}{k_l^2} \sin(\phi) J_1(k_\rho \rho) \left(A_{yz}^p e^{ik_{lz}z} + B_{yz}^p e^{-ik_{lz}z} \right) \end{aligned}$$

$$\begin{aligned} f_{h,yx}^p &= \pm i \left(\frac{k_{lz}}{k_l} \right)^2 \left[k_\rho J_0(k_\rho \rho) \cos^2(\phi) - \frac{1}{\rho} J_1(k_\rho \rho) \cos(2\phi) \right] \left(A_{xx}^p e^{ik_{lz}z} + B_{xx}^p e^{-ik_{lz}z} \right) \quad (\text{A.37}) \\ & + 2i\delta(z-z') \left\{ \left(\frac{k_{lz}}{k_l^2} \right) \left[k_\rho J_0(k_\rho \rho) \cos^2(\phi) - \frac{1}{\rho} J_1(k_\rho \rho) \cos(2\phi) \right] \left(A_{xx0}^p e^{ik_{lz}z} + B_{xx0}^p e^{-ik_{lz}z} \right) \right\} \\ & + i \frac{k_\rho^2}{k_l^2} \left[k_\rho J_0(k_\rho \rho) \cos^2(\phi) - \frac{1}{\rho} J_1(k_\rho \rho) \cos(2\phi) \right] \left(A_{zx}^p e^{ik_{lz}z} + B_{zx}^p e^{-ik_{lz}z} + 1 \right) \end{aligned}$$

$$\begin{aligned} f_{h,yy}^p &= \mp i \left(\frac{k_{lz}}{k_l} \right)^2 \left[-k_\rho J_0(k_\rho \rho) + \frac{2}{\rho} J_1(k_\rho \rho) \right] \sin(\phi) \cos(\phi) \left(A_{xy}^p e^{ik_{lz}z} + B_{xy}^p e^{-ik_{lz}z} \right) \quad (\text{A.38}) \\ & \mp 2i\delta(z-z') \left\{ \left(\frac{k_{lz}}{k_l^2} \right) \left[-k_\rho J_0(k_\rho \rho) + \frac{2}{\rho} J_1(k_\rho \rho) \right] \sin(\phi) \cos(\phi) \left(A_{xy0}^p e^{ik_{lz}z} + B_{xy0}^p e^{-ik_{lz}z} + 1 \right) \right\} \\ & - i \frac{k_\rho^2}{k_l^2} \left[-k_\rho J_0(k_\rho \rho) + \frac{2}{\rho} J_1(k_\rho \rho) \right] \sin(\phi) \cos(\phi) \left(A_{xy}^p e^{ik_{lz}z} + B_{xy}^p e^{-ik_{lz}z} + 1 \right) \end{aligned}$$

$$\begin{aligned} f_{h,yz}^p &= \pm \frac{k_\rho^2 k_{lz}}{k_l^2} J_1(k_\rho \rho) \cos(\phi) \left(A_{xz}^p e^{ik_{lz}z} + B_{xz}^p e^{-ik_{lz}z} \right) \quad (\text{A.39}) \\ & + \frac{k_\rho^4}{k_l^2 k_{lz}} J_1(k_\rho \rho) \cos(\phi) \left(A_{zz}^p e^{ik_{lz}z} + B_{zz}^p e^{-ik_{lz}z} \right) \end{aligned}$$

$$f_{h,zx}^p = 0 \quad (\text{A.40})$$

$$f_{h,zy}^p = 0 \quad (\text{A.41})$$

$$f_{h,zz}^p = 0. \quad (\text{A.42})$$

Appendix B

MFS and geometry representation

A fully 3D MFS has been implemented in Fortran 90. In its last version, the code can solve scattering problems both in the free space and in stratified media, involving one or multiple homogeneous, non-overlapping scatterers of arbitrary shape.

The program is conceived as a console application, that takes its input from several files (see figure B.1), in ASCII format for easy editing (except for the geometry files), and restitutes the solved electric and magnetic fields, in the region of interest, in ASCII format, for a subsequent visualization with a tool of choice. The linear system's solution (coefficients for the f.s.) is saved for any subsequent field calculations. Besides the solved total field, the residual norm (2.7) is provided as an index of accuracy.

B.1 Geometry representation and the STL format

It can be noticed from Fig.B.1 that the geometrical representation of the scatterer(s) is completely separated from the core of the software, and instead is committed to specialized input files, in STL format. The choice of using an external CAD to generate both the scatterer's surface and the fictitious surfaces is an important aspect of our code, and the main reason for its capability of solving arbitrary shaped objects.

The problem of how to efficiently represent and manipulate geometrical descriptions of the scatterers is one of the first issues arising when trying to implement a 3D numerical method. The problem may be more or less difficult depending on the type of objects one would want to represent. I.e.:

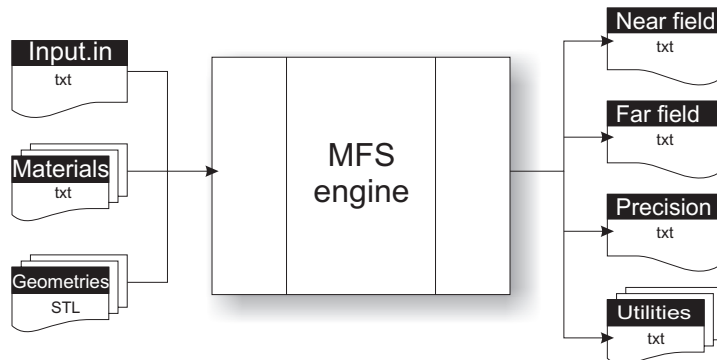


Figure B.1: A gross scheme of the MFS program structure. Each label represents one or more input/output file, with their format.

are we willing to solve only "academic" problems, where objects have a proper analytical description or do we need "real life" objects of arbitrary shapes? Generally speaking, one would always be able to solve the more general case, but without a proper equation to implement, how can we generate the representation of an arbitrary shaped object?

In the f.s. method, it also must be considered that we need not only a representation of the scatterer, but we also need adequate surfaces where f.s. can be placed. Ideally we would also like to be able to manipulate these surfaces arbitrarily, in such a way to investigate the effect of sources placement on solution's accuracy. This makes necessary to properly implement algorithms to move, scale, rotate 3D objects (at least). As most fictitious sources distribution require to be at constant distance from the scatterer surface, proper algorithm of conformal surface creation should be implemented.

Shortly, what we need is a three-dimensional CAD program. There is no point in trying to create a new CAD program from scratch: it is not in the goals of our research and it would be a waste of time. The best solution is to keep the creation and manipulation of three-dimensional geometries *external* to the MFS engine. We only need to choose a data representation that can be used to interface the CAD program to MFS. One choice maybe to interface directly the CAD code (if available) with MFS: this choice, possible in theory, is quite difficult to realize practically for several reasons. Moreover, in this way we would link our code to a given version of the CAD program we use and we would get stuck to the only platform the CAD can run into.

This is why we concluded that the best choice is to completely separate the mesh creation process from the MFS engine. In this way, one could create the meshes on one machine, export them in a suitable format and use them

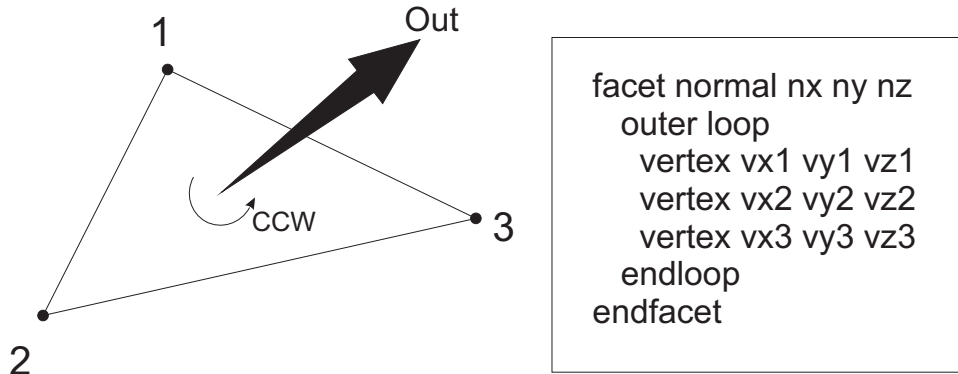


Figure B.2: STL file format and facet orientation. Each triangle is described with its three vertex $\mathbf{v1}$, $\mathbf{v2}$, $\mathbf{v3}$ and the normal vector \mathbf{n}

on one or more machines where MFS is run. In our case we do not need 3D *volume* meshes, but only 3D *surface* meshes. This is because we only enforce boundary conditions on the scatterer surface, and we finally express the total field everywhere in a semi-analytical way.

The STL format is a simple yet complete file format, perfectly suited to represent surface meshes. It is a well documented, open format that contains all the data we need, that is surface point and normal vectors. It is widely used in stereolithography and thus it is available as exportable format from almost every CAD program. An example of Open Source CAD that is able to export in STL format is BRL-CAD or Active3D.

We believe that this solution is the most flexible in terms of manipulation of f.s. placement. Several common activities, like changing the number of sources on a given surface, putting sources closer to the edges, or adding more sources in given locations, have proven to be easy and fast.

An STL file describes a raw unstructured triangulated surface by the unit normal and vertices (ordered by the right-hand rule) of the triangles using a three-dimensional Cartesian coordinate system. For each triangle, we calculate its center \mathbf{c} and we use this point to describe the surface of the scatterer or to place fictitious sources. The vector $\hat{\mathbf{n}}$, normal to the triangle on the point \mathbf{c} , is directly read from the file with no further elaborations, and it is also used to calculate the tangential vectors \mathbf{t}_1 and \mathbf{t}_2 as

$$\begin{aligned}\mathbf{t}_1 &= \mathbf{v1} - \mathbf{c} \\ \mathbf{t}_2 &= \mathbf{n} \times \mathbf{t}_1\end{aligned}$$

Appendix C

Waveguides and rectangular cavities

A cavity can be considered as a volume enclosed by a conducting surface and within which an electromagnetic field can be excited. The electric and magnetic energies are stored in the volume of the cavity. The fields in the cavity can be excited, or coupled to an external circuit, by several means as small-coaxial lines loop or probes. Alternatively, the cavity can be coupled to a waveguide by means of a small aperture in a common wall. Before considering the problem of the field solution in a cavity, the problem in a waveguide must be solved.

C.1 Rectangular waveguides

Hollow pipe waveguides are very common at microwave frequencies, and rectangular cavities are the most used in particular. This kind of guide does not support TEM waves. Instead, the field solutions are a superposition of TE and TM waves, and can be found by solving Maxwell's equations in transverse (x,y) coordinates.

For TE waves propagating in the positive zeta direction¹, the solution can be found by imposing $\mathbf{e}_z = 0$ and decoupling the equations in \mathbf{e} and \mathbf{h} ,

¹Through this chapter, an $e^{j\omega t}$ time dependence is assumed, as the usual convention at microwave frequencies.

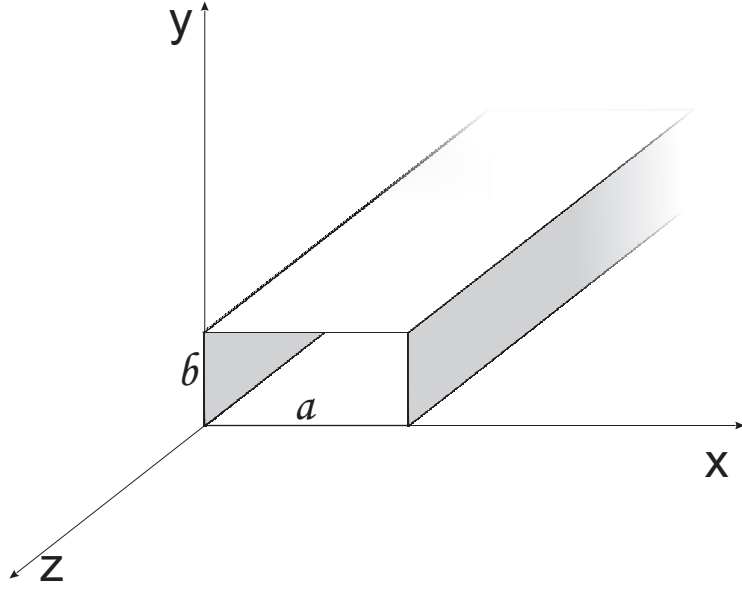


Figure C.1: A rectangular waveguide.

to find

$$\nabla_t^2 h_z + k_c^2 h_z = 0 \quad (\text{C.1})$$

$$\mathbf{h} = \frac{-j\beta}{k_c^2} \nabla_t h_z \quad (\text{C.2})$$

$$\mathbf{e} = -Z_h \hat{\mathbf{z}} \times \mathbf{h} \quad (\text{C.3})$$

where $\beta = (k_0^2 - k_c^2)^{\frac{1}{2}}$ and $Z_h = (k_0 Z_0)/\beta$. The complete field solutions are then given by

$$\mathbf{H} = \pm \mathbf{h} e^{\mp j\beta z} + \mathbf{h}_z e^{\mp j\beta z} \quad (\text{C.4})$$

$$\mathbf{E} = \mathbf{E}_t = \mathbf{e} e^{\mp j\beta z} \quad (\text{C.5})$$

A solution for (C.1) can be found by separation of variable, that is assuming a product solution $h_z = f(x)g(y)$. In this way, the solution for f and g are easily found to be

$$f = A_1 \cos k_x x + A_2 \sin k_x x \quad (\text{C.6})$$

$$g = B_1 \cos k_y y + B_2 \sin k_y y \quad (\text{C.7})$$

where A_1, A_2, B_1, B_2 are arbitrary constants. These constants, and k_x, k_y , can be found by imposing the boundary conditions that h_z must satisfy. In

particular, for a metallic waveguide, the normal component of the transverse magnetic field \mathbf{h} must vanish at the waveguide walls. This means, from (C.2), that it must be $\hat{\mathbf{n}} \cdot \nabla_t h_z = 0$, where $\hat{\mathbf{n}}$ is the normal unitary vector at the walls. When this condition holds, (C.3) shows that the tangential \mathbf{e} will vanish too. In conclusions, the boundary conditions on h_z are

$$\begin{aligned} \frac{\partial h_z}{\partial x} &= 0 & \text{at } x = 0, a \\ \frac{\partial h_z}{\partial y} &= 0 & \text{at } y = 0, b \end{aligned}$$

By substituting this conditions in the solution for f and g , it is found that $A_2 = 0, B_2 = 0$, and that

$$\begin{aligned} k_x &= \frac{n\pi}{a} & n = 0, 1, 2, \dots \\ k_y &= \frac{m\pi}{b} & n = 0, 1, 2, \dots \end{aligned}$$

This gives an expression for h_z equal to

$$h_z = Anm \cos \frac{n\pi x}{a} \cos \frac{m\pi y}{b} \quad (\text{C.8})$$

where $A_{nm} = A_1 B_1$ and both n and m are different from zero, which identifies a trivial constant h_z solution. From this expression we can conclude that the cutoff wavenumber for the nm -th mode is given by

$$k_{c,nm} = \left[\left(\frac{n\pi}{a} \right)^2 + \left(\frac{m\pi}{b} \right)^2 \right]^{\frac{1}{2}} \quad (\text{C.9})$$

The propagation constant for the nm -th mode is $j\beta_{nm} = j(k_0^2 - k_{c,nm}^2)^{1/2}$. For $k_0 > k_{c,nm}$, β_{nm} is real and the mode propagates, otherwise the mode rapidly decays along z .

It is important to notice how $k_{c,nm}$ is dependent from the guide dimensions only, and that the field solution for TM modes gives the same $k_{c,nm}$ expression.

C.2 Perfectly metallic cavity

Figure C.2 illustrates a rectangular cavity: it can be considered a section of a rectangular waveguide of height b and width a , terminated with a short circuit at $z = 0$ and $z = d$. If d equals a multiple of a half guide wavelength at the frequency f , the resultant standing wave pattern is such that the

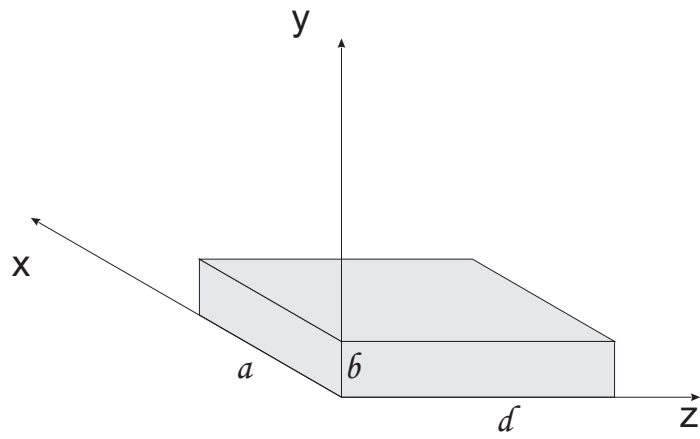


Figure C.2: A rectangular cavity.

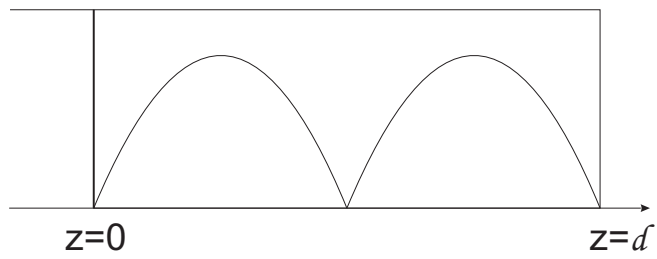


Figure C.3: Standing wave pattern in a short circuited waveguide.

x and y components of the electric field are zero at $z = 0$ and at $z = d$. Consequently, a short circuit can be placed at both this sections, thus constituting a rectangular cavity. The same simple approach leads to the field solution, that can be directly derived from the corresponding waveguide solution. For the nm th TE or TM mode, the propagation constant is given by

$$\beta_{nm}^2 = k_0^2 - \left(\frac{n\pi}{a}\right)^2 - \left(\frac{m\pi}{b}\right)^2, \text{ where } k_0 = \frac{2\pi f_0}{c} \quad (\text{C.10})$$

For the cavity to be a multiple of half a guide wavelength, it must be $\beta_{nm}d = l\pi$. This relation, when used in the C.10, leads to a solution only for discrete values of k_0 that we indicate as k_{nml} , where k_{nml} is given by

$$k_{nml} = \left[\left(\frac{l\pi}{d}\right)^2 + \left(\frac{m\pi}{b}\right)^2 + \left(\frac{n\pi}{a}\right)^2 \right]^{\frac{1}{2}} \quad (\text{C.11})$$

From these values of k_{nml} , the resonant frequencies of each mode can easily be calculated.

It must be noticed that there is a triply infinite number of resonant frequencies, corresponding to different field distributions. Also note that there is more than one field solution for each given resonant frequency, since (C.11) holds for both TE and TM mode. In addition, because of a lack of a preferential coordinate, in the case of a rectangular cavity, field solutions corresponding to TE and TM modes with respect to the x and y axes could also be constructed, and these would have the same resonant frequencies. However, the latter modes are just a linear combination of a TE and TM mode with respect to the z axis and therefore don't represent a new solution.

Equation C.11 can be easily implemented in a spreadsheet or in any other form, and be used to calculate the excitation order of each mode, for arbitrary dimensions a, b, d .

C.3 PEC/PMC waveguide and cavity

A waveguide with two PEC and two PMC walls can support a TEM mode. Fig. C.3 shows a section of such a guide, with the electric field distribution. The magnetic field is orthogonal to it and they both lie on the transverse plane. When the TEM mode is polarized with the electric field parallel to the PMC walls, boundary conditions are satisfied. In fact, PMCs surfaces have a null orthogonal electric field and a null tangential magnetic field. Viceversa, PEC walls have a null tangential electric field and a null orthogonal magnetic field.

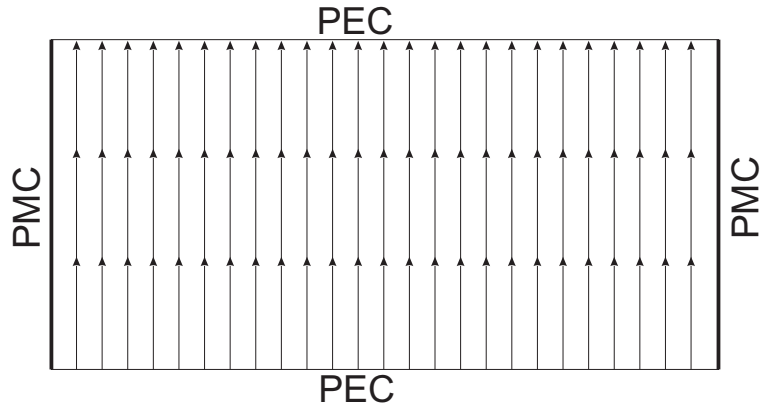


Figure C.4: A section of a PEC/PMC guide, showing the Electric Field distribution.

When a section of such a guide is truncated with appropriately placed short circuit walls in the z direction, a cavity can be obtained by applying the same exact procedure described in the previous section.